UNIVERSITÀ DEGLI STUDI DI MILANO

Scuola di Dottorato in Fisica, Astrofisica e Fisica Applicata
Dipartimento di Fisica

Corso di Dottorato in Fisica, Astrofisica e Fisica Applicata
Ciclo XXV

Phase Behavior of Star-Shaped DNA Nano-Structures

Settore Scientifico Disciplinare FIS/03

Supervisore: Professor Tommaso BELLINI

Coordinatore: Professor Marco BERSANELLI

Tesi di Dottorato di:
Silvia BIFFI

Anno Accademico 2012-2013

Commission of the final examination:

External Referee:
Professor Francesco SCIORTINO

External Member:
Professor Francesco MANTEGAZZA

Internal Member:
Professor Tommaso BELLINI

Final examination:

Date January 21, 2013

Università degli Studi di Milano, Dipartimento di Fisica, Milano, Italy

To my brothers, Marco and Andrea

Cover illustration:

Solution of DNA nano-stars tagged with EtBr showing phase separation.

MIUR subjects:

FIS/03

PACS:

82.70.Dd

Contents

List of Figures

List of Tables

Introduction

Motivation

In the last years a strong interest has been devoted to the synthesis of new generation colloids, particles interacting via strongly anisotropic forces arising from non-spherical shapes or from physical or chemical patterning of the particles surface. [1–4]. Potentially, if properly designed, these particles can act as macromolecules, and used to mimic the behavior of real molecular systems. In this respect, a particular stimulating class of new colloids is provided by the so-called limited valence particles, i.e. particles with a small controlled number of possible bonding opportunities. As the mutual interactions of these particles are made stronger and densely packed aggregates become increasingly stable, it is expected that the system undergoes some kind of phase transition, a colloidal analog of the gas-liquid coexistence in simple liquids. Theoretical and numerical studies predict that the unstable region in the *temperature-concentration* $(T - c)$ plane significantly shrinks, with critical temperature T_c and critical concentration c_c decreasing as the valence is reduced [5]. Such a prediction can not be tested in molecular systems owing to the inevitable presence of additional interactions besides the directional ones. As building these shapes can be challenging, very often the emphasis has been on designing single-particle properties and on tuning mutual interactions, so to guide their assembly into definite structures under specific conditions [1–4, 6, 7]. Until now, less effort has been devoted to the study of their statistical behavior, phase transitions and emerging collective structures and properties.

In parallel with studies on new generation colloids, an increasing interest has been developed towards the DNA molecule and the possibility to exploit DNA self-assembly properties to build DNA nano-structures on design. Nano-sized objects such as geometrical figures, nano-machines as well as more complex meso- and macroscopic structures can nowadays be self-assembled via a rational design of the DNA sequences. What is interesting to our purposes is that DNA nanotechnology also enables constructing particles with mutual interactions controlled in valence, strength and selectivity, e.g. limited valence particles.

We took advantage of the notions on DNA nanotechnology to synthesize star-shaped DNA particles having either three or four arms, each arm terminating in a sticky overhang sequence that provides interactions between individual particles. Each nano-star can thus be viewed as a limited valence particle whose valence number f is dictated by the number of star arms. Such structures offer two main advantages (i) nano-stars geometry is only provided by the DNA assembly and hence it is unique, a feature that makes DNA nano-stars easy to be produced in bulk quantities (ii) interactions between individual nano-stars can be tuned by controlling the temperature and the composition of the overhang sequences.

These properties makes the DNA nano-stars an ideal system to experimentally investigate the dependence of the gas-liquid coexistence region from the valence, answering the limited-valence issue introduced on top.

Thesis overview

Main results

Driven by the motivations described above, the present Thesis is devoted to the experimental investigation the equilibrium phase behavior of solutions of DNA nano-stars having either $f = 3$ or $f = 4$, with the aim to provide the first experimental study on the collective behavior of particles provided with bond limitations in number and directionality. The main results of this Thesis are summarized below.

Determination of the phase diagram for $f = 3$ and $f = 4$ star-shaped DNA nano-structures Solutions of $f = 3$ and $f = 4$ DNA nano-stars are found to exhibit liquid-gas-like phase separation, with critical parameters depending on the valence, thereby confirming for the first time recent theoretical predictions [5]. The range of DNA concentrations where separation takes place is rather limited and decreases on going from $f = 4$ to $f = 3$. The concentration of the dense phase is comparable to the concentration of regular networks in which DNA constructs are fully-bonded with f neighbors each. T_c also decreases with decreasing f, according to the reduced number of bonds. To the best of our knowledge, this is the first observation of critical behavior in DNA solutions.

Critical activated dynamics As the temperature of the system is reduced, and the critical point approached from above, the dynamic behavior slows down and becomes characterized by a two-step relaxation process, with the clear insurgence of a plateau whose height (the so-called non-ergodicity factor in glass physics [8]) increases on cooling. All correlation functions can be well fitted to the sum of two stretched exponentials. As T decreases, the two characteristic times behave differently: the faster one (τ_f) changes only very mildly while the slower one (τ_s) slows down by more than three orders of magnitude in an Arrhenius fashion, without any noticeable divergence as T_c is approached. Quite remarkably, τ_s does not show the power-law divergence expected for critical slowing down.

Colloidal macromolecules The colloidal system here proposed makes use of DNA not only to introduce mutual interactions between individual particles, but to model their geometry controlling internal interactions at the nanoscale level. This work proves that DNA is a powerful tool to produce particles with directional interactions, and can be used to design complex structures as colloidal molecules at the nanoscale.

Organizational note

The present Thesis consists of two Parts, for a total of six Chapters. Part I is composed of Chapters 1, 2 and 3 and introduces to phase diagrams of colloidal systems, to DNA properties and to the experimental methods used to investigate the behavior of the system, Part II spans from Chapter 4 to Chapter 6 and reports the results obtained within this study.

Chapter 1: Exploring phase transitions with colloids: We described the use of colloids as model system to mimic the behavior of atomic systems. We give examples of existing anisotropic particles and introduce to the limited-valence issue.

Chapter 2: DNA as a tool to explore soft-matter: We introduce the properties of the DNA molecule and describe its use to build nano-structures, in particular to assembly 2D and 3D crystals.

Chapter 3: Experimental methods: Given the biological nature of the particles used in these work, a variety of experimental techniques proper of biology have been employed to characterize the system behavior. This Chapter describes these techniques, together with the basic principles of static and dynamic light scattering experiment.

Chapter 4: Star-shaped DNA structures: preparation and characterization: Here we provide a full description of the individual DNA nano-stars. Design, energies, characterization of the full-formed nano-stars are reported in this Chapter.

Chapter 5: Phase diagram of limited valence aggregates: By means of measurements of volume and of UV absorbance we determined the phase diagrams of $f = 3$ and $f = 4$ particles. DNA nano-stars are found to exhibit liquid-gas-like phase separation, with critical parameters depending on the valence.

Chapter 6: Static and dynamic behavior of $f = 3$ and $f = 4$ DNA nano-stars: light scattering measurements: We report the results of the investigations performed on the DNA systems via light scattering measurements. Characterizations of the $f = 3$ and $f = 4$ system along the critical isochore, comparison between non-critical $f = 4$ samples prepared at various concentrations, high density behavior and investigation of the coexistence phases are discussed in this Chapter.

Part I

Chapter 1

Exploring phase transitions with colloids

1.1 Spherical colloids as tool to explore crystalline and liquid structures

Colloidal suspension are solutions of solid particles, with size ranging from typically 1 nm to 10 μm, dispersed in a simple molecular solvent. Colloidal particles can be thought as solid spheres, rather than as large molecules: they are big enough that we don't need a detailed knowledge of their internal degrees of freedom to describe them (i.e. we do not need to know the detailed microscopic arrangement of their constituents). At the same time, colloids are small enough that the thermal energy scale set by k_BT is relevant for their interactions. Their behavior is determined by the laws of statistical mechanics. In equilibrium, colloidal suspensions occur in the phase with the lowest free energy, and the dynamics of colloids in equilibrium is due to thermal ("Brownian") motion.

Interactions between colloids

Interaction between colloids can be tuned by varying the properties of the solvent in which the particles are disperser, or by functionalizing their surface. Van der Waals attractive forces can be screened by making the surface of the colloids charged, so that electrostatic repulsion stabilize the colloids, preventing them from aggregation. The screening length that comes from electrostatic repulsion can in turn be tuned by varying the concentration of ions in solution. Another way to stabilize colloids is to cover their surface with polymers: when two colloids get close to each other, steric interactions between polymers induce a repulsive force between the particles. The range of steric repulsion is set by the polymers length. Clearly, a condition for steric stabilization to work is that the solvent is a good solvent for the polymers. Attractive interactions between colloids can be introduced, in a controlled way, via depletion forces. These forces origins whenever the solution contains, in addiction to the suspended particles, other particles (macromolecules) or non adsorbing polymers intermediate in size between the suspended particles and the size of the solvent molecules. Macromolecules are excluded from a depletion zone near the surface of the colloidal particles. When the depletion zones of two particles overlap, a net attractive force results between the particles, arising from unbalanced osmotic pressure.

Colloids as giant atoms

The description of the static properties of a colloidal suspension resembles that of a system of atoms in vacuum. Colloids, though, offer more advantages than standard atomic systems from both a theoretical and an experimental point of view: (i) many colloidal particles can be represented quite well by models - such as the Hard-Sphere and Yukawa models - that are far too simple to represent molecular systems (ii) the tunability of

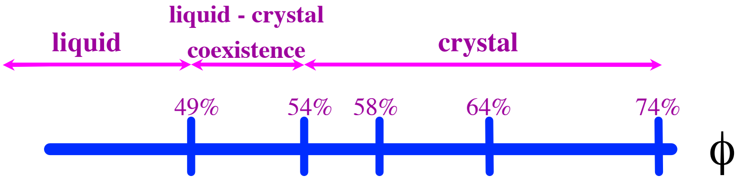

Figure 1.1: Phase diagram for hard-sphere colloids

colloid-colloid interactions is almost arbitrary, as opposed to standard atomic interactions fixed by elementary chemistry (iii) characteristic space and timescales are much larger with respect to atomic systems, allowing for experimental studies in the light scattering regime and for a better time resolution.

For these reasons colloids have often been used as a model systems to reproduce and study the behavior of atomic systems, e.g. to study liquid and crystalline structures, phase transitions, or to understand dynamical arrest processes [9–12]

1.1.1 Equilibrium phase diagram for hard spheres

The simplest model of interaction potential is the so called *Hard-Sphere* model. In this model, each colloid is described as a perfect sphere that interacts via a potential which is zero except where two spheres overlap, in which case it is infinite due to excluded volume restrictions. Temperature has no influence on the particles behavior. The only control parameter for the behavior of this system is the volume fraction ϕ, i.e. the fraction of volume occupied by the particles with respect to the total volume.

At low packing fraction the particles composing the system are free to move, acting like gas molecules of a molecular system. At high density, instead, the particles need to organize in a crystalline structure simply due to packing constraints. The maximum density of a system of hard spheres is obtained when they are arranged in a regular close-packed structure, in which case the volume fraction of the spheres is $\phi = 0.7404$. A random close-packing, instead, would lead to $\phi \approx 0.63$. However, the hard sphere system becomes crystalline even at lower concentration than that for the ordered or random close packing. This was demonstrate by Pusey and van Megen, who experimentally realized hard-spheres using sterically stabilized PMMA particles [13]. They found that for packing fractions comprised between $\phi = 0.49$ and $\phi = 0.545$ a system of hard spheres phase separates in two coexisting phases, a fluid-like phase and a crystalline phase.

This phase separation is not driven by attractive interactions, which are absent in hard spheres. Instead, it is only driven by entropic effects. At low packing fractions the fluid- (gas-)like arrangement of particles minimizes the entropy of the system, but when ϕ increases, approaching the concentration of the random close packing, crowding effects become relevant in determining the energy of the system. On one side, a regular crystal with long range order looses orientational entropy (it looses the possibility to explore the whole volume) with respect to a random, liquid-like arrangement, but on the other side it gains vibrational entropy. Adopting a crystalline packing individual spheres have more space locally to explore, and thus the whole entropy of the crystalline state is higher than the entropy of the amorphous state. Thus, when $\phi > 0.49$ it is more convenient for the system to organize in a regular crystal than to remain in the fluid state.

Equilibrium phase diagram is shown in Fig. 1.1

1.1.2 Equilibrium phase diagrams for spherical particles with tunable interactions

We discuss here the equilibrium phase diagrams for colloids which have at the same time short range (range smaller than approximately one tenth of the particles diameter) repulsive interaction, and attractive interaction (short range or long range).

In Fig. 1.2 are shown the phase diagrams obtained from simulations for a system composed of colloids and macromolecules that act as depletant [14]. Phase diagrams are expressed as function of the concentrations of colloids and macromolecules, η_c and η_p respectively. q is a parameter indicating the ratio between the size of the depletants and the size of the colloids. As it is possible to see in Fig. 1.2a, when the diameter of the macromolecules is comparable to that of the colloids (e.g. $q = 0.8$, the range of interaction is "long") the phase diagram that characterize the system is similar to the phase diagram obtained for a molecular systems. The variable η_c is the analog of the density ρ for the fluid of a molecular system, while the variable η_p plays the role of $1/T$, where T is the temperature of the system. In both cases (colloidal and molecular system) lowering the temperature down, or increasing the depletion forces, the system phase separate.

When $\eta_p = 0$ no attractive forces act, and we go back to the hard sphere case. By increasing the macromolecules concentration colloidal particles experience attractive interactions. When the attractive interactions are weak, the system undergoes a liquid-solid transition driven by the effective repulsion between the particles. This repulsion includes both the repulsion having entropic origin, that underlies the excluded volume effect, and any other physical repulsion (that may be due to electrostatic or polymer-mediated interactions). The Fluid-Solid (F+S) interaction is always first order, because there is a change in symmetry between the two phases and the transition cannot take place gradually and thus there can be no critical point [9]. When the attractive part of the potential becomes more important, we can have a Fluid-Fluid (F+F) phase separation which is analogous to a gas-liquid (demixing) transition. The system separates in a *colloidal gas* and *colloidal liquid*, where by colloidal gas and colloidal liquid we mean a colloid-poor and colloid-rich phase respectively. This transition can take place continuously, and thus there is a critical point. However, when the coexisting volume fraction for the liquid phase is large enough, this phase can lower its free energy even further by going over to an ordered state. Thus, according to the amount of added polymer, one can have a phase transition as a function of particle concentration from a gas to a liquid phase, from a gas to a solid crystal state, and indeed at one special condition there is a triple point, where gas, liquid, and crystal coexist [9].

Reducing the size of the depletant ($q = 0.4$), and thus the range of attractive interactions that act on colloids, the phase diagram is deeply modified. We can see from Fig. 1.2b that (i) the consolution curve describing the coexistence of the two fluid phases disappears. In the phase diagram remains a unique coexistence region between a fluid of equilibrium and a solid of equilibrium (F+S) (ii) given the huge difference in density and in structure between the fluid phase and the solid phase, equilibrium between gas and solid is found, but the transition becomes metastable. In other words, increasing η_p to value that go over the line B-C-D the system does not unmix immediatly in fluid and crystal, but it may remain for a long time in a metastable fluid phase. This metastable phase is in turn characterized by phase separation phenomena between metastable fluids.

A metastable state describes a local minimum of energy, where the system may remain for a long time. When concentration fluctuations bring a region of the system to one of the equilibrium concentrations (the concentration of the equilibrium gas or solid), then the whole system phase separates to reach the two equilibrium concentrations corresponding

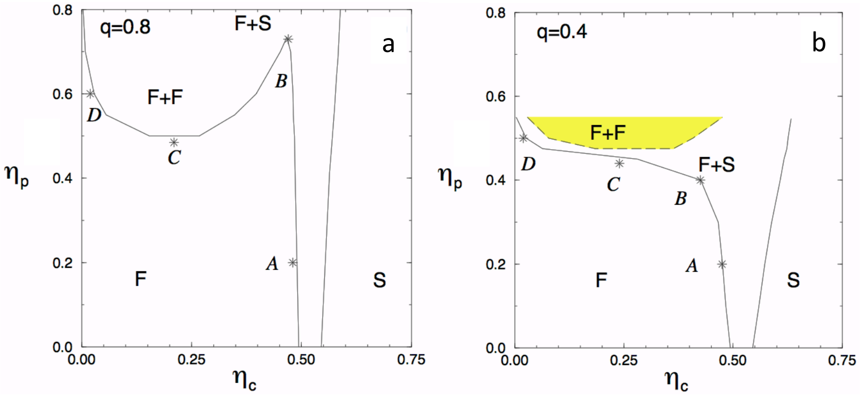

Figure 1.2: Phase diagrams for spherical colloids with tunable interactions. (a) long range attraction leads to the colloidal analog of the phase diagram obtained for atomic systems (b) short range attraction leads to the formation of metastable states (yellow region). Star points have been investigated in detail by the authors. [14]

to the minimum energy of the system.

1.1.3 Taking dynamics into account: dynamical arrest

Phase diagrams discussed in the previous section are ”thermodynamic” phase diagrams, i.e. they represent the equilibrium states of the systems discussed. But when the dynamics of the particles is taken into account, these equilibrium states, even if predicted, may not be reached. In presence of attractive interactions the solid state obtained after phase separation is not a crystalline structure, but a glass. For hard sphere systems, a glassy state is found for $\phi > 0.58$ [13]. This structural arrest is only due to excluded volume effects that trap the particle in a cage of nearest neighbors. This is the so called *caging* mechanism, which causes jamming and non-ergodicity in hard-sphere systems, originating the so called *repulsive* glass. Even the phase diagram in Fig. 1.2b results to be deeply modified when dynamics is taken into account, and a very rich phenomenology is found, as sketched in Fig. 1.3 [15]. Here the y-axis is reversed with respect to Fig. 1.2, since the temperature T, i.e. the inverse of the depletant concentration η_p is plotted.

Again, at high temperatures the system behavior is close to that of a hard-sphere system, and for high concentrations a repulsive glass is found. Lowering the temperature, the presence of attraction leads to the formation of temporary bonds between particles. This process competes with the caging mechanism and alters the short-range order, thereby creating small aisles for the particles, whose mobility is effectively increased. In a limited range of temperatures, this competition between attraction and repulsion causes the melting of the repulsive glass on cooling. If cooling persists, the bonding eventually prevails and the system falls into the second type of arrested state, the *attractive glass.* In fact, a reentrant liquid-glass line, surrounded by two distinct glasses, is found, which gives rise to the liquid pocket in Fig. 1.3. At low volume fractions the presence of attraction also causes a low density disordered and arrested state, which is called a *gel* [11]. The formation of gels and the connection of the gel line with the glass line (see figure Fig. 1.3) are not yet fully understood. Very recent results suggest that gels are the result of an arrested phase separation, i.e. that follow the crossing of the spinodal line of a liquid-gas

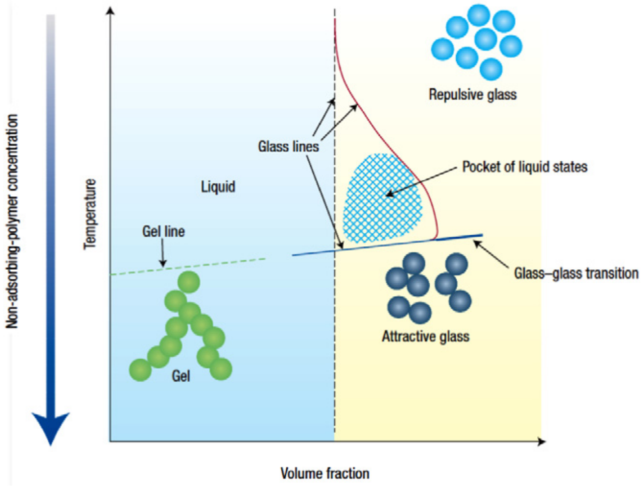

Figure 1.3: Phase diagram that schematizes the different arrested states in a colloidal system with short-range attractions. The vertical dashed line represents the hard-sphere glass line. The connection between the gel line and the attractive glass line is object of ongoing research.

phase transition [16]. In this view, the dense phase after the separation would become so concentrated as to be effectively arrested.

1.2 New generation colloids

In the previous section we discussed how colloidal system are used as a model to reproduce the behavior of atomic systems. The description presented is only relative to colloids with spherical symmetry. The question arises about what happens to the phase diagram when particles are characterized by anisotropic interactions. In the last few years a new generation of colloids has been synthesized, exploring a variety of anisotropic interactions. These can be achieved by chemical functionalization of the particles surface, so that different region of the surface have different properties of interaction, or using non-spherical geometries. Here we review some of these new particles, with a particular attention to those characterized by directional bonds which resemble the shape of real molecules.

1.2.1 Colloids with anisotropic interactions

Anisotropic shape and interactions through chemical patchiness are powerful tools for engineering the assembly of particular targeted structures. A variety of synthesis methods have been developed, including emulsion drying, selective deposition, drawing from the diverse fields of chemistry, physics, biology, engineering and materials science. Over the years a variety of geometrical shapes have been built, opening a wide spectrum of particle anisotropy [1].

Recently a classification scheme has been proposed to describe the potentially infinite types of anisotropic particles [1]. The scheme considers each type of anisotropy as a ”dimension”. Moving along a dimensional axis leads to a continuous or discrete tuning of the corresponding anisotropy attribute, so that each particle can be described by a vector

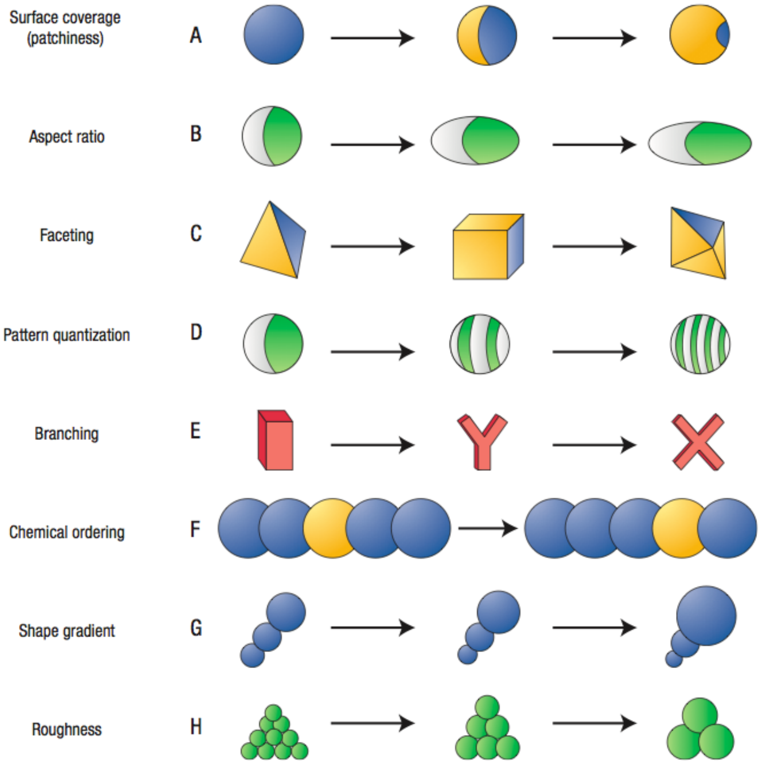

Figure 1.4: Anisotropy dimensions used to describe key anisotropy attributes of particles. Homologous series of particles as the attribute corresponding to the anisotropy axis is varied from left to right. [1].

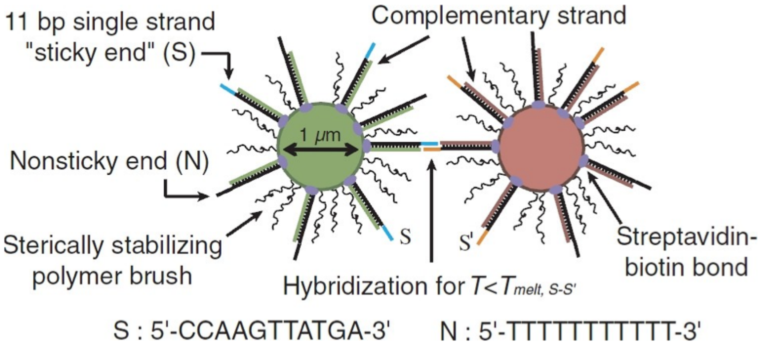

Figure 1.5: Schematic representation of micron-sized colloidal particles coated with DNA strands with interacting sticky-ends. Each helix ends with a 11bases dangling strand, either non-interacting (N) or complementary to the tails on the second type of particle (S, S') [17].

comprising few critical dimensions, each of variable amplitude. The scheme is reproduced in Fig. 1.4. Each line represents a specific anisotropy dimension, and moving along the line the amount of anisotropy can be tuned.

Among the most common surface covering is functionalization with DNA strands. The recognition properties of DNA (see Chapter 2) are exploited to introduce selective interactions between particles. Particles are covered with single strand DNA, or with double stranded DNA terminating in ”sticky-ends”, which are short single strand sequences. Two particles covered with complementary sequences can bond via hybridization of their single stranded sequences. An example is reported in Fig. 1.5.

1.2.2 Colloidal macromolecules

One of the most active fields in particle synthesis is the production of colloidal macromolecules, i.e. colloids which mimic shape and interactions that characterize molecular systems.

To synthesize these particles a variety of methods have been developed, all including long and complex synthesis procedures. In Ref. [4] multiple protrusions of monomers are grown on highly cross-linked polymer spheres, the number and size of protrusions controlled by carefully changing the synthesis conditions (see Fig. 1.6a). The resulting geometries can be viewed as macromolecules.

An alternative mechanism to obtain molecular geometries is to induce the assembly of relatively simple particles in combined structures. An example of these approach are the Pac-man particles, which makes use of lock and key identification mechanism for directing the assembly of complex structures [6]. As shown if Fig. 1.6b, colloidal spheres act as as

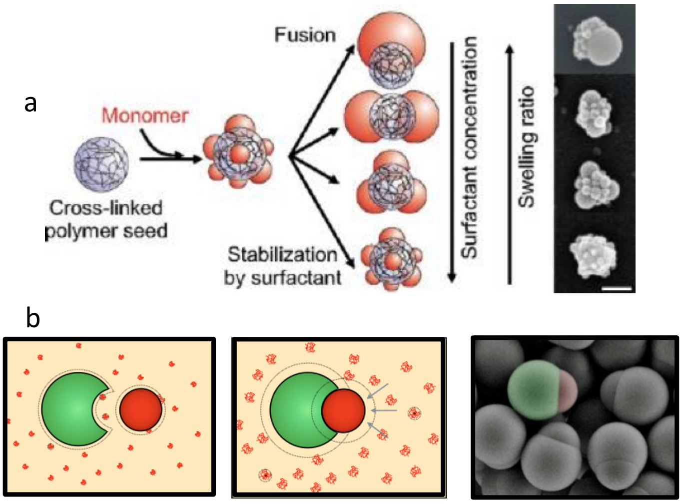

Figure 1.6: (a) Schematic of the synthesis technique and systematic influence of several factors on the resulting patchy particles [4] (b) Pac man particles [6].

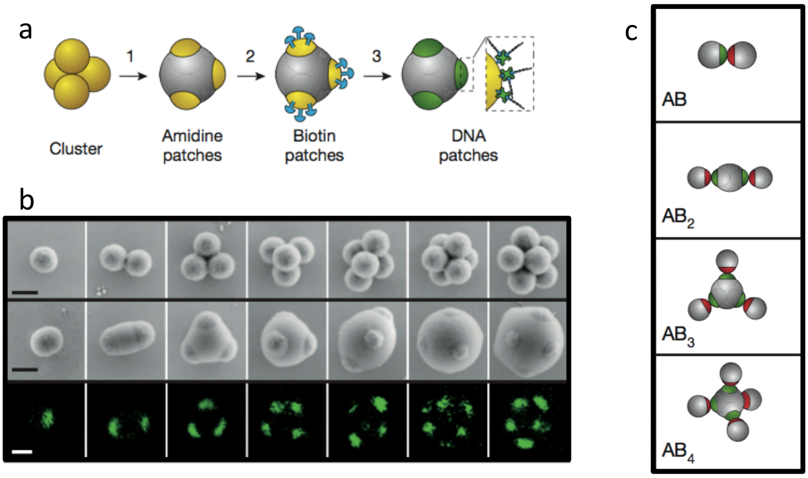

Figure 1.7: (a) DNA patchy particle fabrication (b) pictures of colloidal clusters, patchy particles, and fluorescence from dye-labelled patches (c) Colloidal molecules [7].

key, and monodisperse colloidal particles with a spherical cavity (Pac man particles) act as locks. Locks and keys, Pac men and spherical colloids, are hold together by depletion forces. What makes the interaction specific is the fact that the assembly is controlled by how closely the size of a spherical colloidal key particle matches the radius of the spherical cavity of the lock particle. The structure can be viewed as a simple molecule, but to obtain more complex structure it is necessary to use a different approach.

Colloidal molecules with specific shape and selective interactions were obtained only recently, from controlled assembly of spherical particles functionalized with DNA. At first, spherical particles are assembled into a clusters, which is swollen with styrene such that the extremities of the cluster protrude from the styrene droplet. Protrusions from the original cluster become patches of the new particle, and are made "sticky" by functionalization with DNA. The choice of DNA sequences for covering the patches surfaces enables to design interactions between individual particles. An cartoon of the particles fabrication, images of the particles, and representation of their assembly are shown in Fig. 1.7.

1.3 Colloids of limited valence: theoretical and numerical predictions

Patchy particles are, by definition, characterized by a limited number f of directional bonds. It is limited in the sense that the number of possible bonds is $f < 12$ and thus the interaction potential of the particle can not be described by a spherical potentials.

The collective behavior of these particles has been deeply investigated both theoretically and numerically. Theoretical studies of the physical properties of these systems started in the eighties in the context of the physics of associated liquids [5]. In these works, to focus on the essential features of inter-particle association, molecules were modeled as hardcore particles with attractive spots on the surface (see Fig. 1.8). To resemble the molecular behavior it is also necessary to insert the limitation that each patch/interaction site/can only bond one bond at the time, a situation properly described by the Wertheim theory [18].

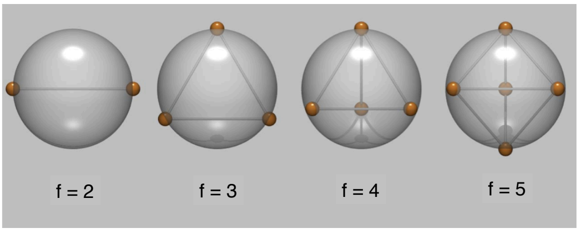

Figure 1.8: Hardcore particles with f attractive spots on the surface [5].

Both theory and simulations predict patchy particles to undergo a gas-liquid-like phase separation in a colloid-poor and colloid-rich fluid. What is relevant here, with respect to the case of spherical interactions, is that for patchy colloids the coexistence region is predicted to be strongly affected by the number f of interacting sites. Reducing the bond possibilities (i.e. reducing f), the coexistence region reduces too, and it is progressively confined towards lower and lower packing fractions (resembling zero). Fig. 1.9 shows a family of phase diagrams obtained via numerical simulations for particles having diverse valence numbers. Patchy colloids were modeled as spherical particles decorated with a number f of identical short-ranged, square- well attraction sites per particle (sticky spots), distributed on the surface with specific geometries [5].

These results demonstrates that the number of possible bonds per particle is the key parameter controlling the location of the critical point. The coexsitence region maintains the shape of a gas-liquid consolution curve, and hence the dilute phase and the dense phase obtained after separation can still be considered a colloidal gas and a colloidal liquid respectively. The liquid phases obtained in patchy systems though have very low concentration - with respect to colloidal liquid obtained from spherical interactions - and for this reason are called *empty liquids*.

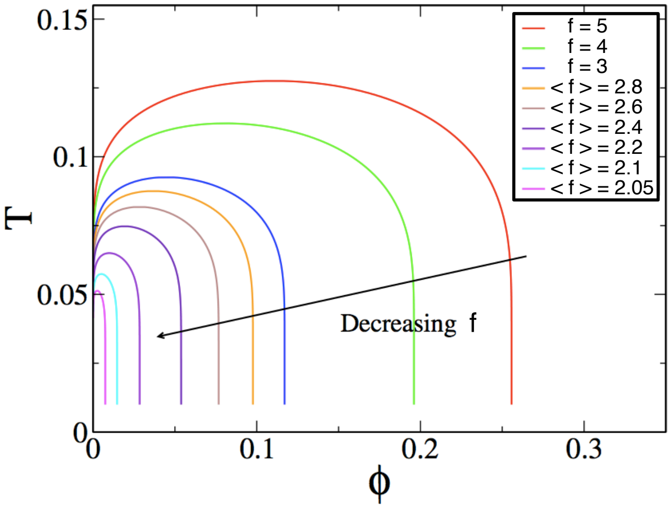

Figure 1.9: Phase diagram for hardcore particles with f attractive spots on the surface. The phase diagram is in the form of a gas-liquid consolution curve. The coexistence region significantly shrinks as the valence number f of the particles is reduced. Adapted from [5].

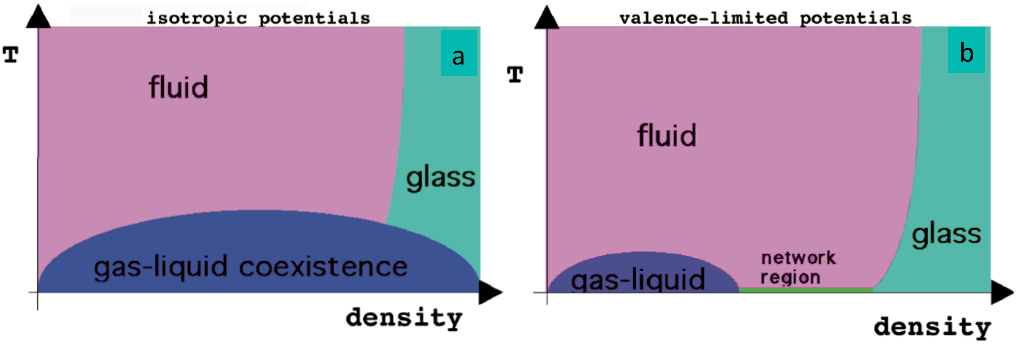

Figure 1.10: (a) Phase diagram for spherical potentials (b) Phase diagram for limited valence particles. The gas-liquid coexistence region is reduced with respect to (a). A new region opens where particles form a transient network. As the temperature is reduced the lifetime of bonds increases and the system dynamically arrests, originating an equilibrium gel.

Patchy colloids and dynamic arrest

The shrinking of the coexistence region depending on f has noticeable consequences within the context of dynamical arrest, and in particular of the gel formation processes. It has been shown that, in presence of spherical interactions, gels are the result of an arrested phase separation. After crossing the consolution curve, the dense phase of the system may become so dense that the system dynamically arrests due to crowding effects. With patchy systems, instead, the shrinking of the coexistence region opens in the phase diagram a large region of intermediate densities, in which there is no driving force for phase separation (see Fig. 1.10). Within this region it would be possible to obtain a gel without any action from phase separation, an *equilibrium gel* originating as a consequence of the bond lifetime of particles, instead that of crowding effects. As the temperature is reduced, particles interact and form a transient network, whose restructuring depends on the lifetime of the particle bonds. Lowering the temperature, the network grows in size (from percolating to spanning) but also becomes ”long living” since bonds between particles last longer. Lifetime of bonds thus determine the slowing down of the dynamics of the system, till it becomes dynamically arrested [19].

Empty liquids and equilibrium gels in a complex colloidal clay

Despite the extensive work on simulations and the promising synthesis of new patchy colloids, there is neither a strategy for realizing bulk quantities of particles with controlled valence [7], nor any experimental evidence for the systematic dependence of the coexistence curve on the valence.

A first experimental result supporting predictions on empty liquids and equilibrium gels has been recently obtained from a complex colloidal clay, Laponite, whose behavior can be interpreted within the contest of patchy interactions invoking an effective (although unknown) limited valence of the clay particle [20].

Laponite is an industrial synthetic clay made of nanometer-sized discotic platelets with inhomogeneous charge distribution and directional interactions (see Fig fig:1.8). The anisotropy of the face rim charge interactions, combined with the discotic shape of Laponite, produces a very rich phase diagram including disordered (gels and glasses) and ordered (nematic) phases, on varying colloidal volume fraction at fixed ionic strength.

At low concentrations the system ages very slowly up to a final non-ergodic state [20]. Even if samples seem to be arrested on the second timescale, a significant evolution takes

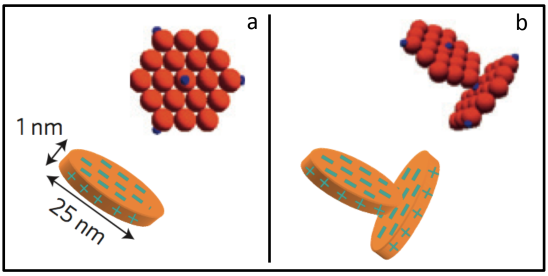

Figure 1.11: (a) The laponite platelet is schematized as a rigid disc composed by 19 sites (red spheres) with five attractive patches (blue spheres), three located on the rim and one at the centre of each face (b) T-bonded configuration for two interacting Laponite platelets and its realization in simulations [20]

place on the year timescale.

The phase diagram of low density laponite systems as a function of concentration and time is shown in Fig. 1.12. In the lower panel, symbols correspond to experimental waiting times required to observe the non-ergodic behavior of the sample by dynamic light scattering measurements. Three different regions, characterized by three different types of arrested state can be observed after years ($\approx$ 4 years). For very low concentrations ($c_w < 1.0\%$) samples undergo an extremely slow, phase-separation process into clay-rich and clay-poor phases, which terminates at a finite but very low clay concentration, above which the samples remains in a homogeneous arrested state. At higher concentrations ($1\% < c_w < 2\%$) an equilibrium gel is found, characterized by a spanning network of T-bonded discs. Higher densities ($2\% < c_w < 3\%$) instead are characterized by the formation of a Wigner glass where disconnected platelets are stabilized in a glass structure by the electrostatic repulsion. The topology of the phase diagram offered by laponite is thus consistent with that predicted for patchy colloids, offering the first experimental observation of an empty liquid. An equivalent phase diagram on particles with defined valence number though is still missing, and as a consequence there is no evidence yet of the dependence of the coexistence region from the valence.

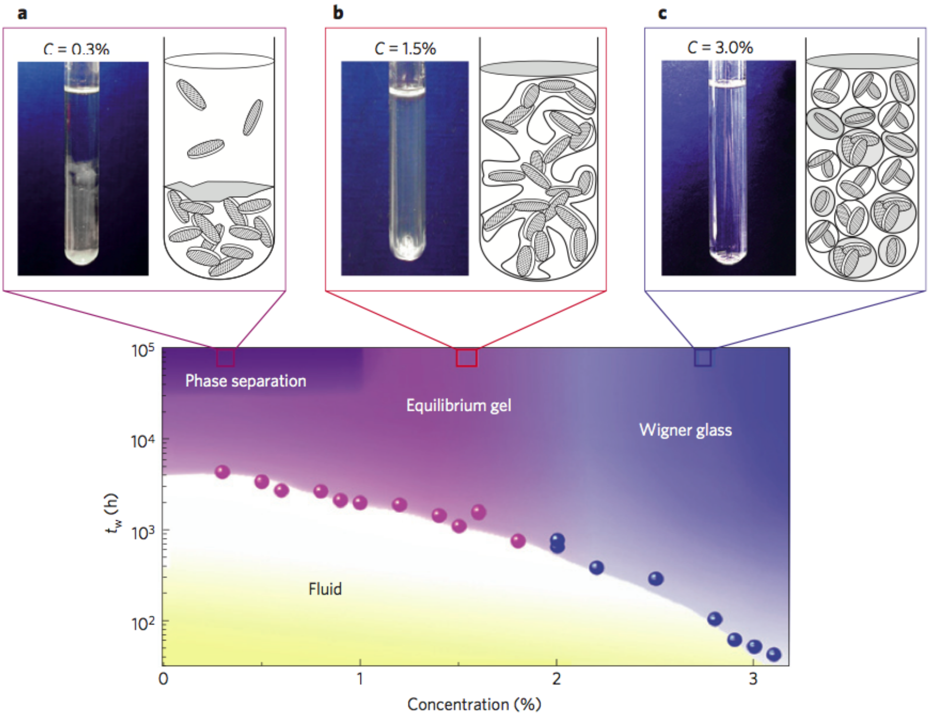

Figure 1.12: Phase diagram of laponite clays. (a) phase separation between clay-poor and clay-rich phases (b) equilibrium gel characterized by a spanning network of T-bonded discs (c) Wigner glass formed by disconnected clays stabilized by repulsion

Chapter 2

DNA as a tool to explore soft-matter

DNA has been subject of a huge amount of studies, which contributed to reveal its structure and its internal and mutual interactions [21]. Properties such as sequence recognition, reversibility of bonding, and thermoregulation of interactions all play a role in the biological processes. Parallel to molecular biology investigations, remarkable self-assembly properties of DNA have recently been recognized. Various studies have demonstrated that, besides its biological purposes, DNA can be used to design nanoscale objects and DNA-based materials controlling interactions at the nanoscale level.

2.1 The DNA molecules as a building block

Deoxyribonucleic acid, better known simply as DNA, is probably the most famous biopolymer thanks to its fundamental role in the transmission of genetic informations. DNA chains usually associate in pairs to form the famous double helix structure, in which the two strands are wound around each other [22]. A DNA chain is a sequence of nucleotides, building blocks which in turn are composed of three sub-units: a phosphate group, a sugar deoxyribose molecule and a nitrogen base (nucleobase). DNA only has four types of nucleotides, only differing among each other in the nucleobase: Adenine (A), Guanine (G), Cytosine (C) and Thymine (T). The way these nucleotides come in succession composes the DNA sequence, and in living organisms this sequence carries the genomic information. Phosphate groups bind sugar molecules of adjacent nucleotides in a phosphate-sugar backbone with directionality conventionally expressed from 5' to 3'. The labeling origins from the position, in the sugar molecule, of the carbon atoms involved in the bond. When assembled in the double helix conformation, two strands have opposite orientation (see Fig. 2.1).

Nucleobases are flat and strongly hydrophobic. For these reasons they occupy the inner part of the double helix, where they tend to get close to each other and overlap to minimize contact with water molecules. Since rigidity of bonds prevents the backbones form bending, in order to enable the approach between nucleobases the two filaments twist and adopt the helicoidal shape.

Several conformations of the double helix are possible, which basically differ in the orientation that nucleobases assume with respect to each other and to the axis of the helix. The most common shape adopted within biological systems is the B shape, in which nucleobases remain on average parallel to each other and perpendicular to the helix axis. In this conformation the periodicity of the helix is $\sim$10 base pairs, equivalent to a length of ~ 3.4 nm, while its diameter is ~ 2 nm. Given the periodicity of the helix we can estimate that in B-DNA each base is tilted of $\sim 36^\circ$ with respect to the previous one.

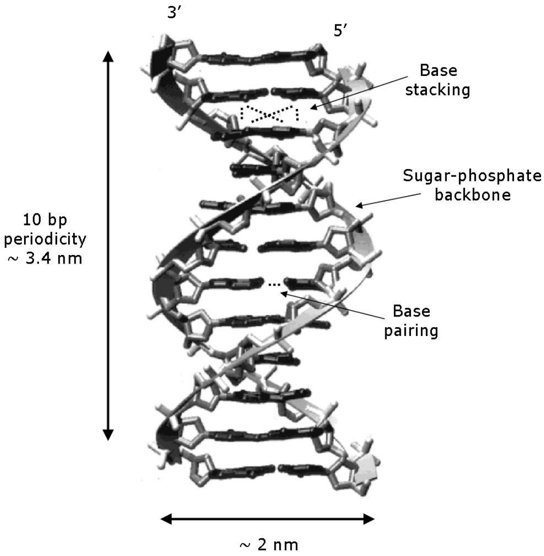

Figure 2.1: B-shape of the DNA double helix.

DNA double helix is also stiff. While single strand DNA behaves like a polymer chain and its persistence length is in the order of ≈ 1 nm, in double stranded DNA persistence length is ~ 50 nm, meaning that the double helix remains stiff for about 15 twists.

2.1.1 Pairing and stacking forces

Hybridization is the process in which the double helix is formed: two single strands (ss) of DNA bond to each other in a doublet (double strand - ds) that takes the shape of a double helix. The double helix is stabilized by the action of two forces: pairing and stacking.

Base pairing originates from the formation of hydrogen bonds between pairs of nucleotides. Strength of interactions is maximized when nucleobases satisfy the Watson-Crick (WC) pairing A-T and C-G, while other coupling combinations are usually unfavorite and charge the duplex with high energetic penalty. Thus it is not surprising that hybridization energy, *i.e.* the energy associated with the formation of the double helix, is related to the length of the strands and on the quality of their WC matching, vanishing for pairs of sequences with poor complementarity. Specificity of pairing relies in the number of hydrogen bonds that each base can form. Fig. 2.2 show that the C-G pair involves three hydrogen bonds, while the A-T pair involves two hydrogen bonds only. In addiction, recent experiments show that only the C-G pairing is actually favorable, meaning that it actually leads to a decrease in the energy of the double helix, while the A-T pairing would be the less unfavorable combination among all the other pairing possibilities [17]. These results suggest that pairing forces provide a minor contribution to the stability of the helix, meaning that the major contribution to stabilization is due to staking forces. Stacking forces arise from hydrophobic interactions between nucleobases: they act to pull nucleobases close to each other to avoid water, and thus hold the helix together. Staking is not selective. Its strength mainly depends on the overlap between nucleobases, that for this reason tilt and increase their overlapping area.

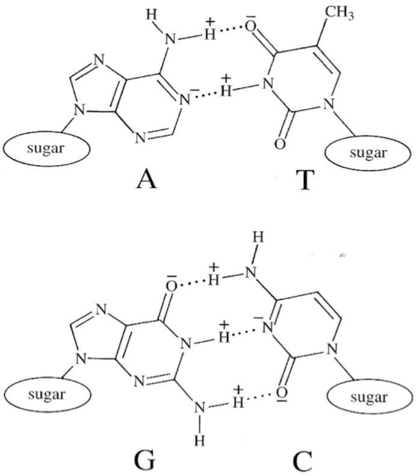

Figure 2.2: Chemical structure of the four DNA nucleotides, showing the Watson-Crick pairing between nucleobases [21].

2.1.2 Thermodynamic description

Processes of formation and melting of the double helix, hybridization and denaturation respectively, are completely reversible and can be repeated multiple times.

The energy involved in the formation of the double helix can be described by the difference in the overall Gibbs free energy G between bonded and unbounded state (G_D and G_U respectively). At the same time this variation in energy can be decomposed in a variation of both enthalpy (ΔH) and entropy (ΔS)

$$\Delta G = \Delta G_D - \Delta G_U = \Delta H - T\Delta S \tag{2.1}$$

In the previous section we described how hybridization energy is sequence dependent, since it is related both on the contribution of stacking forces and on the affinity between the two strands. The large body of observations run over the years has allowed to develop models to calculate ΔG on the basis of the sequences involved in the process. The most adopted model that accounts for the two contributions is called Nearest Neighbor (NN) [23, 24]. According to such a model, ΔG of a duplex involving N paired bases is obtained as a sum of various contributions: (i) N-1 "quadruplet" contributions ΔG_Q, each quadruplet being formed by two consecutive nucleotides on one strand and the corresponding nucleotides on the other strand, (ii) an "initiation" contribution ΔG_{INIT}, representing the free energy cost involved in constraining the two strands in the conformational space available to them when they are bonded in the absence of the contributions from pairing and stacking [25].

The basic idea of the model is that the quadruplet is the smallest unit that includes both pairing and staking effects. Fig. 2.3 shows a drawing of two paired sequences in which the quadruplets are marked by dashed lines. The energy of each quadruplet is written as a sum of contributions from pairing ΔG_P and stacking ΔG_S

$$\Delta G_Q = \Delta G_S + \frac{1}{2}(\Delta G_{P1} + \Delta G_{P2}) \tag{2.2}$$

where subscripts 1 and 2 refers to the two base pairs in the quadruplet (e.g. C-G and G-C in the first quadruplet of Fig. 2.3). Hybridization free energy ΔG_Q for each

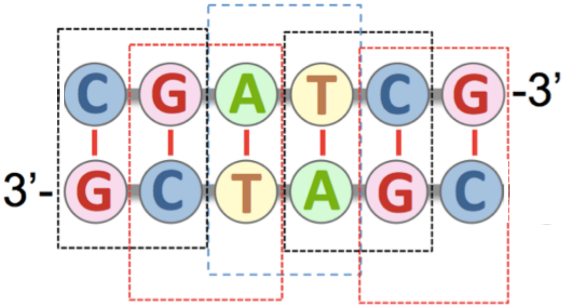

Figure 2.3: Schematic diagram of the *Nearest Neighbor* model to calculate the hybridization energy of a duplex on the bases of its specific sequence. The sequence has 6 nucleotides per strand and 5 different quadruplets in total.

base pair is tabulated together with the corresponding contributions in terms of enthalpy ΔH_Q and entropy ΔS_Q. For self-complementary duplexes an additional ΔG_{simm} term is present. Using the values reported in Ref. [24] the energy of the double helix in Fig. 2.3 can be evaluated for $T = 37°\mathrm{C}$ as

$$\begin{aligned} \Delta G_Q &= \Delta G_{INIT} + \sum_Q \Delta G_Q && (2.3)\\ &= \Delta G_{INIT} + \Delta G_{simm} + \Delta G_{CG/GC} + \Delta G_{GA/CT} + \ldots && (2.4)\\ &= +1.96 - 0.43 - 2.17 - 1.30 - 0.88 - 1.28 - 2.17 \\ &= -5.41 Kcal/mol \end{aligned}$$

Quite clearly, the NN model neglects contribution arising from non-local (beyond nearest neighbors) interactions along the helix.

Values listed in Ref. [24] have been obtained for salt concentration $c = 1$ MNaCl. To extend the calculations of ΔG, ΔH_Q and ΔS_Q to a wider range of experimental conditions, Ref. [24] also proposes an empirical salt correction that accounts for the effects that salt has on interaction energies (see Section 2.1.4). Empirical equations for ΔG and ΔS are

$$\begin{aligned} \Delta G^\circ_{37}[Na^+] &= \Delta G^\circ_{37}[1\ MNaCl] - 0.114 \times N/2 \times ln[Na^+] && (2.5)\\ \Delta S^\circ[Na^+] &= \Delta S^\circ[1\ MNaCl] - 0.368 \times N/2 \times ln[Na^+] && (2.6) \end{aligned}$$

where N is the total number of phosphates in the duplex and $[Na^+]$ the total concentration of monovalent cations. ΔH° is assumed to be independent trom $[Na^+]$, assumption that is valid for nucleic acids having total sodium concentrations above 0.05 M and below 1.1 M [24].

2.1.3 Melting temperature and sequence length

Increasing T causes the thermal energy to overwhelm stacking and pairing forces. As a conseguence, double helices become unstable and denaturate. The *melting temperature*, T_m, is defined as the temperature at which half of the double helices have unbound and split. In other words, T_m it is the temperature where *ds* and *ss* conformations have the same probability to happen.

Melting temperature is related with the energy needed for breaking bonds, and thus it depends on the number N of bases involved in the bond and on the ionic strength of the solution (see Sect. 2.1.4). Experiments performed with fully complementary sequences agree on revealing that for fixed ionic strength T_m is very sensitive to strands length. It is found that in 1 M NaCl T_m increases from $\approx 20-25°\text{C}$ for $N=6$, to $\approx 60-70°\text{C}$ for $N=20$, and saturates around 90°C for sequences with $N>25$ [17]. This behavior can be reproduced reasonably well by the thermodynamic description introduced above [24, 26]. In standard conditions, i.e. when $c_{DNA}=1$ M, the melting temperature is achieved when the difference in free energy between bonded and unbound DNA vanishes: $\Delta G=\Delta H-T_m\Delta S=0$. In these conditions T_m is

$$T_m=\frac{\Delta H}{\Delta S}=\frac{\Delta H_{INIT}-(N-1)\Delta H_Q}{\Delta S_{INIT}-(N-1)\Delta S_Q} \tag{2.7}$$

that for large values of N saturates to $T_m=\frac{\Delta H_Q}{\Delta S_Q}\approx 90°\text{C}$.

This saturation effect is surprising given the fact that the binding energy approximately scales with N, *e.g.* at room temperature ΔG grows from $\approx 10k_BT$ for a 6mer, to $\approx 20k_BT$ for a 10mer, to $\approx 45k_BT$ for a 20mer. But if on one side the binding energy increases, on the other side also the entropic penalty due confinement of sequences in a restricted volume portion grows with N. The two effect almost cancel each other when ΔG_Q is considered, leading to $T_m\approx 90°\text{C}$.

More in general, T_m also depends on the DNA concentration. It can be shown that [27]

$$\frac{1}{T_m}=\frac{R}{\Delta H}ln[c_{DNA}]+\frac{\Delta S}{\Delta H} \tag{2.8}$$

where R is the gas constant. Eq. 2.8 explicitly depends on the DNA concentration, and accounts for salt concentration via the term ΔS. Hence it enables to estimate the melting temperature of specific DNA sequences in a wide range of experimental conditions.

2.1.4 Melting temperature and ionic strength

When DNA is dissolved in water solution its phosphate groups dissociate a positive counter-ion (cation), and the backbone results to be negatively charged. Ionic strength I of a solution is defined as

$$I=\frac{1}{2}\sum_\alpha q_\alpha^2 c_\alpha \tag{2.9}$$

where q is the charge of counterions in unit of e (thus monovalent ions have $q=1$), c their molar concentration, and α the type of ion.

The concentration of counterions (the whole population of cations in solution) has a role in screening electrostatic interactions between DNA chains, and has therefore an influence in determining the melting temperature of the DNA oligomers. In this respect, we are actually more interested in determining the counterions concentration than the whole ionic strength of the solution. We assume that we only deal with monovalent ions, since the counterion we use is Na^+, and that each phosphate dissociates one cation - which is always true when the pH value of the solution is $4<pH<8$ [28]. Cation concentration is given by

$$c_{ions}=c_{DNA}+c_{NaCl} \tag{2.10}$$

where c_{DNA} is the DNA molar concentration, and c_{NaCl} the NaCl concentration of the solvent.

Screening effects may significantly increase T_m. For a 12mer, T_m is increased by nearly 30°C upon changing the added sodium from 50 mM to 1 M. For monovalent ions the overall ionic effect on free energy is found to be proportional to the number of phosphate groups on the helix, thus by tuning the ionic strength of the solution it is possible to control T_m of the system.

2.2 DNA-based nanostructures

The DNA molecule has peculiar properties of bonding, like recognition via WC pairing, self-assembly, reversibility, and tunability of interactions via regulation of sequence length, temperature and salt conditions. In the last three decades these remarkable features have been exploited to program interactions among specific DNA strands: rational design of sequences and self-assembly DNA properties enabled to produce molecular and supramolecular structures mutually interacting in a controlled way, and to engineer DNA materials [29]. DNA is employed in an increasing number of applications, and various structures have been constructed via self-assembly of rational designed sequence: geometrical shapes, 2D and 3D crystals, nanotubes, origami, up to active mechanisms. The existence of all these structures demonstrate the ability of controlling interactions at the molecular level. Some of them will be briefly described in the following, but we remand to recent reviews for a more detailed overview on the existing DNA structures [17, 29–31]. We focus here specially on those systems that lead to 2D and 3D crystal formation.

2.2.1 Structural DNA nanotechnology and DNA origami

The first structure constructed via programmed assembly is due to the work of N. Seeman, that in 1983 succeded in building a rational designed four-branched structure [32]. This is a replica of the Holliday junction, a structure that has transient existence as intermediate in replication or recombination processess (meiosi) of DNA molecules in living organisms. The junction is formed by four DNA strands, equal in length, each of them hybridized to two of the other strands. The resulting four double helices are arms of an interconnected structure having the shape of a star (see Fig. 2.4a).

Double stranded arms may be designed to terminate with a short single strand, called *overhangs* or *sticky-ends*. Complementary overhang sequences from distinct structures may hybridize, therefore inducing interactions between structures (see Fig. 2.4 b, c).

Star-shaped structures with an increasing number of arms have been built (up to 12 arms), together with a variety of geometrical shapes [31–34]. In Ref. [33] is reported the construction of a DNA cube. Each of the six faces of the object is a single-stranded cyclic molecule, doubly catenated to four neighboring strands, so that each edge contains two turns of the DNA double helix. The DNA cube is shown in Fig. 2.5b.

Ref. [34] uses a similar approach to make tetrahedra composed by four sequences. Like in the cube structure each single strand composes one of the faces and connects in the edges with the other three sequences, but in addiction, in this case the shape of the structure can be modified in a precise way and reversibly. One strand in the tetrahedron has been designed to include a hairpin loop opposite to a nick in the complementary strand. When the hairpin is formed in its closed state, the edge of the tetrahedron is contracted. Adding the "fuel" strand that hybridize the hairpin loop, instead, the edge extends. By varying

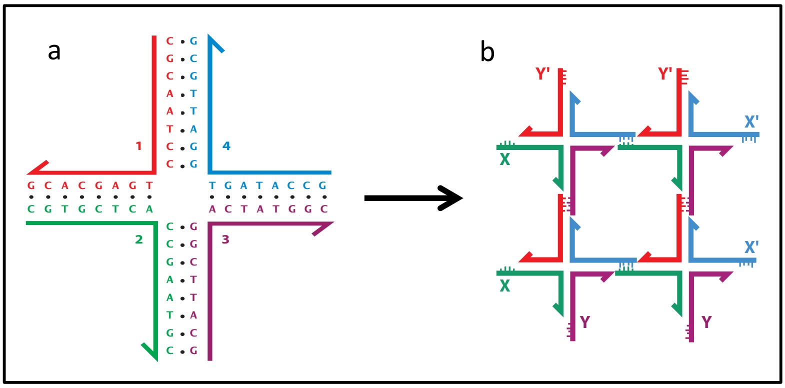

Figure 2.4: (a) star-shaped structure with four arms, obtained by hybridization of four sequences (red, blue, violet and green) (b) structures interacting via sticky overhangs; the choice of the overhang sequences determines the geometry of interactions between the arms of the structures (images from [31])

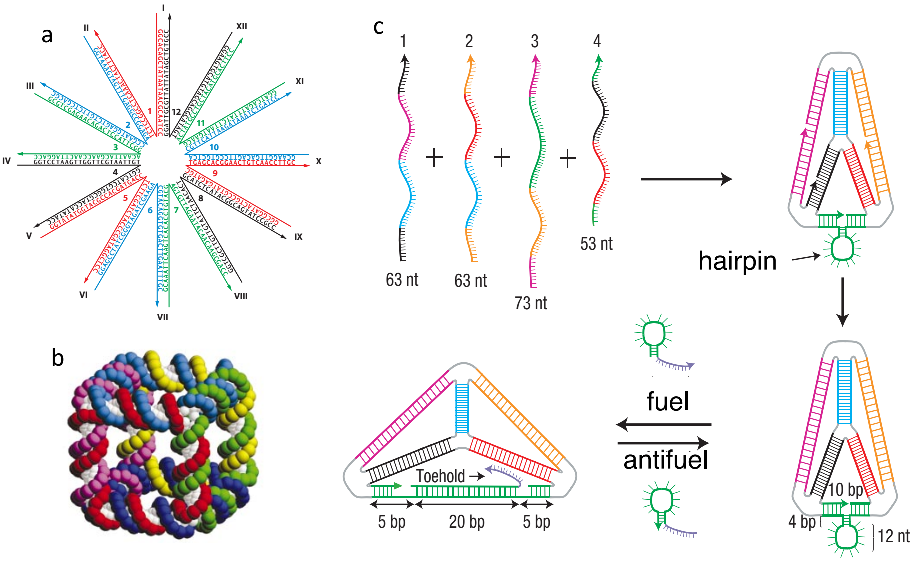

Figure 2.5: DNA structures built on rational design of sequences. (a) 12-arm star, (b) cube (both from [31]), (c) and (d) tetrahedra that can expand and contract one side depending on the concentration of fuel/anti-fuel oligomers [34]

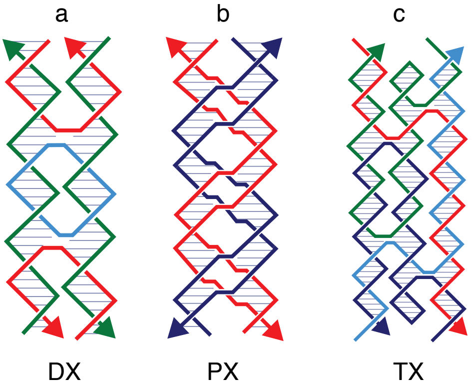

Figure 2.6: Double crossover (DX) structure and variants

the concentration of fuel and antifuel strands the shape of the structure can be continually changed between the open-closed configurations (see Fig.2.5c).

The common idea within all of these structure is that they are composed of many different DNA strands with unique sequences. To increase complexity of the structures, an increasing number of unique sequences is needed. Obviously, the need to synthesize large numbers (hundreds) of unique DNA strands poses a challenging design problem [35].

An alternative approach to the sequence design problem consists in designing basic DNA building units able to assemble into large three-dimensional structures. The most common building blocks are formed using an assembly called *double crossover* (DX), in which two or more double helices connect to each other twice through crossover points. Paired double strands are parallel and the ”tile” structure is rectangular in shape. Again, interactions between single units are introduced by sticky-ends located at their edges. The DX construction is shown in Fig. 2.6 together with its variants.

DX-type DNA stars have been used as building blocks to assemble 3D polyhedric structures (see Fig. 2.7). In Ref. [35] DNA stars having three arms are formed by paired double helices with $N = 22$ long arms and $N = 4$ long sticky terminals. Stars are symmetric for three-fold rotation, but they are not mirror symmetric, *i.e.* they are not flat. These units have an intrinsic curvature that is exploited to promote the polyhedron formation, each tile sitting at a vertex, and each branch associating with a branch from another tile. At the centre of the motif are three single-stranded loops (colored red in Fig.2.7a, c). The flexibility of the motif can be easily adjusted by varying the loop length, with increased loop length increasing tile flexibility. With the same method five-arms DX stars have been built and used to assemble more complex polyhedric structures [36].

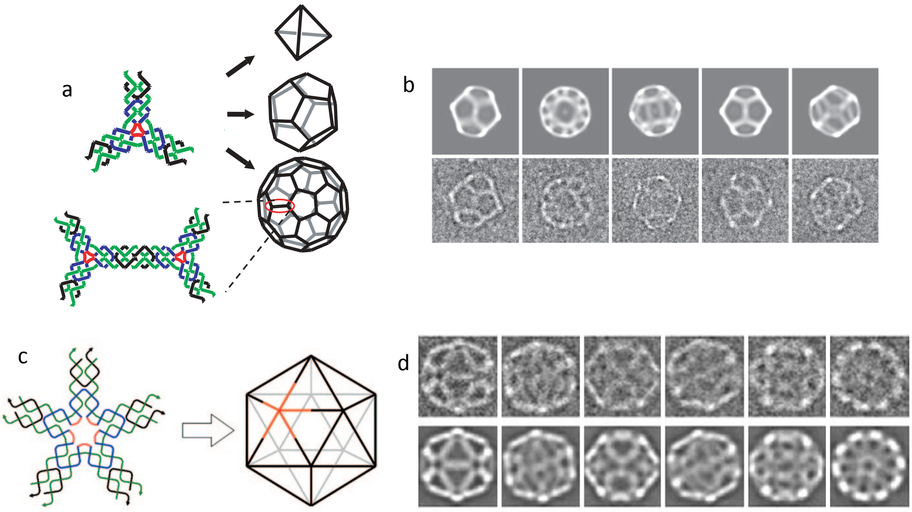

Figure 2.7: 3D polyhedra assembled from DX-type DNA stars. (a) varying the flexibility of the star arms different types of polyhedra can be assembled (b) cryo-TEM images of 3D DNA dodecahedron (lower) and computer reconstruction (upper) (c) sticky-ended five-arm-stars assemble into icosahedra (d) cryo-TEM images (upper) compared with computer-generated models (lower)

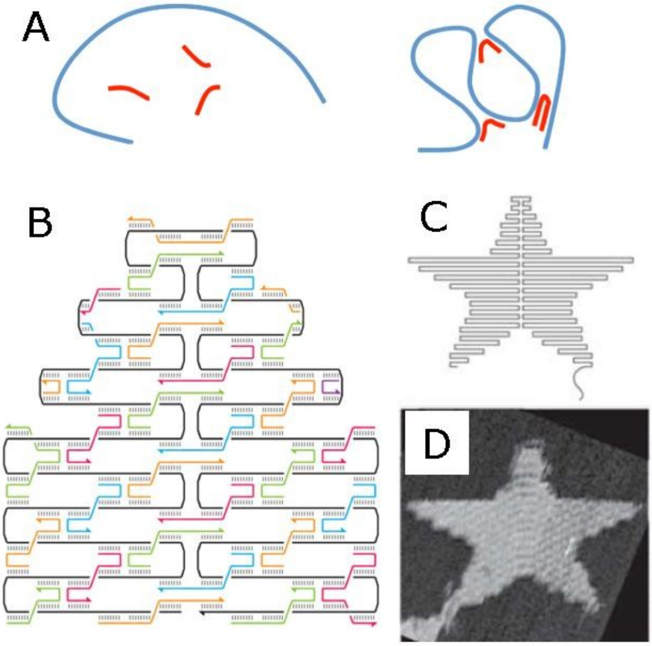

Figure 2.8: (a) Sketch of the basic idea of DNA origami: a long strand is stapled by oligonucleotides complementary to specific tracts along its sequence, and is folded into designed shapes (b), as complex as a star (c). (d) AFM image of the experimental realization of (c)

DNA origami

DNA structures discussed up to here derive from the assembly of multiple DNA strands which are relatively short in length, each of them being less than 100 nucleotides long. An alternative approach to form DNA assemblies is to program the folding of a long DNA sequence and guide it into specific shapes. This technique is called *DNA origami*.

In DNA origami short oligomers, called staples, are designed to hybridize specific sites of a long DNA single strand which is used as scaffold. The selective hybridization forces the long sequence to fold multiple times in a controlled way. The most commonly used scaffold is composed of $N \approx 7249$ bases, originated from the bacteriophage M13. Its sequence is well known and carefully sequenced. Staples length instead is usually comprised in the range $N = 20 - 40$ bases. Fig. 2.8 sketches the binding mechanism that leads to the formation of an origami DNA star [37].

Structures obtained with this technique are roughly 100×100 nm^2 in size, the limiting factor being the length of the scaffold. Spatial resolution of the motif is ~ 6 nm.

A limiting factor in the yield of the "non-origami" types of structures is that oligomers have to be carefully mixed in defined stoichiometry. The advantage of DNA origami is that, dealing with a very long strand, the production of the whole structure is less sensitive to stoichiometric ratios [37].

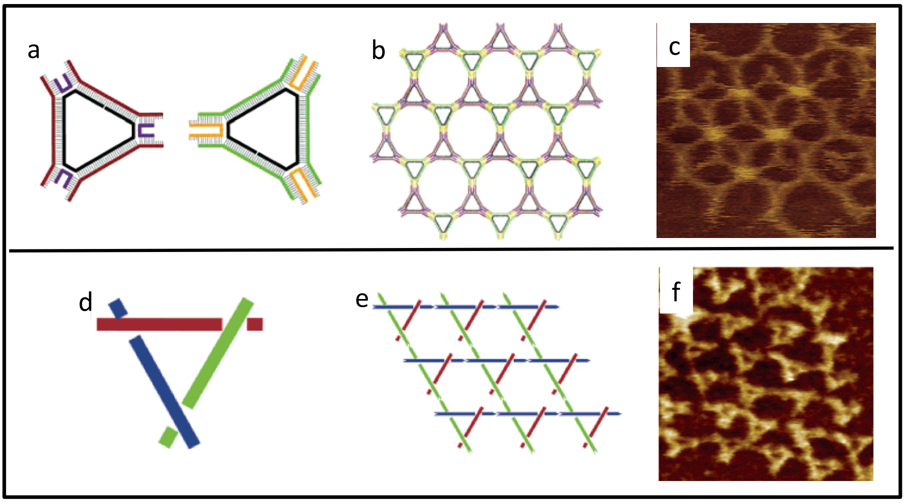

Figure 2.9: Design of a DNA triangles, sketch of the 2D lattice obtained using triangles as tiles, and relative AFM images

2.2.2 DNA crystals

Two-dimensional crystals

After using DNA to self-assemble static structures having geometrical shapes, the next logical step was to build interacting blocks that could grow in large ordered structures like 2D and 3D arrays. Branched structures can easily interact with each other using sticky-ends, but since branch orientations are rather flexible they don't allow the development of crystalline order [38]. More rigid structures are needed in order to provide bond directionality. Two main units have been adopted as tiles so far: (i) three single strands assembled into triangular shape, connected so that each side is composed by a double helix, and (ii) two or more double helices paired in the "double crossover" structure introduced in subsection 2.2.1 (Fig. 2.6). Both structures are flat and can grow microscopic two dimensional arrays.

In Ref. [39] an hexgonal lattice is obtained using two species of triangles with edges made of N=30 base pairs and two sticky groups of length N=4 per vertex. Triangles differs in the dangling sequences at the vertices, designed so that triangles of one group can interact with triangles from the other group only. The two sets of tiles have been prepared separately by annealing five different DNA sequences for each set. Upon mixing, triangles aggregate in the two-dimensional hexagonal lattice. The same type of crystal has been obtained using triangles of one type only, with sticky ends chosen so that each vertex would join with either one or two other triangles [40]. The two structures and relative crystals are shown in Fig. 2.9.

Several triangular tiles have been proposed, mainly differing in vertex design and thus is the way triangles connect to each other.

A more rigid structure that has been employed as tile block is the double crossover, which is approximatively twice as rigid as a double helix. In order to assemble in two dimensional patterns, the two parallel helices of the DX structures need to terminate with sticky ends that ensure end-to-end aggregation in a translated-type pattern. In Ref. [41] a structure with this scheme is obtained by mixing two DX tiles (A and B), each 36 base pair long with N=5 sticky terminals. Care needs to be taken to design the DX terminals, so

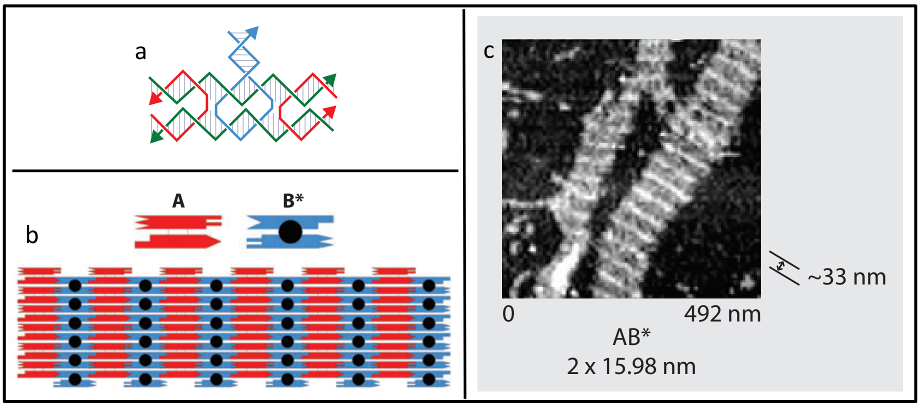

Figure 2.10: (a) DX+J structure. The blue protruding oligomers enables visualization of the lattice via AFM measurements (b) sketch of the 2D lattice obtained from the assembly of two types of tiles (c) AFM image of the structure sketched in (b)

that they properly match in helical phase and strand orientation. The resulting structure is a periodic two-dimensional lattice, made identifiable by AFM by adopting for one of the tiles a modified DX structure (DX+J) that contains an additional hairpin loop protruding on a side of the structure (see Fig. 2.10). Overall, the lattice is formed by parallel double helices, joined longitudinally through sticky-ends and transversely by crossover links.

Despite the various types of tiles proposed and the success in forming regular patterns, this class of two dimensional crystals is rather small, typically no more than a few micrometers in either dimension [31]. It became evident that the key ingredient to grow crystals in microscopic scale is to control the curvature of the growing structure, avoiding excessive flexibility between basic units and stress storage due to an impropriate matching of the helix turns. Structures that allow for this stress release produce large two-dimensional crystals, up to 1 mm in size [42]. Examples of large planar periodic structures are obtained by symmetric interactions of DX-type sticky DNA stars similar to those used to build polyhedric structures [42, 43]. In addiction to a major rigidity of the building blocks, provided by the DX construction, DX-type stars have been designed so that their arms stick end-to-end in such a way that each star interacts only with stars turned upside down. This generates planar aggregates of stars with alternate orientation, as marked by colors in Fig. 2.11b, e. Such a regular flipping of the aggregated units ensures perfect planarity, which appears to be the key element to produce macroscopically the large two-dimensional crystals obtained by this approach.

The last class of 2D crystals that we present here uses DNA origami to build rectangular tiles having a surface of $\approx 100 \times 100\ nm^2$. In principle the oligomer used as scaffold in the origami construction can be folded to assume a regular pattern, *i.e.* it would be a 2D crystal itself, but in order to extend the lattice surface origami tiles have to connect to each other. The key point to achieve such a connection is that two DNA origami units only cohere in the direction parallel to that of their helix axes. For this reason, if we want the crystal to extend in two dimensions, an origami tile must have helix axes propagating in two independent directions. Two independent types of tiles (A and B in Fig. 2.12) having this feature have been used in Ref. [44]. Both A and B units have two domains, one in a plane above the other, the purple rectangular domain lying above the green rectangular domain in both tiles. The two domains have orthogonal directions of propagation, and their sticky-ends have been designed to connect the green domain in tile

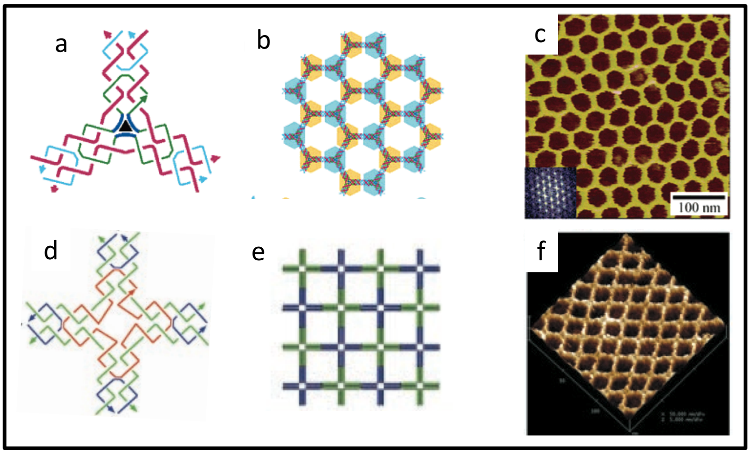

Figure 2.11: (a) DX-type DNA-star tile with sticky ends (b) Two families of such motifs can bind and yield a two-dimensional array. (c) AFM imaging of the structure in (b), the inset shows the associated Fourier pattern. (d) DNA 4 x 4 tile structure; two different tiles can produce a square lattice (e). (f) AFM surface plot of the structure in (e), edge size is 150 nm.

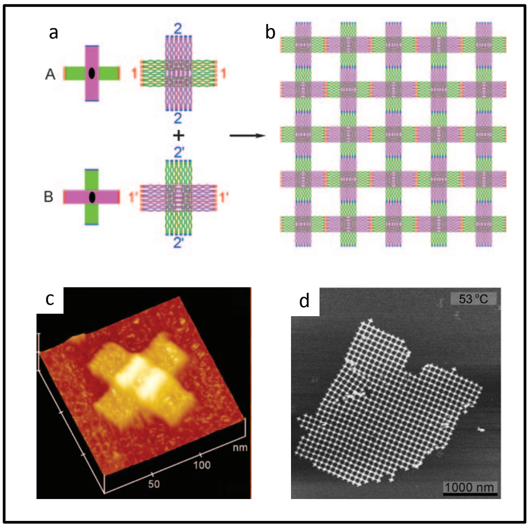

Figure 2.12: Origami tiles with orthogonal directions of propagation. (a) complementary tiles, A and B. The sticky-ends sets in A are labeled with the numbers 1 and 2, the complementary sticky ends are labeled 1' and 2' in B (b) sketch of the 2D lattice (c) AFM image of the A tile (d) AFM image of the lattice.

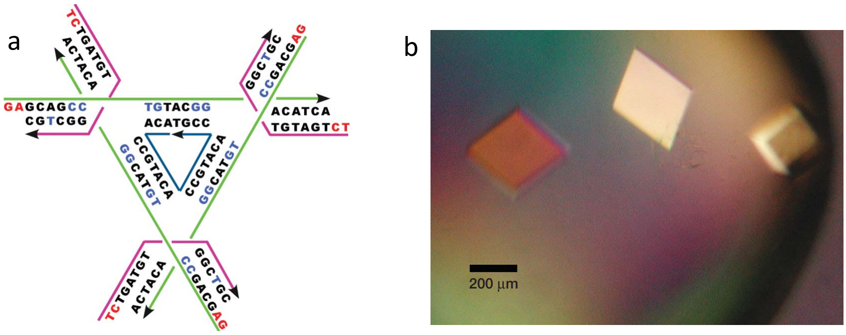

Figure 2.13: (a) Schematic of the tile triangle, composed of three unique DNA strands. Sticky-ends are shown in red letters. (b) optical image of 3D crystals made with triagles in (a). The rhombohedral shape of the crystals and the scale are visible.

A with the purple domain in tile B, so that the top layer of one tile bind to the bottom layer of the next tile. Since the two domains distort from planarity in opposite relative directions (for example, one curves up, and one curves down), adopting this arrangement planarity distortion cancel out, and an extended crystal with edge dimensions of $2-3\ \mu m^2$ is obtained (see Fig. 2.12).

Three-dimensional crystals

Three dimensional crystals assembled by rational design of DNA sequences have been obtained only recently [45]. If symmetry of building blocks and distortion release are important in 2D crystals formation, they are even more crucial in the formation of 3D crystals as an additional dimension is involved. Building blocks are again triangles that connect to each other via sticky-ends, but in this case the three double helices that form the triangle don't lay on the same plane. To enable the formation of a three-dimensional pattern, helices are tilted with respect to each other and overlap so that in vertex A (see Fig. 2.13) the helix 1 is above helix 2, in vertex B 2 is above 3 and in vertex C 3 is above 1. In order for the crystal to form, the total length of each helix is such to match an integer number of helical twists. Sticky groups instead, are chosen so to promote the adhesion of triangles oriented in the same way along the three directions. The results in Ref. [45] also enlighten how strongly the three-dimensional crystallization depends on the symmetry of the aggregating units. The terminals of the internal DNA strand (blue in Fig. 2.13) inevitably produce an asymmetry in the aggregate since one of the three helices forming the triangles necessarily has a chemical discontinuity (between the $3'$ and the $5'$ ends of the internal strand). Since the sequences in the internal triangle are all equal, such a nick is equally distributed in the three directions, a situation that somehow compensates the asymmetry. If this compensation is eliminated by choosing different sequences in the internal triangle, the resulting crystal size is severely reduced.

2.2.3 DNA hydrogels

DNA hydrogels are amorphous water-swollen cross-linked DNA networks typically extending over macroscopic volumes. Given their compatibility with biological environments and processes, they are potentially relevant in the context of drug delivery, cell culture and tissue engineering [17]. (the can hold some stress)

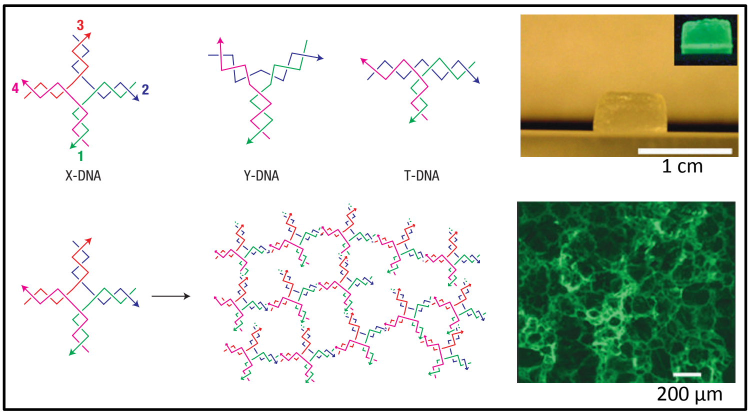

Figure 2.14: DNA hydrogels. Left panel: X- Y- and T-shaped units. Lowering the temperature, enzimatic reactions bond the star-shaped units into a network. Right panel: pictures of a gel. The inset shows the same gel tagged with fluorescent marker. Inside view of the network of star-particles.

Ref. [46] show that is possible to obtain DNA hydrogels from star-shaped structures similar to the ones discussed in section 2.2.1. Three types of star-shaped units have been used, differing in valence (number of arms) and/or geometry (Fig. 2.14). Units interact via sticky-ends with self-complementary sequences, which are the same in the three types of unit. After sticky-ends hybridization, enzymatic reaction of ligation makes the bonds permanent, and units connected into an amorphous network.

Chemical and physical properties of the hydrogels depend either on the shape of the star-like units and on their initial concentration. The degree of swelling of each hydrogel increases with the initial concentration of the structures, growing to volumes up to a factor 4 larger than the native. In general, hydrogel from valence four stars have the highest swelling degree and the strongest tensile modulus among all the DNA hydrogels. Hydrogels prepared with this technique also show remarkable memory effects. When synthesized in a specific shape, they can be dried and rehydrated several times repeatedly and returned to their original shapes.

Chapter 3

Experimental methods

3.1 Light scattering

The light scattering technique is based on the optical properties of matter, in particular on its ability to diffuse light. At the origin of the diffusion process are inhomogeneities in the refractive index of the medium: (i) a perfectly homogeneous medium only scatters forward, along the same direction of the incident beam (ii) if the medium is not homogeneous, instead, variation in the refractive index causes light to be diffused in all direction except for backward. Inhomogeneities in solids are due to the spatial arrangement of atoms into the crystalline lattice, while in fluids they can be due to the presence of suspended particles.

Any particle hit by an electromagnetic wave becomes itself source of a spherical electromagnetic wave having amplitude proportional to that of the incident wave and to the polarizability of the particle. The intensity profile scattered by a sample is determined by its internal structure and by interactions between its components. Using a reverse approach, the light scattering experiment measures scattered light to determine in a non-invasive way properties of the sample. In particular, static light scattering enables to measure static properties like shape and mass of the scatterers - or size of growing clusters - while with dynamic light scattering dynamic properties as diffusion coefficient and hydrodynamic radius R_h are measured.

In the following is given a description of Quasi-Elastic Light Scattering (QELS) process (for a detailed analysis see Ref. [47–49]). In QELS interaction between light and matter does not alter significantly the energy of the beam: the scattering process is linear, *i.e.* the the scattered field E_s is proportional to the incident field E_0, and it is only due to single scattering events.

Fig. 3.1 sketches a typical scattering experiment. An incident beam with intensity I_0 is focused on a sample, and the scattered light I_s is collected as a function of θ, the angle between the directions of incident and scattered beams. The region of the sample that is illuminated by the incident beam is called scattering volume. The particle has position $\mathbf{r}$ with respect to the origin O, while the collection point P has distance $\mathbf{R}$. k_0 and k_s are wavevectors of the incident and diffused beam, respectively. Their difference gives the scatting vector $\mathbf{q} = \mathbf{k_s} - \mathbf{k_0}$, which represents the transferred momentum in light-matter interaction. Since we are considering quasi-elastic interactions, the wavevectors are similar in modulus and so $|\mathbf{k_0}| \sim |\mathbf{k_s}| = \frac{2\pi}{\lambda}$ with $\lambda = \frac{\lambda_0}{n}$, where λ_0 is the beam wavelength in vacuum and n is the refractive index of the sample. The scattering vector $\mathbf{q}$ has modulus

$$q = |\mathbf{q}| = 2k \sin\frac{\theta}{2} \tag{3.1}$$

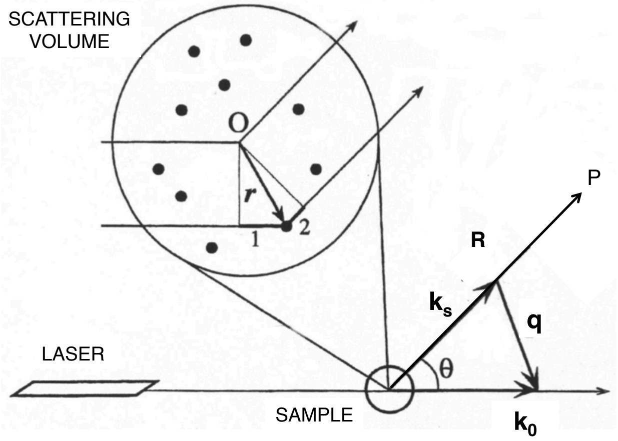

Figure 3.1: Light scattering experiment and wave vector q

3.1.1 Scattering by single particle

The rigorous solution to Maxwell equations under opportune boundary conditions enables to predict the scattering profile diffused by a particle with arbitrary shape and size, and it is known as Mie solution. In most cases though it is possible to introduce approximations. The two most popular approximations are known as Rayleigh and Rayleigh-Gans. The former is applied when the size of the particle is much smaller than the wavelength λ of the incident beam, while the latter also applies to particles having size comparable with λ, provided that the refractive index of the particle is similar to that of the medium surrounding it ($\frac{n_m}{n_p} \sim 1$). This section gives a theoretical introduction on the light scattering experiment, starting from the easiest approximation and adding progressively elements to generalize the results.

Small particle

Consider a spherical particle with radius a small with respect to the wavelength of the beam, so that the relation $qa \ll 1$ is true. Within this condition the particle can be viewed as a simple oscillating dipole, an approximation called Rayleigh theory. The incident electric field $\mathbf{E_0}$ has the form

$$\mathbf{E_0} = E_0 e^{i\omega t} e^{i\mathbf{k_0}\cdot\mathbf{R}} \tag{3.2}$$

The dipole induced in the particle is related to the incident field $\mathbf{E_0}$ and the polarizability α of the particle

$$\mathbf{p} = \alpha\mathbf{E_0} \tag{3.3}$$

The electric field of the scattered wave can be written in the general form

$$\mathbf{E_s} = \frac{\mathbf{k_s} \times (\mathbf{k_s} \times \mathbf{E_0})}{4\pi\epsilon(R - r_j)} \alpha e^{i\phi} \tag{3.4}$$

where $\epsilon = \sqrt{n}$ is the relative dielectric constant of the medium in which the particle is suspended, r_j and R are the positions of the particle and of the observation point respectively (see Fig. 3.1), and ϕ the phase of the wave.

Polarizability α of a spherical particle is given by

$$\alpha = 3V\epsilon_0\epsilon_{sol}\frac{\epsilon_P - \epsilon_{sol}}{\epsilon_P + 2\epsilon_{sol}} \tag{3.5}$$

where ϵ_0 and ϵ_{sol} are the dielectric constants of vacuum and solvent respectively, and V is the volume of the particle. If polarizability is isotropic and if the particle is homogeneous and made of material having index of refraction n_P, then α is simply

$$\alpha = (n_P^2 - n_{sol}^2)V \tag{3.6}$$

Notice that whenever particle and solvent had the same refractive index the solution would be optically homogeneous and no scattering effect would take place.

The phase contribution is given by the phase of the incident field at the position $\mathbf{r_j}$ plus a phase shift due to the propagation of the scattered field from $\mathbf{r_j}$ to $\mathbf{R}$

$$\phi_j = \omega t + \mathbf{k_0} \cdot \mathbf{r}_j + \mathbf{k_s} \cdot (\mathbf{R} - \mathbf{r}_j) \tag{3.7}$$

and can be rewritten introducing the scattering vector $\mathbf{q} = \mathbf{k_s} - \mathbf{k_0}$

$$\phi_j = \omega t + \mathbf{k_s} \cdot \mathbf{R} - \mathbf{q} \cdot \mathbf{r}_j \tag{3.8}$$

Substituting these quantities into Eq. 3.4, and under the approximation that $R - r_j \ll R$ the scattered field in the observation point R becomes

$$\mathbf{E_s}(t) = \frac{E_0}{4\pi R}\left(n_P^2 - n_{sol}^2\right) V \left(\frac{k^2}{n_{sol}^2}\right) e^{i(\omega t - \mathbf{k_0}\cdot\mathbf{R})} e^{-i\mathbf{q}\cdot\mathbf{r_j}(t)} \tag{3.9}$$

Notice that the amplitude of $\mathbf{E_s}(t)$ is independent from the particle position, while its phase is not. If the particle move with Brownian motion, as it usually happens for non-interacting particles in solution, then the scattered field has a randomly modulated phase that reflects the particle translation and rotation, and possibly internal motion when the scatterer has internal degrees of freedom. Since the scattered electric field depends on the particle position, its measurement can be used to extract informations about its motion. This is the bases of dynamic light scattering that will be further discussed in sections 2.1.3 and 2.1.4.

The experimentally accessible quantity though is the scattering intensity I_s

$$I_s = |E_s E_s^*| = I_0 \frac{V^2}{16\pi^2 R^2}(n_P^2 - n_{sol}^2)^2 \frac{k^4}{n_{sol}^4} \tag{3.10}$$

We point out that there is no contribution from the phase here. In principle, scattering intensity diffused by a single particle in a specific position $\mathbf{R}$ does not depend on the position of the particle into the scattering volume, and thus is constant. Scattering intensity has an intrinsic dependence from the incident wavelength, that is contained in the term $k^4 = (1/\lambda)^4$. According to this term, blue light is scattered more that red light, e.g. blue light of $\lambda = 450$ nm is scattered more intensely than red light of $\lambda = 670$ nm by a ratio $(670/450)^4 \approx 5$.

Large particle

Rayleigh-Gans approximation is only valid under the condition

$$2ka\left|\frac{n_{sol}}{n_p}-1\right| \ll 1 \tag{3.11}$$

where n_{sol} and n_p are the refractive index of the solvent and of the particle respectively. The approximation is true even when the size of the particle is comparable to the wavelength of the incident beam, provided that the refractive index of the particle is very similar to that of the solvent where the particle is dispersed (or generally of the medium surrounding the particle). Within this approximation the volume of the particle is ideally divided into small volumes, independent form one another, and each of them satisfying the Rayleigh scattering co-anchors. If Eq. 3.11 is true, the beam scattered from each element of volume must have phase and amplitude similar to that of the incident beam. In other words, the incident beam goes across the particle without being significantly distorted and based on the same principle, the intensity diffused by each point of the big volume travels across the particle without being affected from other volume elements. Ultimately, intensity diffused in a specific point results form interference between the contributions from each single small element of volume. The amplitude of the diffused field is the same for each volume element, while the phase term is different because every beam has a different optical path. The resulting scattered beam is obtained by integrating the phase contributions $e^{i\mathbf{q}\cdot\mathbf{r}}$ over the volume of the particle. The square modulus of this quantity is called *form factor* $P(\theta)$.

$$P(\theta) = |F(\theta)|^2 = \left|\frac{1}{V}\int_V dv e^{i\mathbf{q}\cdot\tilde{\mathbf{r}}}\right|^2 \tag{3.12}$$

where $\tilde{\mathbf{r}}$ indicates the position of the volume elements of the particle.

In conclusion, what we have is that the scattering intensity for a large particle is equal to the light scattered by a small particle multiplied to the form factor $P(\theta)$, that takes into account the microscopic structure of the particle

$$I_s^{LARGE} = I_s^{SMALL} P(\theta) \tag{3.13}$$

For any shape of the particle it can be shown [???] that the small angle limit of $P(\theta)$ is given by

$$P(q) \overset{q\to 0}{\to} 1 - \frac{k^2 R_G^2}{3} \tag{3.14}$$

where R_G is the radius of gyration of the particle, defined as

$$R_G^2 = \frac{1}{V}\int_V \tilde{r}^2 dv \tag{3.15}$$

$\tilde{r}$ being the distance of the volume element dv from the center of mass of the particle.

In the limit of small V, i.e. for small particles, i.e. for $qa \ll 1$ we fall in the limit of Rayleigh scattering and $P(\theta) = 1$. This also means that the light scattered by a small particle is independent from its orientation and it is the same for any $\mathbf{q}$. While the same is not true for large particles.

3.1.2 Macromolecules in solution

Scattering from non interacting particles

Consider a system composed of many particles dispersed in solution. When more particles are involved in the scattering process, the electric field diffused by the system is a sum of the electric fields scattered by each single particle.

$$E_s = \sum_j E_j \tag{3.16}$$

If the concentration of the particles is low enough, each scatterer is independent from the others and it scatters light independently. Assuming that the system is composed of N not interacting scatterers, $\mathbf{E_s}$ can be written as

$$E_s = e^{i(\omega t - \mathbf{k_s}\cdot\mathbf{R})}\sum_{j=1}^{N} A_j e^{-i(\mathbf{q}\cdot\mathbf{r_j}(t))} \tag{3.17}$$

In this case the amplitude A_j of each component is modulated by a phase term that in turn depends on the position of the particle. As a consequence, the resulting amplitude A is modulated by interference between all the components. Since particles are not still, but move all around with brownian motion, phases of the scattered waves detected in an observation point P continually change randomly, and cause the amplitude of the electric field to fluctuate. Obviously, fluctuations in the amplitude of the scattered field translate into fluctuations of the scattering intensity

$$\langle I_s\rangle = \langle |E_s E_s^*|^2\rangle = \langle |\sum_{j=1}^{N} A_j e^{-i(\mathbf{q}\cdot\mathbf{r_j}(t))}|^2\rangle \tag{3.18}$$

where $\langle\rangle$ indicate time average on I_s. Assuming that particles are identical, small, and non interacting, it is possible to introduce the simplification that A_j is the same for each scatterer, and phase contributions are independent from one another and randomly distributed. Under these conditions Eq. 3.18 becomes

$$\langle I_s\rangle = A_j^2\left\langle \sum_{j=1}^{N} e^{i(\mathbf{q}\cdot\mathbf{r_j}(t))}e^{-i(\mathbf{q}\cdot\mathbf{r_j}(t))}\right\rangle = A_j^2\left\langle \sum_{j,k}^{N} 1\right\rangle = I_0 N \tag{3.19}$$

In case of independent particles the cross product in Eq. 3.19 is always zero except for $j = k$. The summatory reduces to a sum of 1 terms and the time average of the phase terms $e^{i\delta}$ is thus equal to N, the number of particles that contributed to generate the diffused wave. Accordingly, the average intensity diffused from N independent scatterers is N times the intensity scattered by a single scatterer. For small particles $I_s(1)$ has the shape of Eq. 3.10, while for big particles the form factor has to be included. In conclusion the average scattering intensity can be written as:

$$\langle I_s(N)\rangle = N\langle I_s(1)\rangle P(\theta) \tag{3.20}$$

Scattering from an ensemble of particles can also be viewed in terms of Bragg scattering. By explicitly writing the amplitude in Eq. 3.17, and substituting the sum operation with an integral, the scattered field has the form

$$\mathbf{E_s}(t) = \frac{E_0}{4\pi R}\left(\frac{k^2}{n_{sol}^2}\right)\alpha\int \rho(r)e^{-i\mathbf{q}\cdot\mathbf{r}}dr \tag{3.21}$$

The quantity $\alpha \int \rho(r) e^{-i\mathbf{q}\cdot\mathbf{r}}$ express how much the volume is optically polarizable: α tells the polarizability of each component and the integral of the density $\rho(r)$ over the volume V tells how much polarizability is contained in the whole sample. We can write

$$\alpha \int \rho(r) e^{-i\mathbf{q}\cdot\mathbf{r}} \propto \int \epsilon_p(r) e^{-i\mathbf{q}\cdot\mathbf{r}} \tag{3.22}$$

The term on the right side of the proportionality can be thought of as a fourier transform on the dielectric constant ϵ. In this view, Eq. 3.22 tells the amount of fluctuations in the optical properties - which corresponds to the amplitude of fluctuations in the particles concentration - along the **q** direction. In other words, the scattered field provides informations about of the **q** component of the Bragg scattering due to the thermal fluctuations of the particles.

The system responds to thermal fluctuations via a proportionality constant that is called *susceptivity*, χ. The more the system fluctuates, the more is the amplitude of the scattered field, and thus of the scattering intensity.

$$\langle I_s \rangle \propto \chi^2 \propto |\epsilon_p(\mathbf{q})|^2 \tag{3.23}$$

Scattering from interacting particles

In a highly concentrated solution of particles, mutual interactions prevail on thermal fluctuations.Particles interact with each other, and as a consequence they assume positions that are correlated to one another. As a consequence, cross terms in Eq. 3.19 are not zero anymore, and the time average intensity is no more proportional to N. This reciprocal interaction is formally expressed through the structure factor $S(\theta)$, defined as

$$S(\theta) = 1 + \rho \int e^{i\mathbf{q}\cdot\mathbf{r}} g(r) d^3r \tag{3.24}$$

where $g(r)$ is the radial distribution function of the particles, integrated over the scattering volume.

The structure factor modulates the shape of the scattering intensity

$$\langle I_s \rangle = N I_s(1) P(\theta) S(\theta) \tag{3.25}$$

and in the limit of non interacting particles its value is $S(\theta) = 1$.

3.1.3 Characteristic time of intensity fluctuations

Consider a sample of macromolecules in solution. As discussed in the previous section, the relative displacement of the particles along the scattering direction causes scattering intensity to fluctuate. In the following we show how to extract informations on the particle dynamics on the bases of such fluctuations.

With reference to Fig. 3.1 we set an observation point P and we discuss the behavior of the scattering intensity $I(t)$ detected in P as a function of time. We call $I(0)$ the scattering intensity measured at $t = 0$. Intensity in P fluctuates, thus in general $I(t) \neq I(0)$. There is a critical time $t = \tau_c$ so that for $t \leq \tau_c$ intensity $I(t)$ changes only slightly with respect to $I(0)$, *i.e.* $I(t)$ and $I(0)$ are correlated. For $t \geq \tau_c$, instead, intensity $I(t)$ is not related to $I(0)$ anymore, meaning that the two intensity values are now uncorrelated. The characteristic time, or correlation time, τ_c, is a measurement of how long scattering intensity remains correlated.

τ_c depends on the size of the particles and on the scattering angle θ. To give a reasonable estimate of τ_c consider when the phase of the scattered beam varies of a quantity $\sim \pi$. This happens when $qx \sim \pi$, where x is the particle displacement along the scattering direction q. We can write x as a mean square displacement, so $q\sqrt{\langle \Delta r^2 \rangle} \sim \pi$. If particles are not interacting and move with brownian motion, then $q\sqrt{2D\tau_c} \sim \pi$, where D is the diffusion coefficient of the particle. The characteristic time is

$$\tau_c = \frac{1}{Dq^2} \tag{3.26}$$

This relation states that the characteristic time of fluctuations is proportional to the inverse of both the diffusion coefficient and the square of the scattering vector. Given it dependence on the scattering vector, for the same particle τ_c is longer for light diffused at low angles and shorter for light diffused at large angles. Dynamic light scattering technique measures correlations between intensity fluctuations in order to extract informations about the properties of the scattering particles.

Characteristic time and hydrodynamic radius

Translational diffusion coefficient D depends on friction coefficient f through the Einstein relation

$$D = \frac{k_B T}{f} \tag{3.27}$$

where k_B is the Boltzmann constant and T the absolute temperature. The friction coefficient depends on the geometry of the particle: for a spherical particle $f = 6\pi\eta a$, where η is the viscosity of the solvent and a the radius of the particle. In a real motion, though, the particle in its movement also involves molecules from the solvent, so the diffusion coefficient that is experimentally measured can be smaller than the real one. The associate radius is called hydrodynamic radius, R_h, and it is larger than the particle radius a. It is possible to generalize even more this formula to include also the case in which the particle is not spherical. To this aim an apparent hydrodynamic radius R_h^{app} is introduced. Independently to the shape of the real particle, this approach is consider an equivalent particle with volume equal to that of the real one, but with spherical shape and radius equal to R_h^{app}. The general form of Eq. 3.27 is thus

$$D^{app} = \frac{k_B T}{6\pi\eta R_h^{app}} \tag{3.28}$$

where D^{app} is the apparent translational diffusion coefficient.

3.1.4 Correlation functions

LS experiments are designed to make good use of the accessible information. Relevant insight in the system is obtained by studying the average scattering intensity as a function of the scattering vector and temperature (see section 1.2.1). Important informations are also obtained by studying the amplitude and extension of the fluctuations in the scattered field and intensity. Such fluctuations can be usefully characterized by the use of correlation functions

$$G_1(\tau) = \langle E_s(t) E_s^*(t+\tau) \rangle \tag{3.29}$$

The field correlation function show how long the field remains correlated to the value it had at $\tau = 0$. Given the shape of the scattered field in Eq. 3.17, it is possible to show that

$$G_1(\tau) = I_s e^{i\omega_0\tau} e^{-Dq^2} \tag{3.30}$$

There is a link between the field correlation function and the diffusion coefficient of the particles, from which it is possible to extract the value of the hydrodynamic radius. The experimentally accessible quantity though is not the scattered field, but the scattering intensity: it is not possible to measure experimentally the field correlation function, while it is possible to build the intensity correlation function, that in turn is defined as

$$g_2(\tau) = \langle I_s(t) I_s(t+\tau)\rangle \tag{3.31}$$

For large values of τ the intensity values are completely uncorrelated and Eq. 3.31 becomes $g_2(\infty) = \langle I_s(t)I_s(t+\tau)\rangle = \langle I_s\rangle^2$, that is simply the square value of the average intensity. For $\tau = 0$ instead, $g_2(0) = \langle I_s^2\rangle$. $g_2(\tau)$ is then a decreasing function that goes from $\langle I_s^2\rangle$ to $\langle I_s\rangle^2$.

Fluctuations in scattering intensity are determined by the relative motion of the N scatterers that contribute to the scattered beam. Thus the distribution of the intensity values reflects the motion of the scatterers. For independent scatterers, scattering intensity is characterized by a gaussian statistic, and the correlation functions G_1 and g_2 are connected through the Siegert relation

$$g_2(\tau) = I_s^2(1 + \gamma |g_1(\tau)|^2) \tag{3.32}$$

where $g_1(\tau) \equiv G_1(\tau)/G_1(0)$ is the normalized field correlation function, I_s the average scattering intensity, and γ is called *efficiency factor* or *contrast*. For macromolecules in solution

$$g_1(\tau) = e^{-Dq^2\tau} = e^{-\tau/\tau_c} \tag{3.33}$$

and Eq. 3.32 becomes

$$g_2(\tau) = I_0^2(1 + \gamma e^{-Dq^2\tau}) \tag{3.34}$$

3.1.5 Stretching exponent

Polydispersity is an indication of the size distribution of the particles in the sample. It can be due to impurities or inhomogeneities or deterioration of the sample, and thus we would like to avoid it, o it can be due to aggregation processes going on into the system. In this case we can use polydispersity to study the evolution of the system.

A continuous distribution of particle sizes gives

$$|g_1(\tau)| = \frac{1}{I_0}\int I(D) e^{(-Dq^2\tau)} dD \tag{3.35}$$

where $I(D)dD = N(D)I_0(D)dD$ is the scattering intensity from particles having diffusion coefficient in the range $[D, D + dD]$, $N(D)dD$ is the number of these particles in the scattering volume and $I_0(D)$ is the scattering intensity from each of them. The broadening of sizes brings about a broadening of characteristic times τ_c. It is possible to show [50] that under some approximations and for large values of τ the relation

$$|g_1(\tau)| = I_0 exp\left[-\left(\frac{\tau}{\tau_c}\right)^{\alpha}\right] \tag{3.36}$$

When studying an exponential decay $E(\tau) \propto exp(-\tau/\tau_c)$ there are three equivalent ways to determine τ_c

1. the value of τ at which $E(\tau)$ is equal to $1/e$: $E(\tau_c) = 1/e$
2. the value that the derivative has in the origin: $\left[\frac{dE}{d\tau}\right]_{tau=0} = -\frac{1}{\tau_c}$
3. the value of the integral over the positive semi-axis: $\int_0^{\infty} E(\tau)d\tau = \tau_c$

Not all of these relations holds with stretching exponents. The τ_c we discussed up to now is the one of 1. The second definition instead in meaningless since the derivative of a stretching exponent diverges in the origin. This lead to the conclusion that the stretching exponential function is not a good description for phenomena with small τ. The third definition brings to a different value of τ. We call $\langle\tau_c\rangle$ the integral of the stretching exponential. This is related to τ_c by [51]

$$\langle\tau_c\rangle = \int 0^{\infty} exp\left[-\left(\frac{\tau}{\tau_c}\right)^{\alpha}\right] dt = \frac{\tau_c}{\alpha}\Gamma\left(\frac{1}{\alpha}\right) \tag{3.37}$$

τ_c has the meaning of an average of characteristic times of elementary contributions averaged on their distribution.

Stretch exponential relaxation can also be found in perfectly monodispersed systems when the relaxation processes depend on some local variables that may not be uniform across the system. for example in a system with large density fluctuations the diffusion of a single scatterer may be different from in different locations of the sample. Another example is when monodispersed scatterers are bound to each other or to a different substrate with a variety of energies. In this case the activation processes will be different depending on the specific local energy. Hence, stretch exponential relaxations generally indicate that the system is characterized by statistically distributed properties, that could either concern the structure of the scatterers (size or shape polydispersity) or characterize their collective state (energy, cluster size, or local density distributions).

3.1.6 Coherence area and efficiency factor

Intensity scattered by a sample in a specific position in space has time fluctuations. This is true for any point in the region around the sample, so the scattered field is a spatial pattern of fluctuations known as *speckle pattern.* Intensity distribution at any time t depends on the position of the particles at that specific time. Since particles move continually, the speckle pattern changes too. Suppose that at a specific time t_0, in the specific position P a certain intensity I is measured. It is reasonable to imagine that points close to P have a very similar intensity, since the phase contribution of the waves scattered in the region around P don't change significantly. There is a region in space, characterized by the same value of scattered intensity. This region is called *coherence area.* An ideal scattering experiment would measure the intensity of a single coherence area. In this case the efficiency factor would be $\gamma = 1$. Very often intensity of single area is too low to be measured, and it is necessary to collect light from more coherence areas.

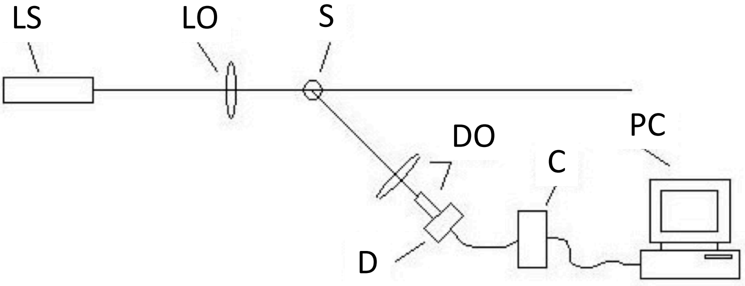

Figure 3.2: Scheme of a light scattering apparatus

If light coming from too many coherence areas is collected, though, the collected signal becomes an average of the fluctuations that we would like to measure. In this scenario the efficiency factor decreases proportionally to the number of coherence areas that are detected, following the relation

$$\gamma \propto \frac{1}{N} \tag{3.38}$$

with N number of coherence areas. Depending on the experimental conditions is thus necessary to find a compromise between these quantities.

3.2 LS Setup

The experimental apparatus for light scattering measurements is composed of the following parts: light source (LS), usually a LASER; launch optics (LO) to optimize shape and size of the LASER beam on the sample (S); detection optics (DO), to detect the light scattered by the sample and couple it with a detector (D); correlator (C), an electronic board connected to a personal computer (PC) to determine statistical properties of the scattering intensity, specifically its time average and time correlation function.

Measurements in this thesis have been performed with a light scattering apparatus (ST100, Scitech Instruments, CA) able to simultaneously measure the average scattered intensity (static light scattering) and its time correlation function (dynamic light scattering) as a function of the scattering angle, and customized to measure samples with small volume. The instrument is shown in Fig. 3.3

3.2.1 Light source and launch optics

The light source employed is a solid state Nd-YAG (Neodynium - Yttrium Aluminum Garnet) LASER (Compass 315M, Coherent) emitting light at $\lambda = 532\ nm$, with vertical polarization. The power of the beam can be tuned in the range $70-150\ mW$ via analogical control. The beam has divergence < 2.2 mrad and waist of $170 \pm 20\mu$ m placed at 3 ± 2 cm out of the LASER window.

The light source is external to the scattering apparatus and is connected to the instrument via a monomode polarization maintaining optical fiber. An FC/APC coupler (OZ Optics) couples the LASER and the connectorized optical fiber. At the other end of the fiber, a lens focuses the incident beam on the sample, which is hold into the optical chamber of the instrument.

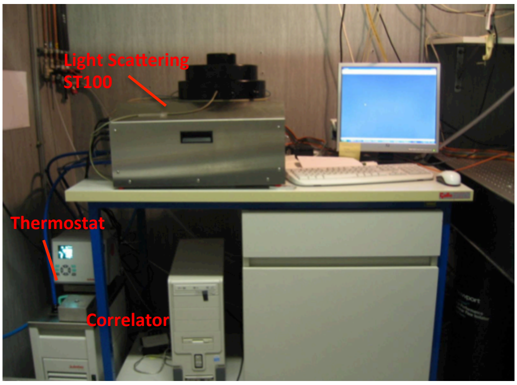

Figure 3.3: Light scattering apparatus

3.2.2 Thermalization of the system

Diffusion coefficient D depends on the temperature both explicitly (see Eq. 3.28) and through viscosity. Experimental values of viscosity are well fitted by the function $\eta = ae^{b/T}$. In water, for temperatures close to room temperature, the T/η factor in Eq. 3.28 varies of about 3% for Kelvin degree. It is thus important to stabilize and precisely control the temperature of the sample. In ST100 this issue is achieved by plunging the sample into a silicon oil bath that completely fills the optical chamber and acts as thermal bath for the sample. The oil (specific weight $= 0.915$, $n = 1.39$) is thermalized and continually fluxed in by an external thermostat and a pump (F25-HE Julabo). It is possible to set the temperature of the external bath or that of the optical chamber, monitored via a PT100 thermistor temperature sensor. In both settings the target temperature remains stable within $\pm 0.01°$C.

3.2.3 Detection optics

Detection optics collects the light scattered by the sample, selecting the contribution of a specific number of speckles. Using a multimode optical fiber as detection optics, the number of detected speckles (i.e. coeherence areas) is equivalent to the number of modes transmitted by the fiber [52].

In the ST100 apparatus a system of mirrors drives the scattered light to a non-polarized optical fiber that at $\lambda = 532$ nm detects three modes, i.e. three speckles. Mirrors are arranged to collect scattered intensity at an angle $\phi = 5°$ below the scattering plane, setting adopted by the constructor of the instrument to reduce the detection of straylight eventually present in the optical chamber. Straylight would superimpose to the scattered light, affecting the real signal and reducing the quality of the measurements. Using the instrument we noticed that this setting on one side actually reduces the contribution to the signal due to reflections on the cell walls, but on the other side it forces to adopt approximations that are reliable for high angles, but problematic for low angles.

The mirror system can rotate exploring the range $0° - 180°$, but since light is collected 5° below the scattering plane, the equivalent range of explored scattering angles is $\theta = 5° - 175°$. Angular rotation is provided by a stepper motor and controlled by a relative encoder.

In the optical chamber there are three other collection points, fixed and collecting light in the scattering plane. One of these is dedicated to collection of transmitted light, while the other two are positioned at $\theta = 90°$ with respect to the incident light, and thanks to polarizers detect light diffused with vertical and horizontal polarization respectively. All the collecting fibers are non-polarization maintaining and collect three modes.

3.2.4 Detection and analysis of the signal

The collected signal is detected by a photomultiplier tube, then amplified and translated into digital signal by an operational amplifier. To reduces noises and afterpulses that may happen during the detection and amplification processes, the collected beam I_s is split in two identical signals I and j by a beamsplitter. The two signals are detected and amplified independently, and used to calculate the intensity cross-correlation function

$$g_2(\tau) = \lim_{x \to \infty} \frac{1}{2T} \int_{-T}^{T} I(t) J(t+\tau) dt \tag{3.39}$$

which measure the correlation between the I signal and the J signal. We point out that I and J carries the same information about the sample since they come from the same I_s. The only differences between I and J come from the detection and amplification processes, and must be uncorrelated. Thus, the cross-correlation function between the two signals eliminates these spurious contributions and the resulting data are more clean. Correlation functions are calculated using the four channel digital correlator Flex03LQ-1, that can calculate two cross-correlation functions at the same time (using two channels for each function). The shortest τ that Flex03LQ-1 has access to is 1.6×10^{-7} s.

The control software for ST100 instrument is furnished with the instrument. Both static and dynamic measurements can be performed in the angular range $\theta = 5° - 175°$. In order to perform long runs of measurements, also including temperature variation, a routine of operations has been developed using the software *Automate*. The routine runs alternatively the ST100 acquisition software and temperature control software enabling to acquire long runs of measurements.

3.3 Determination of the phase diagram via volume measurements

When phase separation takes place into a system, the system divides itself between two coexisting phases having volumes and concentrations that differ from the native one. Volumes and concentrations of the new coexisting phases are not independent from each other. They are instead connected by a specific relation, called *lever rule*, that origins from conservation of the total mass. We assume the total volume of the sample, V, to remain constant. Subscribed "+" and "−" in the quantities below stay for the dense phase and diluted phase respectively. The total mass of the system must be conserved, so

$$m_0 = m_+ + m_-$$

that can be written as

$$c_0 = c_+ \phi_+ + c_- \phi_-$$

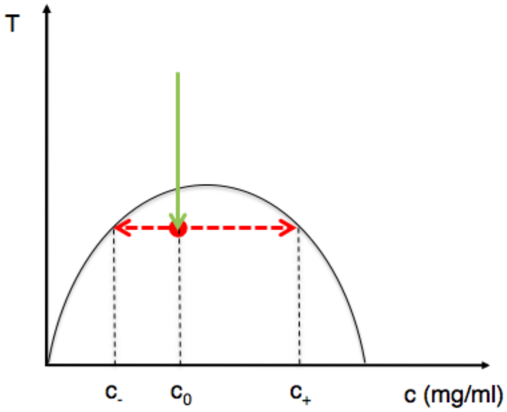

Figure 3.4: Liquid-gas-like phase diagram and lever rule construction.

where c_0 is the native concentration, and $\phi_+ = \frac{V_+}{V}$ and $\phi_- = \frac{V_-}{V}$ are the volume fractions of the two coexisting phases. As V is conserved, we can write $\phi_- = (1 - \phi_+)$, thus

$$c_0 = c_+\phi_+ + c_-(1 - \phi_+)$$

from which we obtain

$$\phi_+ = \frac{c_0 - c_-}{c_+ - c_-} \tag{3.40}$$

The volume fraction of the dense phase is given by the difference between the native concentration and the concentration of the diluted phase divided by the difference between the two new concentrations. A similar relation holds for the volume fraction of the diluted phase:

$$\phi_- = \frac{c_0 - c_-}{c_+ - c_-} \tag{3.41}$$

Equations 3.40 and 3.41 are called *lever rule*. A graphic construction of the rule is shown in Fig. 3.4.

Measurement of the volume fractions enables to determine the concentrations of the two coexisting phases.

3.4 Electrophoretic gel

Gel electrophoresis enables to sort molecules having different sizes. The technique is based on the principle by which applying an electric field on a disperse solution of charged molecules causes the molecules to migrate in the fluid, driven by their charge. This phenomenon, called electrophoresis, is exploited to induce migration of molecules into a porous medium, usually a gel. Size of the gel pores forces the sorting of molecules depending on their size or, more specifically, on their length: short molecules are small and move faster, because it is easier for them to go through the gel pores, while long molecules move slower. In this context, the gel is used as a matrix to contain and then separate

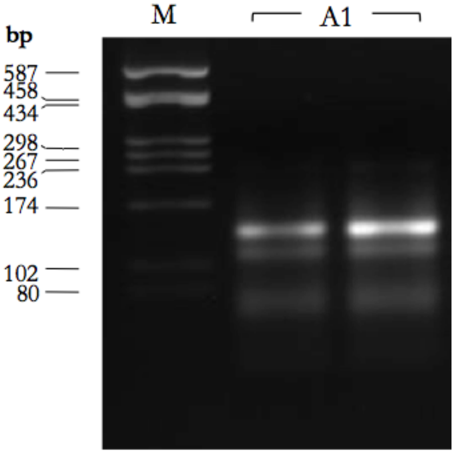

Figure 3.5: Representative DNA separation in Agarose gel.

the target molecules. Provided that their charge-to-mass ratio is constant, different sized molecules form distinct bands on the gel, one band for each size (see Fig. 3.5).

Two types of gel are commonly used: polyacrylamide and agarose gels. In both cases pore size is determined by the concentration of the element. A single gel can host several samples, each of them running along its own lane, so multiple experiments can be run simultaneously. One of the lanes is usually filled with a marker, a reference sample composed by a set of molecules whose mobility is well known. Molecules are tagged/marked with some fluorescent dye usually absorbing in the UV-spectra and emitting in the visible-spectra, enabling the detection of the bands under UV-light.

3.4.1 Gel electrophoresis on DNA molecules

Gel electrophoresis can be applied to sort DNA molecules depending on their length. Type and concentration of the gel are chosen depending on the length of the chains. In addiction, gels can be run in denaturing or non-denaturing conditions, meaning that DNA oligomers can run as single chains or as duplexes. Since stiffness of DNA chains significantly changes depending on whether they are hybridized or not, their electrophoretic mobility into gel is also strongly affected. When electrophoresis is performed in non denaturing conditions, the mobility of single strands is larger than that of double strands. By adopting the same non denaturing conditions, it is possible to measure the electrophoretic mobility of DNA structures with two- or three-dimensional geometry, and it is found that their mobility reduces with increasing geometrical complexity [53, 54].

Polyacrylamide gel and PAGE purification

Polyacrylamide (PA) gels are obtained by mixing acrylamide with a cross-linker, thus producing mesh networks of polyacrylamide. Samples usually run in denaturing conditions and sequences are tagged with intercalating fluorophores. The pore size is uniform along the gel volume and it is controlled by the agarose/cross-linker ratio. Increasing the cross-linker concentration leads to more connected networks, with small sized pores. For this reason PA gels can be used to sort DNA sequences within a wide range of lengths, depending on the gel structure. A proper choice of the pore size enables to resolve oligomers that differs in length for one base only.

Given their high resolution ability, PA gels are be used to purify DNA oligomers after synthesis. In DNA synthesis process, chains are literary grown up starting from the first nucleobase of the sequence and adding one oligonucleotide after the other. Each nucleobase is bonded to the growing chain via enzymatic reaction before adding the next nucleobase. In this process errors may occur and shorter DNA oligomers, with missing bases in the sequence, may grow together with the full-length chains. Poly Acrylamide Gel Electrophoresis (PAGE) is used to purify the product of the synthesis by sorting the full length ologomers from all the others. This purification procedure is according to the standards of molecular biology. PAGE purification process guarantees up to $90 - 95\%$ of full length product.

Agarose gel

Agarose is composed of long unbranched chains of uncharged carbohydrate, that form a gel structure even without additional cross-linkers. Agarose gels do not have a uniform pore size, thus they are not suitable for purification purposes. Since they have larger pores than PA gel, though, Agarose gels enables to sort macromolecules and macromolecular complexes. Within the DNA context, Agarose gels are used to sort long DNA sequences, starting from ≈ 50 bases to longer sizes. Again, the average pore size depends on the density of the gel, with pore size decreasing with increasing agarose percentage in the compound.

Agarose gels can be run in both denaturing and non-denaturing conditions, and it is thus more indicate to run DNA complexes with non-linear shapes. DNA running on Agarose gels is usually tagged with Ethidium Bromide (EtBr), a fluorescent tag that intercalate into the major groove of DNA double helix. EtBr fluoresce with an orange color, intensifying almost twenty-fold after binding to DNA and thus allowing for DNA detection.

3.5 Melting temperature

Melting temperature T_m is defined as the temperature where half of the DNA double helices have unbound and split. We introduced this quantity already in section 2.1.3, within the context of DNA hybridization energy. Here we focus on the experimental procedure to measure it.

Melting temperature can be easily measured by monitoring absorbance, or fluorescence, or with calorimetric methods [26]. Fig. 3.6 shows an example of UV absorbance and the corresponding fraction of single strands plotted as a function of T. T_m is determined as the middle point of single strands to double helix transition.

Within the context of this work, absorbance measurements were performed with a commercial instrument (LightCycler480, Roche) that measures fluorescence emitted in the interval 483-533 nm by a saturating fluorescent dye furnished with the instrument (High Resolution Melting Dye, Master Mix 2X). The dye only fluoresces when bond to double stranded DNA. As a consequence, when the dye is added to a DNA sample, its fluorescence intensity I_F is detectable only when the strands are hybridized. As T becomes larger than T_m, duplexes unbind and the fluorescence emission drops. Hence, the measurement of I_F vs. T light enables to assessing the fraction of bound strands

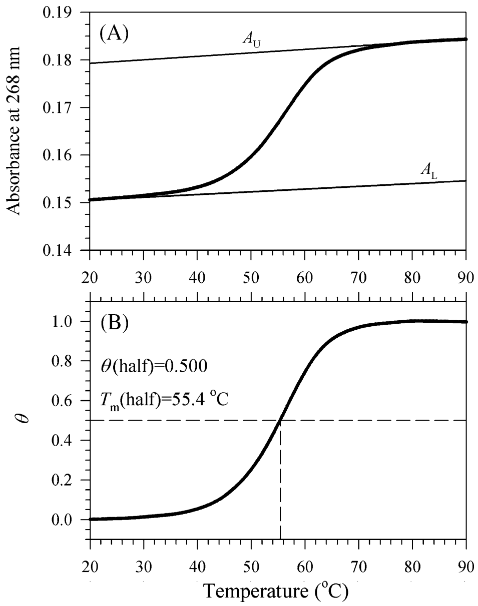

Figure 3.6: (A) Melting curves determined via UV absorption, (B) corresponding fraction of single strands and estimate of T_m [26].

and to determine the melting temperature, defined as the temperature where half of the double helices have unbound.

Using a saturating dye ensures that measurements are quantitative. Since each DNA double strand is equally (totally) filled with dye molecules, all the double helices involved in the process fluoresce with the same amount of light, and the fluorescence intensity is representative of the amount of arms, i.e. of the amount of structures.

3.6 UV absorption

Every molecule has its own electronic cloud with energetic levels characteristic of the molecular specie. When light of the right frequency, i.e. of the right energy, is absorbed, the molecule can be excited to one of its higher energy levels. This phenomenon is called *absorption* and it is foundation of the homonym spectroscopic technique used to identify and quantify elements, e.g. components dissolved in solution. Since each element has its own characteristic absorbance peaks at specific wavelengths, the absorption spectrum of a sample can tell which elements a given sample is composed of. In addiction, as the fraction of light absorbed is proportional to the number of absorbing molecules [55], the absorbance value at a specific wavelength can be used to quantify the amount of molecules in solution.

The connection between absorption A and sample concentration c is described by the *Beer-Lambert* law. Imagine to shine light with intensity I_0 at wavelength λ on a solution prepared at concentration c. The beam impinges on the sample for path length of l cm, and the light that is not absorbed by the sample emerges with intensity I. *Beer-Lambert*

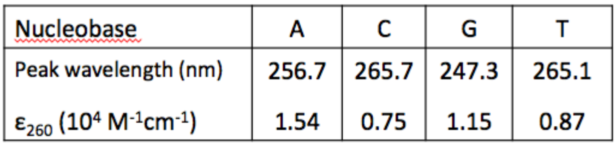

Nucleobase	A	C	G	T
Peak wavelength (nm)	256.7	265.7	247.3	265.1
ε_{260} (10^4 $M^{-1}cm^{-1}$)	1.54	0.75	1.15	0.87

Table 3.1: Peak of maximum absorption and molar extinction coefficient for DNA nucleobases.

law connects all these quantities in the following relation:

$$A(\lambda) = -\log \frac{I}{I_0} = c\epsilon(\lambda)l \tag{3.42}$$

where ϵ is the molar extinction coefficient in unit of $\mathrm{M}^{-1}\mathrm{cm}^{-1}$.
The range in which the relation between absorbance and concentration is linear, i.e. in which the Beer-Lambert law is valid is from $A \approx 0.1$ to $A \approx 0.8$. Out of this range linearity is lost.

3.6.1 UV absorption of DNA molecules

The key quantity to convert absorbance into concentration is the molar extinction coefficient ϵ. Absorption experiments on DNA nucleobases show that they have maximum absorbance peaks at $\lambda \approx 260\ nm$ and that their molar extinction coefficient ranges from $0.75 \times 10^4\ \mathrm{M}^{-1}\ \mathrm{cm}^{-1}$ to $1.54 \times 10^4\ \mathrm{M}^{-1}\mathrm{cm}^{-1}$ [55, 56]. (see Tab. 3.1)

Models allow to predict ϵ for any oligomer on the base of its sequence [56]. Long DNA chains usually contain every type of nucleobase in the same amount, so for any nucleobase the average molar extinction coefficient $\epsilon = 1.1 \times 10^4\ \mathrm{M}^{-1}\mathrm{cm}^{-1}$ is generally adopted. For short DNA chains, though, this is not generally true and the molar extinction coefficient of the chain should be calculated by weighting the ϵ of each type of nucleobase for its amount in the sequence [56].

$$\epsilon_{chain} = \sum_{i=A,T,C,G} N_i \epsilon_i \tag{3.43}$$

Despite the fact that this base-composition model discards interactions between bases, in most cases its predictions are supported by experimental results so this model is often preferred to the nearest-neighbor because of the minor number of parameters involved in the calculation of ϵ.

The extinction coefficient of double stranded DNA is minor than the sum of the extinction coefficients for the composing two single stranded DNAs [57]. Consider two single stranded oligodeoxynucleotides, S1 and S2. When they hybridize and form the DNA duplex, D their extinction coefficient decreases due to interactions between neighboring bases [57].

$$\epsilon_D < \epsilon_{S_1} + \epsilon_{S_2} \tag{3.44}$$

The extinction coefficient of the duplex, ϵ_D, can be estimated from the extinction coefficients of both strands, ϵ_{S1}, ϵ_{S2}, and hypochromicity, h,

$$\epsilon_D = (1-h)(\epsilon_{S1} + \epsilon_{S2}) \tag{3.45}$$

The value of $1-h$ is the fraction of absorbance that remains when the single strands anneal to form the duplex,

$$1-h = \frac{A_D}{(A_{S1}V_{S1}+A_{S2}V_{S2})/(V_{S1}+V_{S2})} \tag{3.46}$$

where A_D is the absorbance of the duplex solution, A_{S1}, A_{S2} are absorbance values of the single strand $S1$ and $S2$ solutions, respectively. Volumes V_{S1} and V_{S1} of $S1$ and $S2$ strand solutions.

Once the coefficient extinction at $\lambda = 260$ nm is known it is possible to convert measured absorbance values into concentrations. Recently a method to calculate ϵ in a range of λ starting from ϵ_{260} has been proposed, allowing to predict the absorbance spectrum in a wide range of wavelengths [56].

Often an effective extinction coefficient $\epsilon^\star = 1/\epsilon$ is used. The accepted $\epsilon^\star$ values for DNA are $\epsilon^\star_{ss} = 30$ ng cm/μl and $\epsilon^\star_{ds} = 50$ ng cm/μl for the single strand and double strand DNA respectively.

$$\epsilon^\star_{ss} = \frac{1}{\epsilon_{ss}} = \frac{1}{1.1\times 10^4} Mcm = \frac{1}{1.1\times 10^4} \times 330\ \mu g\ cm/\mu l = 30\ ng\ cm/\mu l \tag{3.47}$$

To check the purity of DNA samples, absorbance at $\lambda_{DNA} = 260$ nm is usually compared with absorbances at the maximum absorbance peaks of proteins $\lambda_{proteins} = 280$ nm. DNA samples are considered pure for $Abs_{260}/Abs_{280} > 1.8$ [58]. The Abs_{260}/Abs_{230} is used as a secondary measure of nucleic acid purity. Expected 260/230 values are commonly in the range of 2.0-2.2. If the ratio is appreciably lower than expected, it may indicate the presence of contaminants which absorb at 230 nm.

3.6.2 Experimental setup

To perform experiments within the linear range it is possible to act on the sample concentration (diluting the sample) or on the optical path.

We determined the DNA concentration of our samples by measuring the absorbance at 260 nm by using a Thermo Scientific NanoDropTM 1000 Spectrophotometer. This instrument requires reduced volumes to perform the measurement ($1-2\ \mu l$) and repeats each measurement using two different path length, in order to fall into the validity range of the Beer-Lamber law. Absorbance spectrum is measured in the range 220-350 nm thus enabling to compare absorbance at different wavelengths.

Part II

Star shaped DNA nano-stars

Chapter 4

Star-shaped DNA particles: preparation and characterization

The idea of using DNA to explore soft matter is not new: bare DNA has the tendency to self organize into ordered structures as liquid crystals [59–62], while man-designed all DNA systems and DNA covered colloids has been used to form 2D and 3D crystals pattern, as described in Chapter 2. In this work we take advantage of the knowledge about DNA controlled assembly, and especially about branched structures, to experimentally investigate the limited valence issue introduced in Chapter 1. We studied the collective behavior of DNA star-shaped nano-structures having respectively three and four arms, each arm provided with a sticky termination that enables controlled and reversible interactions. Previous investigations by Luo and coworkers have shown that when assisted by enzymatic catalysis these structures form three-dimensional hydrogels [46]. Here we operate instead in the absence of any enzyme and we perform a systematic investigation of the equilibrium phase behavior of the two systems, with the aim to determine their phase diagrams and to investigate the dependence of the phase boundaries on the valence. Overall, these DNA nano-stars, once formed, can be viewed as *supermolecules*, whose mutual interaction depend on their specific design, suggesting that the DNA approach enables to build structure that are reminiscent of the real geometry of real molecules.

4.1 Nano-stars design

4.1.1 Sequences and assembly

Star-shaped DNA supermolecules result from the assembly of 49-base long oligomers. Each structure is formed by a number of strands equal to the number of star arms (f). The sequences used to assemble the structures are as follows.

Oligomers forming $f = 3$ structures

1. 5′–CTACTATGGCGGGTGATAAAAACGGGAAGAGCATGCCCATCCACGATCG–3′
2. 5′–GGATGGGCATGCTCTTCCCGAACTCAACTGCCTGGTGATACGACGATCG–3′
3. 5′–CGTATCACCAGGCAGTTGAGAATTTATCACCCGCCATAGTAGACGATCG–3′

Oligomers forming $f = 4$ structures

1. 5′–CTACTATGGCGGGTGATAAAAACGGGAAGAGCATGCCCATCCACGATCG–3′
2. 5′–GGATGGGCATGCTCTTCCCGAACTCAACTGCCTGGTGATACGACGATCG–3′
3. 5′–CGTATCACCAGGCAGTTGAGAACATGCGAGGGTCCAATACCGACGATCG–3′
4. 5′–CGGTATTGGACCCTCGCATGAATTTATCACCCGCCATAGTAGACGATCG–3′

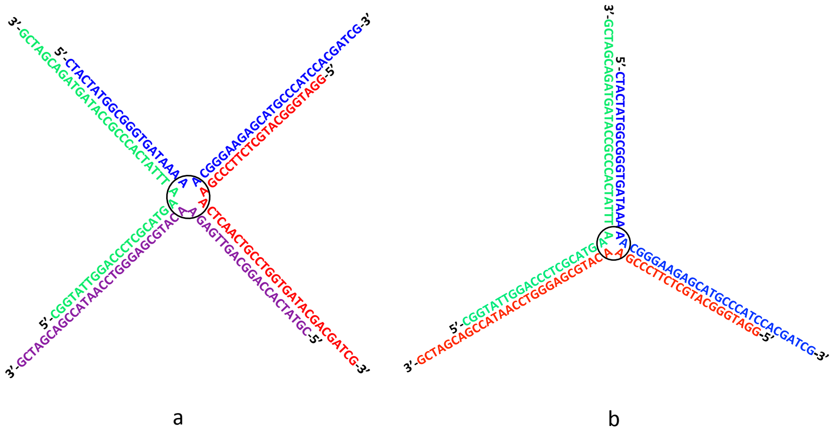

Figure 4.1: Internal structure of (a) $f = 4$ and (b) $f = 3$ particles (2D view). Each sequence is designed to bind to two other sequences with two 20 bases long segments, giving rise to the arms of the structure.

Sequences assemble as sketched in Fig. 4.1. Each strand is designed to bind to two other strands with two 20-nucleotide-long segments, leading to the formation of the arms of the structure.

Each arm terminates with a 6 bases single strand overhang having sequence $CGATCG$, which provides stickiness between arm tips (Fig.4.2) and induce interactions between structures. The overhang sequence is self-complementary and therefore all nano-star arms are equal in bond possibilities, meaning that each arm can bond to any arm of any other nano-star.

Two A bases without complementarity are placed between the arm-forming segments to release angular constraints between the arms. Such constraints arise from the crowding of paired strands at the center of the structures. With this choice arms are allowed some flexibility in their mutual angles.

For analogous reasons, another A base with no complementary partner is added before the 6-nucleotide-long overhangs. This minimizes the constraints on the mutual orientation of two bound nano-stars, since each can freely rotate around the axis connecting the centers of the two structures, and orientation of bonded nano-stars is allowed some flexibility. Despite the flexibility of the structures, electric charges on the phosphate groups will tend to keep the nano-stars arms away from each other, favoring a nearly three dimensional tetrameric shape for the $f = 4$ structures and an open flat structure for the $f = 3$ structure.

Differences in length between arms of the structures and sticky terminations is such that they have well separated melting temperatures. Arm-forming sequences are designed to self assemble at $T_{sa} \approx 65°$C, while sticky-ends start interacting at approximately $T_b \approx 30°$ C. Therefore there is a wide range of temperature where DNA structures are formed and weakly interacting with each other. Thus, upon decreasing T, the system changes from a mixture of ss at $T > T_{sa}$, to a solution of independent structures of valence f in the interval $T_b < T < T_{sa}$, to a state in which the structures are bound in clusters when $T < T_b$. Reducing the temperature, clusters grows forming a three-dimensional network [63] (Fig. 4.2). To single-out the role of the valence, we made use of identical sticky overhangs in both $f = 3$ and $f = 4$ nano-stars, so to obtain equal binding

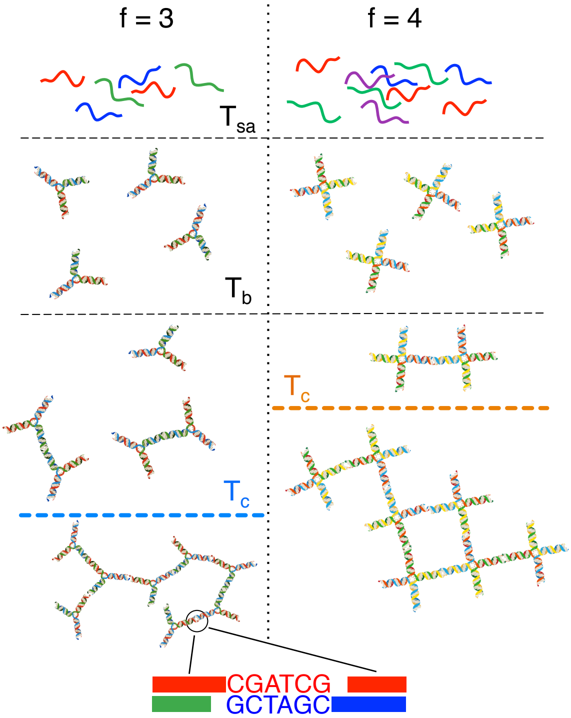

Figure 4.2: System behavior as function of temperature. Above $T_{sa} \approx 65°\mathrm{C}$, DNA is single stranded. For $T < T_{sa}$, single strands hybridize, leading to the self-assembly of stable $f = 3$ and $f = 4$ nano-stars. For $T > T_b \approx 42°\mathrm{C}$ nano-stars are independent. Below T_b, interactions between sticky overhangs (see schematic at the bottom) promote the formation of clusters that grow progressively larger as T is lowered.

free-energy in the two cases.

4.1.2 Estimates of energies and melting temperature on the bases of database values

Sequences were carefully designed so that they could self-assembly only in the star-shaped structure. Using the on-line calculator *OligoAnalizer 3.1* (eu.idtdna.com), which provides hybridization energies for couples of oligomers on the base of values reported in Ref. [24], we estimated that the energy involved in the formation of each arm is in the order of $\Delta G \approx -40\ kcal/mol$, while energies involved in other assemblies are $\Delta G \approx -9\ kcal/mol$ or even less. This gap in energies ensures that hybridization between arm forming sequences is strongly favorite with respect to other assembly possibilities.

We specifically report the calculation of the hybridization energy for the 6 bp overhangs using the Nearest Neighbor model introduced in Chapter 2. Experiments in this work were performed at a total of 48 mM NaCl, thus we used the salt correction reported by Eq. 2.5 and 2.6 to calculate the energies. By adopting the values for ΔH_Q and ΔS_Q listed in Ref. [24] we determined the enthalpy and entropy involved in the hybridization of the overhangs, providing the interaction energy between the DNA nano-stars. Calculation is as follows

$\Delta H(CGATCG) = \sum_{N-1} \Delta H_Q + \Delta H_{INIT} = (-10.6 - 8.2 - 7.2 - 8.2 - 10.6 + 0.2)$ $kcal/mol = -44.6\ kcal/mol$,

$\Delta S(CGATCG) = \sum_{N-1} \Delta S_Q + \Delta S_{INIT} + \Delta S_{SALT} = (-27.2 - 22.2 - 20.4 - 22.2 - 27.2 - 5.7 - 6.7)\ cal/molK = -132\ cal/molK$.

In the context of the collective behavior of the DNA nano-stars discussed in this work, the duplexing ΔG is a key quantity for both the equilibrium and the dynamics of the system.

The estimate of hybridization energy and enthalpy enables to determine the melting temperature T_m of the duplexes, i.e. the temperature at which half of the duplexes are unbound. Indeed, the melting temperature of the overhangs is a crucial parameter in designing the structures and in particular in determining the length of the overhangs. When dealing with self-complementary sequences, as the 6mer forming the overhangs, T_m can be expressed using Eq. 2.8 [64]

Two relevant concentrations within this work are $c = 9$ mg/ml for the $f = 4$ system and $c = 4.5$ mg/ml for the $f = 3$ system When $f = 4$ and $c = 9$ mg/ml, the evaluation of the melting temperature leads to $T_m \approx 30.5$°C. The same calculation in the case of $c = 4.5$ mg/ml and $f = 3$, brings to $T_m = 26.7$°C because of the smaller f and [c] values. At T_m a large fraction (half) of the overhangs are duplexed, i.e. a situation where DNA nano-stars are strongly interacting. Actually, nano-stars interactions start becoming relevant at a larger T. By adopting a similar approach, we can estimate the temperature T_b, defined as the temperature at which 10% of the $f = 4$ system overhangs are duplexed. We obtain $T_b \approx 42.4$°C.

4.2 Nano-stars preparation

Sequences were synthesized by Primm S.p.a. (Segrate, MI Italy) in $3'$ to $5'$ direction while covalently attached to a solid support (solid phase synthesis). Oligonucleotides were PAGE purified to insure high purity level of product (up to 95-99% of full-length product).

$f = 3$ and $f = 4$ nano-stars were formed by mixing equimolar quantities of the three and four strands respectively involved in the structures. To minimize the amount of ill formed nano-stars we took particular care to ensure that the f distinct oligomers were present in equal stoichiometric amount in all samples. To this aim, we prepared a single starting solution by mixing the f sequences in equal ratios. The large amount of DNA involved in the starting batch and its low concentration ($1\ mg/ml$) reduced the errors in volume and concentration measurements. The obtained homogeneous mother solution was then divided into several aliquots, which were then dried for subsequent use.

DNA was dissolved in NaCl electrolyte solution prepared with degased MilliQ water. Ionic strengths were chosen to yield similar ionic conditions in the samples despite the difference in the DNA concentrations, assuming that each phosphate dissociates one cation. The resulting counterions concentration is, for all the samples we investigated, approximately 50 mM NaCl. pH measurements indicate that in our working conditions, $pH \approx 7.5$, a condition in which we can safely assume that all phosphate groups in the DNA backbones have dissociated [28].

Annealing procedure

In order to enable nano-stars formation, solutions were heated to 90°C and slowly cooled to room temperature. Three annealing procedure were tested:

1. in oven, about 20min at 90°C, then cooled to room temperature in approximatively 3 hours;
2. in microscope hot stage: 5 min at 90°C, 30 min at 65°C, 30 min at 50°C, 30 min at 37°C, then cooled to room temperature;
3. in microscope hot stage: 5 min at 90°C, from 67°C to 58°C with rate 0.01° C/min (this range of temperature includes T_m for the nano-stars, section 4.3.2) then cooled to room temperature in approximately 2 hours.

Gel electrophoretic measurements (see Section 4.3.1) have shown that procedure 2 is not efficient on our system, leading to the formation of a small amount of structures. Procedure 1 and 3, instead, lead to the formation of $\approx 92-96\%$ of well formed structures.

Since procedure 1 and 3 lead to almost identical results, procedure 1 was chosen as standard, as it is easier and quicker to run.

4.3 Characterization of the system

4.3.1 Gel electrophoresis

To check for the actual assembly of the DNA oligomers into the desired structures, we performed electrophoretic runs under non-denaturing conditions in 3% agarose gel. DNA solutions were first diluted in TBE buffer to a concentration of ≈ 100 ng/ml maintaining the ionic strength to 48 mM NaCl, so to keep the amount of counterions about the same as before the dilution. We run the DNA samples in the gel at temperatures between 33°C and 35°C to minimize interactions between the sticky-ends. The temperature could not be increased further because the agarose gel melts at 40°C.

Electrophoretic analysis of the samples used for the experiments is shown in Fig. 4.3a. In the central lane (M) a double strand DNA size marker (pUC8 *Hae*III fragment lengths varying from 587 to 80 bp) was used to approximately gauge the position of the DNA structures. In lanes A and B we loaded a solution of $f = 4$ nano-stars whereas in lanes C and D we run $f = 3$ nano-stars. Lanes A and C are referred to experimental samples first prepared at $c = 9$ mg/ml and $c = 4.5$ mg/ml respectively and annealed as described in the previous section, and later diluted as described above. The profiles of the fluorescent intensity I_F for lanes A and C measured by using a Typhoon 9200 phosphor imager and the ImageQuant software (GE Healthcare) as a function of the running coordinate x are shown in Fig. 4.3 [panels (c) and (d)] for $f = 4$ and $f = 3$ respectively. Each curve has been analyzed by fitting the main peak with a Gaussian curve (dashed lines) and comparing its integral (after background subtraction) with the integrated intensity of the shoulder on its right hand side, possibly representing partially formed nano-stars, smaller and thus with a larger electrophoretic mobility in the gel. Such a shoulder has the shape of a wide peak in the case of $f = 4$ nano-stars, and thus in this case was also approximated with a second Gaussian curve (line). The shoulder in the $f = 3$ case, being instead monotonically decreasing, could not be fitted by a peak-shaped function and was thus integrated directly from the data. From this analysis we obtain that fully formed structures involve about 93% of the total DNA for both $f = 3$ and $f = 4$ nano-stars.

To obtain a reference value for the mobility of the different structures that could result from the partial hybridization of the sequences, we prepared solutions in which the

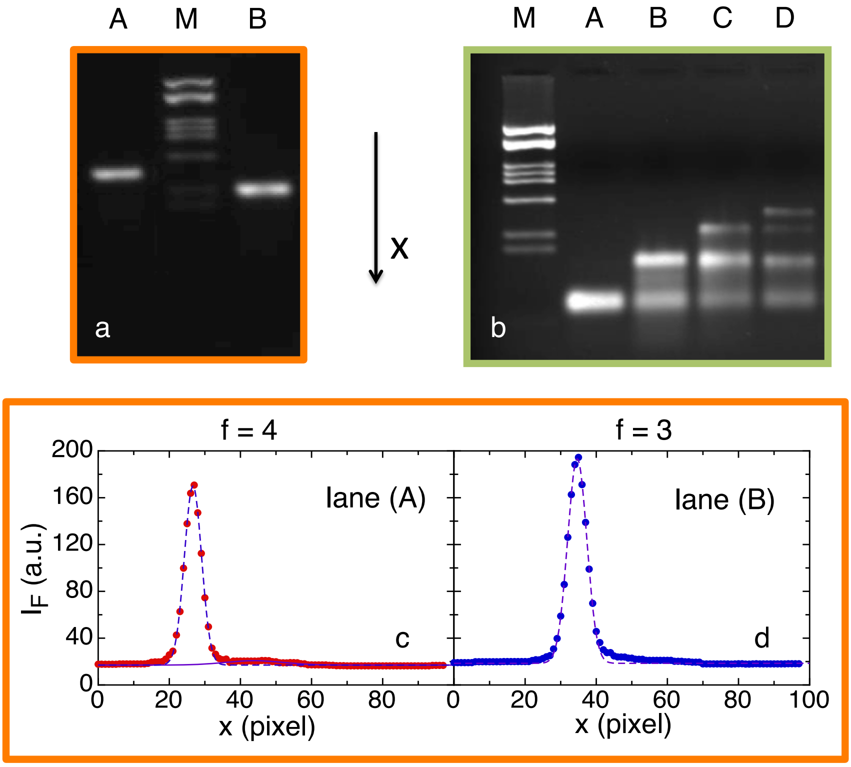

Figure 4.3: Electrophoretic measurements on 3% Agarose gel. (a): gel runs of samples with properly balanced stoichiometric ratios. Lane A $f = 4$ nano-stars at $c = 9$ mg/ml. Lane B $f = 3$ nano-stars at $c = 4.5$ mg/ml. Lane M shows the bands of reference sequences. (b): gel runs of partially formed $f = 4$ nano-stars. The solution in lane A contains only sequence 1 of the four sequences forming the structures; lane B contains sequences 1+2; lane C sequences 1+2+3; lane D sequences 1+2+3+4. (c-d): intensity profiles extracted from the four lanes of the gel in panel a as a function of the pixel position.

f sequences are progressively added. Fig. 4.3b shows such results performed with the set of sequences designed to assemble in the four arms structure. In lane A we loaded a solution containing sequence 1 only, obtaining a unique band; in lane B we run a mixture of sequences 1 and 2, obtaining two bands; in lane C we run a mixture of sequences 1, 2 and 3, obtaining three bands; in lane D we run a mixture of sequences 1, 2, 3 and 4, obtaining four bands. Since here the stoichiometric ratios are only approximately maintained and since sequences are added sequentially with no annealing, all partial combinations are found in the solution, as desired to obtain a reference system. As generally expected, the mobility of the structure is reduced as its mass and its three dimensional complexity is increased i.e. increasing the number of arms [65].

4.3.2 Melting temperature

DNA structures in our experiments were designed so that the assembly of each nano-stars would take place at a temperature significantly larger than the one at which mutual interactions occur. To ensure this gap in T and to properly define the annealing protocol, we characterized the melting process of our structures.

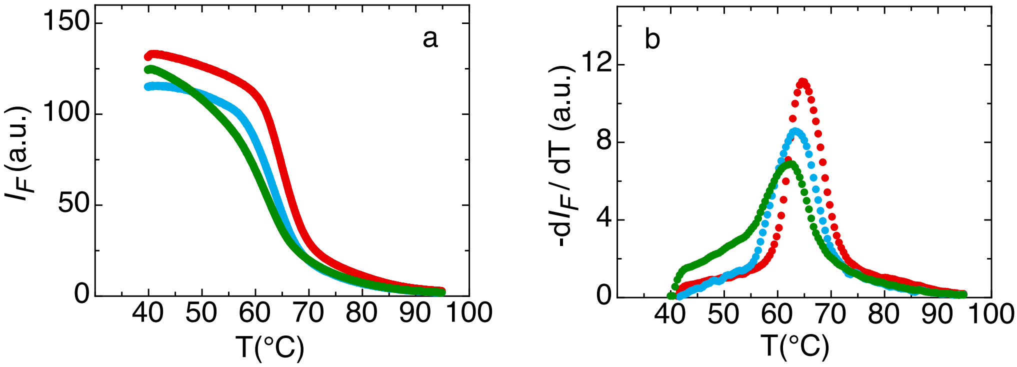

Figure 4.4: Melting curves as measured by the fluorescent emission of a fluorochrome whose emission vanish when DNA double strands unbind. Left: fluorescence emission vs. temperature for fully formed $f = 4$ nano-stars (red dots) and for partially formed $f = 4$ nano-stars, made by 2 and 3 out of the 4 building strands (green and blue dots, respectively). Right: inverse derivative of the fluorescence intensity vs. temperature.

To perform these measurements, samples were first annealed and diluted as described in the *Gel electrophoresis* section, and later mixed with the tagging fluorescent dye. The results obtained with the $f = 4$ particles are shown in Fig. 4.4 (red dots). In the left panel we plot the T dependence of the fluorescent intensity, that has the expected sigmoidal decrease as T grows. To better determine the melting temperature we also show, in the panel on the right, the derivative of I_F with respect to T. The melting temperature is indicated by the peak temperature [56]. For both the $f = 3$ (data not shown) and $f = 4$ nano-stars we find $T_m \approx 65°\mathrm{C}$.

With similar experiments we also checked the melting behavior of the partially built nano-stars that we studied by gel electrophoresis in lane b and c of Fig. 4.3a, *i.e.* samples containing respectively two and three of the set of four sequences to form the $f = 4$ nano-stars. The results are shown in Melting curves and derivatives for these samples are also shown in Fig. 4.4 (green and blue symbols). As expected, the melting temperature decreases for incomplete nano-stars.

4.3.3 Characterization by light scattering

On the bases of the considerations on the energies of interactions discussed in Section 4.1 we expect the DNA particles to be weakly interacting at high temperatures.

We investigated the size of weakly interacting structures by performing static and dynamic light scattering measurements at high temperatures ($T = 45°\mathrm{C}$) on both $f = 3$ and $f = 4$ nano-stars.

Field correlation functions for $f = 3$ structures at $c = 4.5$ mg/ml, and for $f = 4$ structures at the highest and lowest DNA concentrations we explored ($c = 3.6$ mg/ml and $c = 9$ mg/ml respectively) are compared in Fig. 4.5a. The correlation functions show a first major decay which is similar among the three samples and is well approximated by a single exponential. The resulting correlation time corresponds to a hydrodynamic radius of $r = 4.5$ nm for the $f = 3$ particles and $r = 4.7$ nm for the $f = 4$ particles. These values are in agreement with the estimated size of the nano-stars, whose arms are expected to be ≈ 8 nm long.

The second spurious decay that is also present in all of the high temperature correlation functions has unclear origin. It may be due to contamination of the sample, or straylight

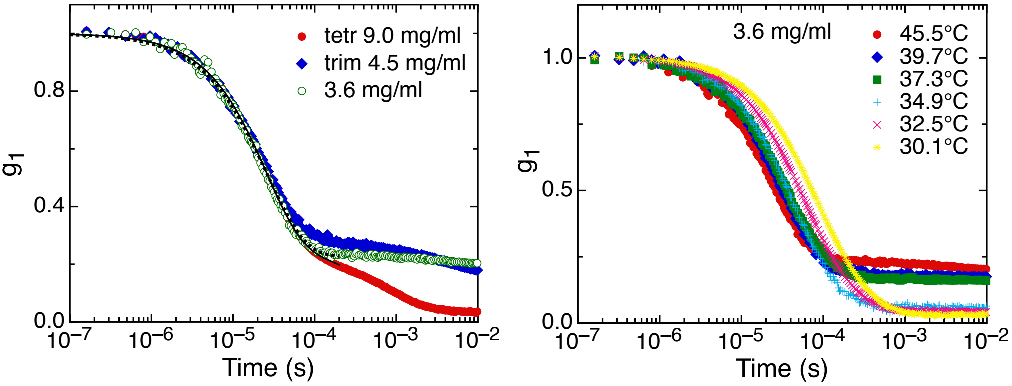

Figure 4.5: Dynamic light scattering (a) tetramers and trimers, at $\theta = 90°$, (b) high temperatures, $c = 3.6$ mg/ml at $\theta = 90°$: the second decay disappears .

reflections, or other artefacts. In any case, its amplitude progressively reduces as the temperature of the sample is lowered, till it vanishes. One possible explanation for this behavior is that the light scattered by the sample, which increases in amplitude as the temperature is decreased, progressively overwhelms the contribution of the spurious effect (Fig. 4.5b).

Accordingly, static measurements at $T = 45°$C show a q dependance of the scattering intensity that also decreases with temperature - but still remaining in the range of temperatures at which nano-stars are weakly interacting. When $T \approx 35 - 30°$C the scattering intensity does not depend on q, especially for the low concentration samples (Fig. 4.6)

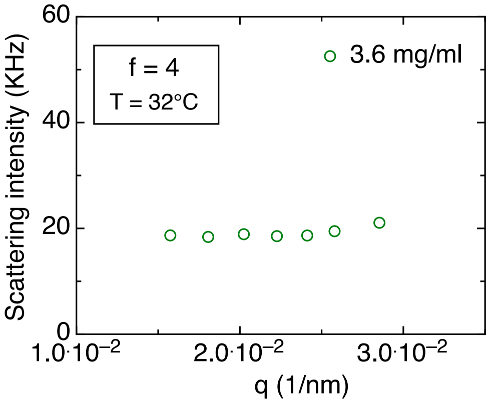

Figure 4.6: Static light scattering at high temperatures for $f = 4$ DNA nano-stars

4.3.4 Packing fraction of nano-stars and density of the network

According with recent theories and simulations $f = 3$ and $f = 4$ systems are expected to phase separate into two coexisting particles-rich and particles-poor phases. In particular, particles in the dense phase are expected to connect to each other saturating their bond possibilities and originating a network [5] . Geometrical considerations, as well as theoretical predictions [5, 66], show that $f = 3$ and $f = 4$ particles have a maximum (optimal) packing fraction $\phi = 0.18$ and $\phi = 0.30$ respectively. On the bases of these values we can estimate the DNA concentrations corresponding to the maximum packing of nano-star structures for both $f = 3$ and $f = 4$ systems. The volume fraction is expressed as

$$\phi = \frac{\pi L^3 n}{6} \tag{4.1}$$

where L is the diameter of an equivalent sphere and n the *number density*, i.e. the number of structures in a sample volume V. We consider $L = 16$ nm (twice the length of a star arm) and we assume the sticky-ends to remain aligned with their arm axes, thus the concentration we obtain has to be considered as a lower limit. The number density is $n = 135$ μM and $n = 225$ μM for $f = 3$ and $f = 4$ respectively, and the corresponding packing DNA concentrations are $c = 6.1$ mg/ml and $c = 13.6$ mg/ml.

This can be explained on the bases of simple geometric consideration, since $f = 3$ structures can only grow an "open" network, while $f = 4$ structures, having more bond possibilities, can connect in a more compact network. An example of the two networks in 2D is sketched in Fig. 4.7, but the same argument holds in 3D too.

With this notion we start this work by studying samples having concentration lower than that of the maximum packing.

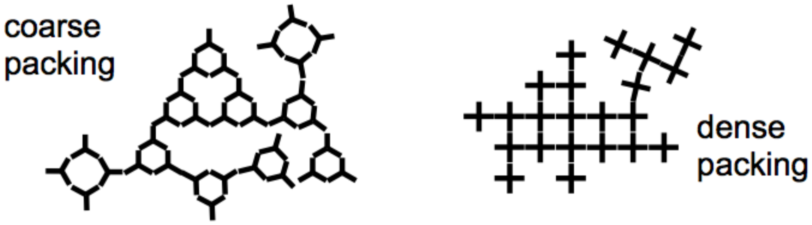

Figure 4.7: 2D networks for $f = 3$ and $f = 4$ systems

Chapter 5

Phase diagram of limited valence aggregates

DNA nano-stars with three and four arms have been introduced and characterized in the previous chapter. Arm tips are sticky and induce interactions between individual structures. For this reason, DNA nano-stars aggregates can be considered as particles having well defined valence number, $f = 3$ and $f = 4$ respectively. Interactions between particles are driven by hybridization of complementary overhangs, and thus are regulated by temperature, with interactions increasing as the temperature is lowered. Every sample we investigated, for both types of structures, showed phase separation when cooled below a critical temperature T_c. This chapter describes in detail the procedure we used to measure the phase diagrams of the limited valence nano-star particles.

5.1 Phase diagram via measurements of volume

5.1.1 Experimental procedure

On the bases of theoretical predictions [5, 66] we assumed that solutions of DNA nano-stars had a symmetric bell-shaped consolution curve. We expected the volume fraction ϕ_+ occupied by the dense phase to be related to the concentration its c_+ through the lever rule and we used Eq. 3.40 to determine the boundaries of the coexistence region.

To this aim, samples with different concentrations were cooled to the same target temperature. When phase separation takes place, we expect the volume fraction ϕ_+ to increase accordingly with the native concentration of the samples. For each sample we measured the volume fraction of the dense phase, plotted it as a function of the initial concentration, and extracted the concentrations of the coexisting phases as fit parameters of Eq. 3.40.

Sample preparation

DNA solutions of $f = 4$ structures were prepared as described in Section 4.2, at the concentrations of $c_{DNA} = 3.6$ mg/ml and $c_{DNA} = 6.0$ mg/ml. DNA samples were diluted in NaCl electrolyte solutions 37 mM and 30 mM respectively in order to maintain the ionic strength to ≈ 50 mM.

NMR cylindrical, borosilicate glass tubes (inner diameter = 2.4 mm, Hilgenberg GmbH) were cleaned flushing out the inside first with acetone and then with ethanol, to remove acetone residues. Tubes were filled with about 50 μl of sample, topped with

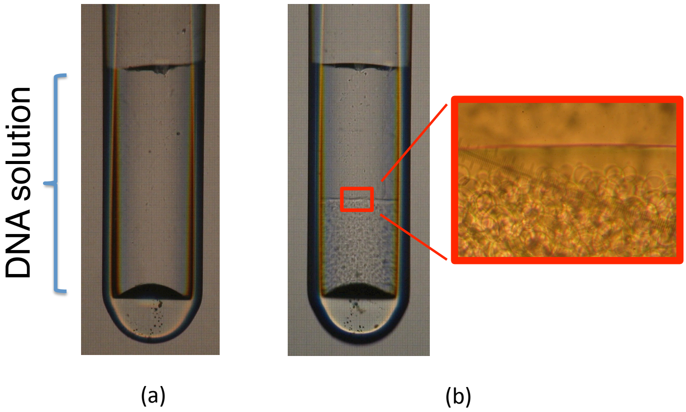

Figure 5.1: DNA sample of $f = 4$ nano-stars, $c_0 = 6.0$ mg/ml, at two temperatures. (a) At $T = 40°\mathrm{C}$ the systems is homogenous (b) At $T = 20°\mathrm{C}$ the system is separated in two coexisting phases. The sample is not in equilibrium; inset shows nuclei of diluted phase entrapped in the dense phase

about 30 μl of silicon oil to avoid evaporation and condensation on the tube walls, and flame sealed.

Thermalization and centrifugation

DNA samples were treated with the annealing procedure (≈ 20 minutes at 90°C, then cooled at room temperature in ≈ 3 hours) and then thermalized in a thermal bath with plexiglass walls. This arrangement enabled to monitor the behavior of the samples while maintaining their temperature constant. Samples were thermalized at 40°C overnight to induce disassembly of eventual aggregates of structures, then quickly cooled to a target temperature in the range $10-30°\mathrm{C}$. In between successive temperature quenches, samples were heated up to 40°C and thermalized overnight again.

$f = 4$ samples cooled at $T < 25°\mathrm{C}$ showed phase separation. Fig. 5.1 shows a typical DNA sample before and after phase separation has occurred. Fig. 5.1a shows the sample in its homogenous phase, while in Fig. 5.2b an interface that divides the two coexisting phases is clearly visible. It became evident quite soon that each sample can take a long time to equilibrate, depending on its initial concentration. Samples at concentration 3.6 mg/ml phase separate and equilibrate over a period of a couple of days, while 6.0 mg/ml samples can take more that one week to reach the new equilibrium condition. Observations with optical microscopy on non-equilibrated samples revealed that the high density phase was not homogeneous yet. It contained entrapped nuclei of low density phase, suggesting that the difference in concentration of the two phases should be quite wide (Fig. 5.1b).

To speed up the phase separation process, samples were centrifuged in controlled temperature condition for approximately 4 hours at $3000g$. Centrifugations were performed in commercial Eppendorf Centrifuge 5702 RH with swing-bucket rotor. The centrifuge, refrigerated and heatable, is certified to work between $-9°\mathrm{C}$ and $+42°\mathrm{C}$ with discrete steps of 1°C and a tolerance of $\pm 1°\mathrm{C}$ on the target temperature T_t. Test measurements I run on water samples show that in the range $(5-20)°\mathrm{C}$, i.e. the range of temperatures relevant in this experiment, tolerance on T_t is reduced to $\pm 0.5°\mathrm{C}$, but this error is still wide with respect to the precision we would like to achieve to properly determine the

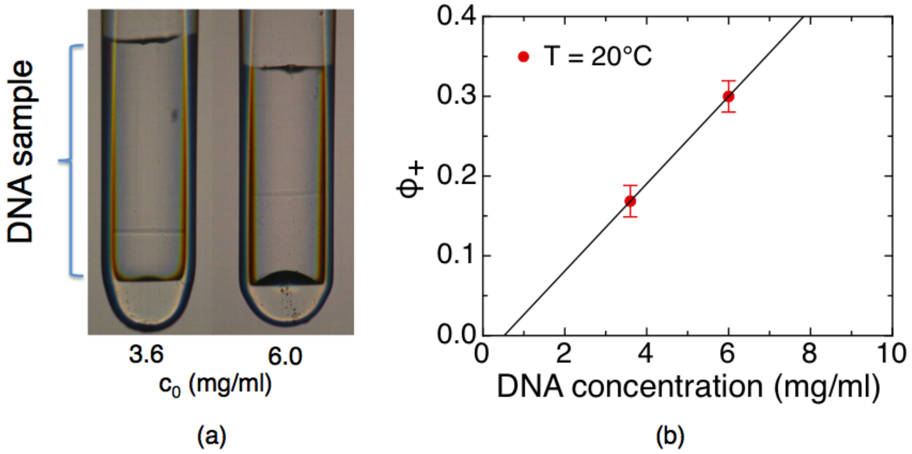

Figure 5.2: DNA solutions of valence four structures, with different initial concentrations: (a) c_0 = 3.6 mg/ml, (b) c_0 = 6.0 mg/ml. As expected, the volume occupied by the high density region is larger as c_0 is increased.

phase diagram of our system, especially at the top edge of the consolution curve.

Measure of ϕ_+

Samples having native concentrations $c_0 = 3.6$ mg/ml and $c_0 = 6.0$ mg/ml were thermalized and centrifuged together, to maintain the same thermal history. Images of the two samples at the various temperatures were projected on a screen and acquired with a commercial CCD camera (Canon PowerShot S45). In Fig. 5.2a are reported images acquired at $T = 20$°C. We notice immediately that the two samples are phase separated and, as expected, since they differ in native concentration, in the new equilibrium condition the dense phases occupy different fractions of the total volumes.

Since tubes containing the DNA solutions have constant section, the quantity ϕ_+ is obtained for each sample as ratio between the quote reached by the whole DNA sample and the quote reached by the dense phase only. A standard error of 1.5 pixels is attributed in the evaluation of the quotes of the interfaces, resulting in an error on the quantity ϕ_+. Volume fractions relative to the dense phases of the two samples have been measured for several temperatures, and for each temperature they have been plotted as a function of the native concentrations, as reported in Fig. 5.2b for $T = 20$°C. Data were fitted with Eq. 3.40 and the concentrations of the two phases extracted as fit parameters.

5.1.2 Results and discussion

Two couples of $f = 4$ nano-stars samples having concentrations $c_0 = 3.6$ mg/ml and $c_0 = 6.0$ mg/ml were prepared independently and measured using the experimental procedure described in Section 5.1.1. The phase diagrams so obtained are shown in Fig 5.3. We identify a region in the *concentration − temperature* plane where phase separation of $f = 4$ nano-stars actually occurs.

The highest temperature at which we could observe phase separation is ≈ 25°C, well below the temperature at which the structures are weakly interacting $T = 45$°C. Values of c_+ obtained from the two sets of samples are $c_+ \approx 13$ mg/ml and $c_+ \approx 18$ mg/ml.

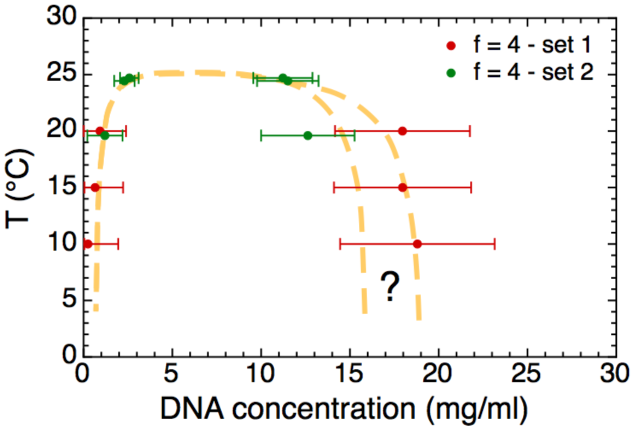

Figure 5.3: Phase diagram of $f = 4$ DNA nano-stars

Despite the c_+ values experimentally determined differ among each other, they both are of the same order of the c_+ value expected on the bases of geometrical considerations on the ideal packing fraction of $f = 4$ structures.

In the explored range, the consolution curve appears to be quite straight on the side but the error bar on every point is wide. Error bars have been determined using error propagation, on the bases of the errors associate to the volumes used to determine ϕ_+. Evaluation of the volume occupied by each phase is made difficult by two effects: (i) tubes are not flat on the bottom, and (ii) interfaces between DNA sample and sealing oil, and between the two coexisting DNA phases, are not flat due to the continuous centrifugations (one for each temperature) that each sample sustain. During the centrifugation process, indeed, tubes may remain slightly tilted with respect to the spinning plane.

In addiction, despite the fact that samples were identically prepared, the two sets of samples lead to different values for the dense phase. This is probably due to experimental errors on the native concentrations c_0, which are larger for high concentrations because the high viscosity of the solutions makes them difficult to handle.

Even the highest temperature at which phase separation takes place may vary for different sets of samples. This may be due to slight differences in the ionic strength of independent sets of sample.

Even worst, the same two samples (the same two tubes) may show a different transition temperature after they have been cycled two or three times. This may be due to a non efficient method to properly melt the dense phase and restore the native concentration c_0. In this scenario, every time we run a quench on the sample, its c_0 could be lower than the previous time, and also the ionic strength in the isotropic phase could be different.

In conclusion, measurements of the volumes occupied by the dense phases lead to the identification of a coexisting region for solution of $f = 4$ structures and to the determination of a range of c_+ values. On this specific system (DNA nano-aggregates), though, the method is strongly affected by experimental errors (producing reliable concentrations, reproducing the exact ionic strength, properly melt the dense phase, thermalization of the thermal bath according to the temperature of the centrifuge) and it is also quite time consuming due to the centrifugations and the thermal protocol. A more reliable way to obtain the values of c_+ and c_- would be to measure them with a direct measurement of the concentration. This approach will be discussed of the next section.

5.2 Phase diagram via measurements of concentration

5.2.1 Experimental procedure

Phase diagrams of $f = 3$ and $f = 4$ nano-stars have been determined via direct measurements of the DNA concentration in the dense and diluted phases of DNA solutions. To this aim, we cooled identically prepared capillaries containing the nano-star solution at the target temperatures, we extracted the DNA and measured its concentration via UV absorption.

Sample preparation

Mother solutions of $f = 3$ and $f = 4$ nano-stars were prepared as described in Chapter 4, at concentrations $c_0 = 4.5$ mg/ml and $c_0 = 9$ mg/ml respectively. DNA was diluted in NaCl electrolyte solutions 35 mM and 27 mM respectively to maintain the counterion concentration ≈ 50 mM. Glass microcapillary pipettes (Kimble Glass Inc. volume $20\mu l \pm 0.5\%$) were filled with 7-8 μl of solution and flame sealed at both the extremities. About 5-6 capillaries were filled with the same mother solution, so that a stock of identically prepared samples, with identical concentration and identical ionic strength, was available for each type of particles.

Thermalization and centrifugation

Samples were treated with the annealing procedure and then stored at 37°C to prevent clustering of structures. Each sample was cooled to a different target temperature and centrifuged for about 4 hours at $3000g$ at controlled temperature to speed up the phase separation process (see Section 5.1.1). This approach has multiple advantages: (i) each sample is used for one measurement only, so the critical step of melting the dense phase after temperature quenches is avoided (ii) experimental errors on the native concentration don't affect the determination of the concentrations of the coexisting phases, as these will be determined by UV absorbance (iii) it is time saving, in one day it is possible to acquire concentrations relative to two temperatures. (iv) in principle a set of identical samples allows to repeat measurements at potentially problematic temperatures, as those close to T_c. Fig. 5.4 shows a capillary containing $f = 4$ DNA particles fluorescently marked with

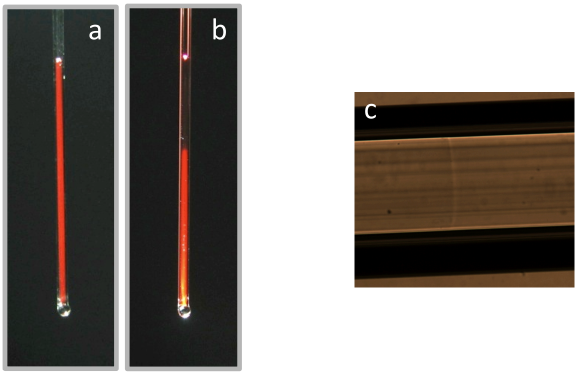

Figure 5.4: Capillary filled with $f = 4$ DNA structures, tagged with Ethidium Bromide, centrifuged at (a) $T > T_c$ and (b) $T < T_c$; DNA particles are confined in the dense phase. (c) Interface between coexisting phases in a capillary filled with $f = 4$ DNA particles.

a small amount of Ethidium Bromide in order to better visualize phase separation into the capillary. Images of the sample were acquired after centrifugation at two different T: $T > T_c$ (Fig. 5.4a) and $T \leq T_c$ (Fig. 5.4b). Clearly in Fig. 5.4b after centrifugation at $T \leq T_c$ the system is macroscopically separated into two coexisting phases.

Measure of concentration

After centrifugation, each capillary was cut in sections, two in the dense phase, one in the dilute phase. Sections from the dense phase were inspected by optical microscopy to evaluate the volume of solution they contained. The DNA contained in each section was extracted either by sucking the solution with a pipette or by plunging the section in about 80 μm electrolytic solution. Dilution of the DNA samples in electrolytic solution instead than in pure water is fundamental to keep constant the ionic strength of the solution, and to preserve nano-stars from melting. In other words, in this way we ensure DNA structures to remain assembled and stable even after the dilution.

In solutions of $f = 4$ aggregates, the difference in density between the two coexisting phases is large enough to enable seeing the meniscus by naked eyes (see Fig. 5.4c). In this case sorting sections with respect to phases was straightforward. In solutions of $f = 3$ structures, instead, no meniscus is visible by naked eye or with a microscope. We hence created a capillary doped with Ethidium Bromide (about one fluorophore per DNA structure) to enable visualization of the meniscus, similar to the one shown in Fig. 5.4 for tetramers, and used it to guide the cutting process. In this case we considered only sections far enough from the meniscus.

The DNA concentration is then determined from absorbance at 260 nm by using a Thermo Scientific NanoDropTM 1000 Spectrophotometer. Values of 260/280 and 260/230 ratios attested that DNA samples were not contaminated from proteins or solvents.

5.2.2 Results and discussion

Phase diagram for $f = 3$ and $f = 4$ structures obtained from absorbance measurements is shown in Fig. 5.5. Data are obtained as an average between several measurements, and error bars are standard deviations on the average values. Both phase diagrams are in the form of a gas-liquid consolution curve. The range of DNA concentrations where separation takes place is rather limited and actually significantly decreases on going from $f = 4$ to $f = 3$. DNA concentration in the dense phase is $c_+ = 8.9 \pm 0.4$ mg/ml and $c_+ = 17.3 \pm 0.7$ mg/ml for the $f = 3$ and $f = 4$ system respectively, in agreement with geometrical considerations discussed in section 4.3.4 (we determined the lower values for the dense phases of $f = 3$ and $f = 4$ nano-stars to be $c = 6.1$ mg/ml and $c = 13.6$ mg/ml respectively). Dilute phases have instead more DNA structures than what expected. According to theoretical predictions, the concentration of the diluted phase well below the critical temperature should approach zero [5], while it contains a significant amount of DNA nano-stars, at least for the $f = 4$ system. We measured $c_- = 0.5$ mg/ml and $c_- = 0.9$ mg/ml for the $f = 3$ and $f = 4$ system respectively.

In order to check the nature of the DNA structures contained in the dilute phases (well-formed DNA nano-stars, or other irregular structures) we run electrophoresis measurements on DNA solutions from the dilute phases. Data are shown in Fig.5.6 (to be compared with data for the homogeneous sample shown in Fig.4.3).

Each curve has been analyzed by fitting the main peak with a Gaussian curve (dashed lines) and comparing its integral (after background subtraction) with the integrated intensity of the shoulder on its right hand side, possibly representing partially formed

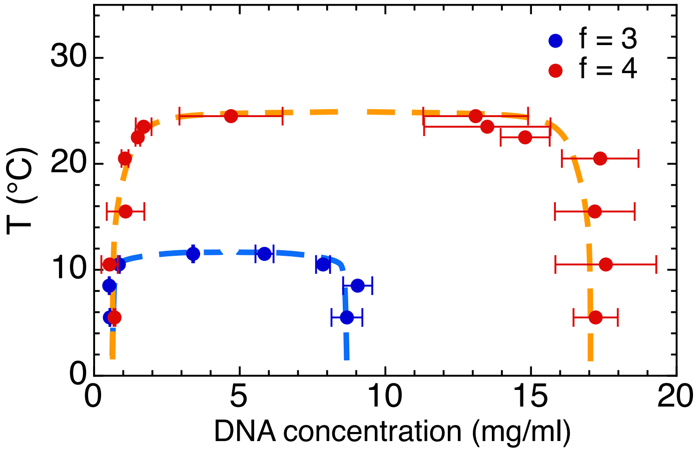

Figure 5.5: Phase diagram of $f = 3$ and $f = 4$ DNA nano-stars (blue dots and red dots respectively) determined by of UV absorbance measurements.

nano-stars, smaller and thus with a larger electrophoretic mobility in the gel. The diluted phase of the f = 4 nano-stars appears to contain a large amount of ill-formed DNA structures involving about one third of the total DNA. This finding suggests that, upon phase separating, the system segregates in the dilute phase the largest part of misshaped structures. This is reasonable since they are typically formed by two or three strands, as indicated by their larger electrophoretic mobility, and are thus less strongly interacting with the network and more prone to evaporate out of it. The profile obtained from the diluted phase of $f = 3$ (Fig.5.6c) is instead almost identical to the one obtained for the homogeneous sample (see Fig.4.3d), meaning that the dilute phase of the $f = 3$ system is almost entirely composed of well-formed structures. The difference in population of ill-formed nano-stars can thus explain the higher DNA concentration that we measured in the dilute phase of the $f = 4$ system with respect to the dilute phase of the $f = 3$ system.

The critical temperature T_c also decreases with decreasing f, as expected on the basis of the reduced number of bonds, and thus of inter-particle interaction free energy [5]. The highest T at which we observed phase separation are $T_c = 11.5°\text{C}$ and $T_c = 24.5°\text{C}$ for the $f = 3$ and $f = 4$ systems respectively.

If the interaction strength between DNA nano-stars were independent from temperature, we would expect the difference in binding energy of the two structures at given T to be given by the ratio between their valence number, a value of the order of 3/4. Thus we would expect a difference in T_c of the same order, about 25%. Instead we observe a difference in T_c that is much smaller, being of the order of $\approx 5\%$. This behavior is easily understood on the basis of the large entropic component in the binding free energy between nano-stars, which produces a large free energy variation over a narrow T range.

To better explore the effect of the T dependence of the interaction energy, it is interesting to compare the mean binding energy of DNA nano-stars in the two systems at their critical temperature.

To determine these energy values we make use of the critical temperatures obtained from the light scattering measurements (that will be discussed in Chapter 6) since LS data enabled to a more reliable determination of T_c. According to LS data the critical temperatures are $T_c = 11.6 \pm 0.5°\text{C}$ and $T_c = 25.5 \pm 0.5°\text{C}$ for the $f = 3$ and $f = 4$

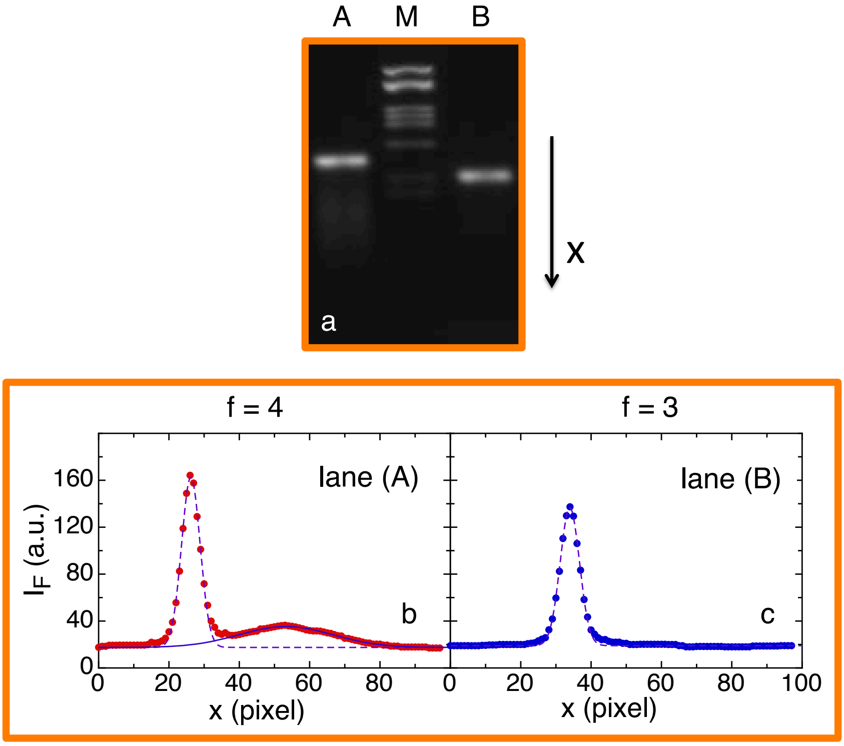

Figure 5.6: (a) Electrophoretic measurements on 3% Agarose gel. Lanes A and B contain solutions from the dilute phase of $f = 4$ and $f = 3$ structures respectively. Lane M shows the bands of reference sequences. (b-c) intensity profiles extracted from the four lanes of the gel in panel a as a function of the pixel position.

.

systems respectively. Using these values we determine $\Delta G(T = 11.6°\text{C}) \approx -7.0 \pm 0.1$ kcal/mol and $\Delta G(T = 25.5°\text{C}) \approx -5.2 \pm 0.1$ kcal/mol. These values indicate that at the two critical temperatures, the energy for fully bond DNA nano-stars is equal:

3 $\Delta G(T = 11.6°\text{C}) \approx 4\ \Delta G(T = 25.5°\text{C}) \approx$ -21 kcal/mol.

This estimate can be made more accurate by including the observation, consistently found in computer simulation of low-valency systems, that the number of bonds at the critical point is actually less than f, being 2.1 for $f = 3$ and 2.6 for $f = 4$ systems [67]. The total bond energy per particle is thus 2.1 $\Delta G(T = 11.6°\text{C})$ for $f = 3$ nano-stars and 2.6 $\Delta G(T = 25.5°\text{C})$ for f = 4 nano-stars. These two values are both ≈ -14 kcal/mol, corresponding to about $23 k_B T$ per nano-star. This simple quantitative analysis enlightens that the difference in critical temperature between the $f = 3$ and $f = 4$ systems is straightforwardly related to valence: the mean binding energy per star at the critical point is the same in the two systems. This analysis shows once more the effectiveness of DNA, whose interaction strength so markedly changes with T, as a tool to investigate statistical physics. It also offers a simple tool to predict the critical point of more complex DNA-based structures.

CHAPTER 6

Static and dynamic behavior of $f = 3$ and $f = 4$ DNA nano-stars: light scattering measurements

6.1 Critical behavior along the critical isochore

The phase diagrams discussed in the previous chapter are in the form of a gas-liquid consolution curve, necessarily terminating, at the high-T end, into a critical point. To characterize the critical behavior of the DNA nano-stars we investigated amplitude and dynamics of the pre-transitional concentration fluctuations by preparing samples at the critical concentrations ($c_c = 4.5$ mg/ml and $c_c = 9$ mg/ml for the $f = 3$ and $f = 4$ systems respectively) and lowering T to approach T_c. Measurements were done via static and dynamic light scattering, for different angles covering the wave-vector range $8.2\ \mu m^{-1} < q < 30.5\ \mu m^{-1}$. This experimental approach takes advantage of the large refractive index of DNA, enabling an effective detection of concentration fluctuations.

6.1.1 Osmotic compressibility and correlation length

According to the theory of critical phenomena, the scattered intensity $I(q)$, for small q, is properly described at all wave vectors by a Lorentzian shape (in addition to a small non-critical background component I_{nc})

$$I(q) = \frac{I_L(0)}{1 + q^2\xi^2} + I_{nc} \tag{6.1}$$

which expresses the dependence of the susceptibility (see section 1.1.2) on q and T in the critical region. In the equation, $I_L(0)$ diverges as $I_L(0) = I_0(T/T_c - 1)^{-\gamma}$, while ξ is the correlation length, diverging as $\xi = \xi_0(T/T_c - 1)^{-\nu}$. I_0 and ξ_0 provide the reference values of the critical scattering intensity and of the thermal correlation length far from the critical point. I_{nc} accounts for the (small) non-critical component of the scattered intensity. The appropriate Ising exponents are $\gamma = 1.237$ and $\nu = 0.630$ [68].

We have measured the intensity scattered by the solutions of $f = 3$ and $f = 4$ nano-stars, both prepared at the critical concentration, at various temperatures and at various scattering angles, ranging from 30° to 152°.

Fig. 6.1 shows the T dependence of the scattered intensity I measured upon cooling dispersions of $f = 3$ and $f = 4$ nano-stars for the entire set of angles. The simultaneous best fit of all the different T and all the different q values of the scattered intensity provides robust estimates for the four fit parameters T_c, ξ_0, I_0, I_{nc}. The fit is also shown in Fig. 6.1 (lines). The resulting values for the critical temperatures (marked by a vertical line in the figure) are $T_c = 11.6 \pm 0.5$°C and $T_c = 25.5 \pm 0.5$°C for $f = 3$ and $f = 4$,

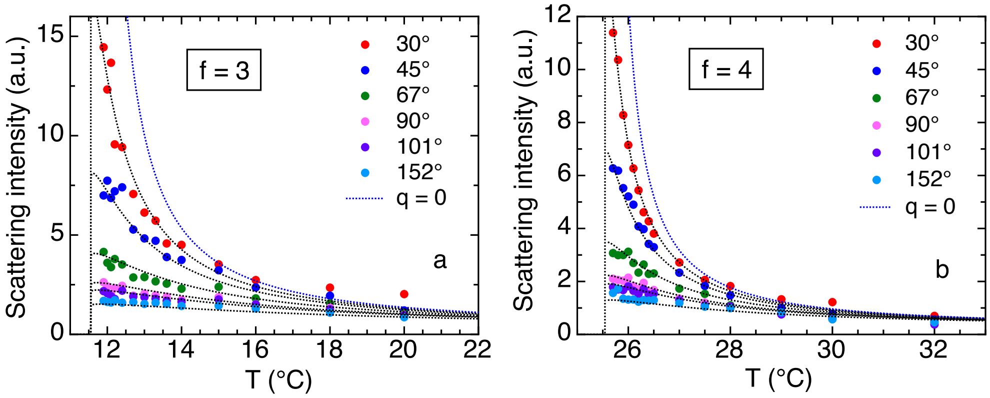

Figure 6.1: Scattering intensity by solutions of (a) $f = 3$ and (b) $f = 4$ nano-stars prepared at the critical concentration. Lines represent the best fit obtained by fitting simultaneously the whole set of data of each system by Eq. 6.1. Black vertical lines mark the critical temperatures. The blue lines represent the expected power law behavior at $q = 0$. The scattering angles, and the corresponding scattering vectors explored in this experiments are: 30° (q = 8.15 μm^{-1}), 45° (q = 12.1 μm^{-1}), 68° (q = 17.6 μm^{-1}), 90° (q = 22.3 μm^{-1}), 101° (q = 24.3 μm^{-1}), 152° (q = 30.6 μm^{-1}).

respectively. The best values for ξ_0 are $\xi_0 = 1.9$ nm and $\xi_0 = 3.2$ nm for $f = 3$ and $f = 4$, respectively. These values are in the range of the hydrodynamic radius of the nano-star ($\approx$ 4.5 nm and 4.7 nm for $f = 3$ and $f = 4$ structures) and reflect the different critical density of the two systems, smaller in the case of $f = 3$. Accordingly, the correlation length at the closest distance from the critical point that we explored in this study is $\xi \approx 240$ nm in the case of $f = 3$ nano-stars (for $T - T_c = 0.3$°C) and $\xi \approx 220$ nm in the case of $f = 4$ nano-stars (for $T - T_c = 0.15$°C). At these temperatures, the product $\xi^2 q^2$ becomes of the order of one even for the measurements taken at the smallest scattering vector, indicating that in this limit the proportionality between the measured scattering intensity and the power-law divergence of the osmotic compressibility (strictly valid only for $q \to 0$) becomes unobservable. Given the sizes of ξ obtained close to the transition, in order to satisfy the condition $\xi^2 q^2 \ll 1$, and thus approach the power-law divergence, the scattering angle should be reduced to $\theta \approx 5°$ in both the $f = 3$ and $f = 4$ systems. The expected power law behavior at these temperatures was obtained imposing $q = 0$ in the lorentzian fit, and it is plotted in Fig. 6.1 (blue lines).

6.1.2 Non-conventional critical dynamics

We investigated the dynamics of DNA nano-stars in solutions by measuring the time autocorrelation function of the scattered intensity at the same angles and temperatures reported in Fig. 6.1 for the equilibrium measurements.

According to the theory of critical phenomena, we would expect an exponential decay of the correlation functions and a power-law divergence of the characteristic time on approaching the critical point, the so-called critical slowing down [69]. We will see in the following that this is not the case of our system.

A family of field correlation functions $g_1(\tau)$ - extracted fromintensity correlation functions measured at $\theta = 90°$- is shown in Fig. 6.2a for the $f = 4$ structures. As discussed in section 2.3.3, at the highest T explored ($T = 45$°C) the correlation function is a simple

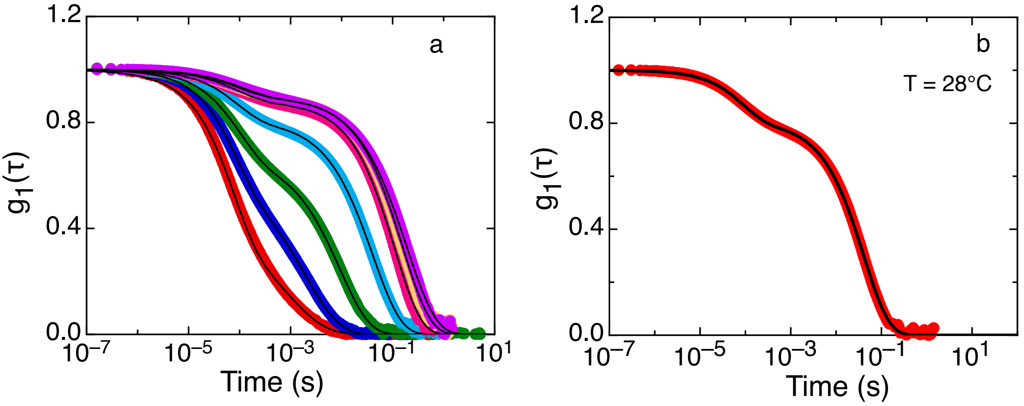

Figure 6.2: (a) Field correlation functions $g_1(\tau)$ measured in the $f = 4$ system for $T = 35$, 32, 30, 28, 26.5, 26, 25.6 °C (full symbols). Data are fitted to a sum of two stretched exponentials (lines). (b) Typical two-step correlation function (red dots) for $f = 4$ nano-stars at $c = 9\ mg/ml$. The function is fitted with Eq.6.2

exponential, confirming the existence of a range in which the nano-stars are formed and their mutual interactions are weak. Upon lowering the temperature of the system, in the correlation functions grows a second, distinct, slower decay with the clear insurgence of a plateau whose height (the so-called non-ergodicity factor in glass physics [8]) increases on cooling. This behavior reflects the insurgence of attractive interactions between DNA nano-stars, interactions that become progressively more important as the temperature is lowered, and lead to the formation of transient clusters.

We analyzed this double feature of $g_1(\tau)$ by fitting the correlation functions to the sum of two stretched exponentials

$$g_1(\tau) = A_F \cdot exp\left[-\left(\frac{\tau}{\tau_F}\right)^{\alpha_F}\right] + A_S \cdot exp\left[-\left(\frac{\tau}{\tau_S}\right)^{\alpha_S}\right] \tag{6.2}$$

where A_F, τ_F and α_F are the amplitude, characteristic time and stretching exponent for the fast component. Analogous definitions hold for the slow component.

Fig. 6.2b shows an example of correlation function (red dots) and double stretched exponential fit (line).

Characteristic times of the *fast* and *slow* component, τ_f and τ_s respectively, are reported in Fig. 6.17 as a function of T. The temperature dependence of the two decays is very different. The faster one (τ_f) changes only very mildly while the slower one (τ_s) slows down by more than three orders of magnitude in an Arrhenius fashion, without any noticeable divergence as T_c is approached. Quite remarkably, we observe no critical slowing down for any of the characteristic times in both the $f = 3$ and $f = 4$ systems. The nature of the two decay times will be discussed in detail in the next section. Here we give just few considerations. The Arrhenius behavior of τ_s describes an activated dynamics. The only process that involves such a dynamics, within out system, is the lifetime of the DNA duplexes. Since the nano-stars structures are stable in this range of temperatures, we associate τ_s with the lifetime of the duplexes formed by the DNA overhangs of interacting nano-stars. Whenever DNA nano-stars disconnect from the growing clusters, they are free to diffuse within the volume of the system, as well as nano-stars that are not part of any cluster yet. Thus we associate τ_s to the kinetic change in DNA concentration fluctuations due to the detachment of single DNA nanostars and their repositioning in

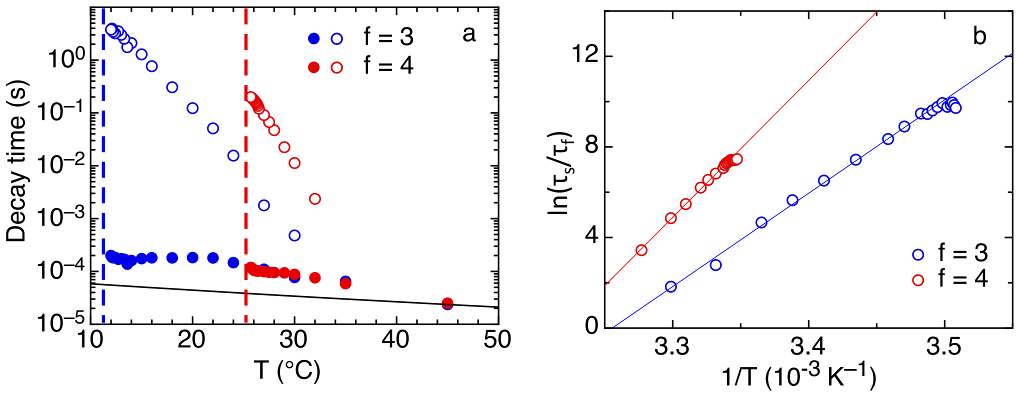

Figure 6.3: (a) Decay times for $g_1(\tau)$. At high T both systems exhibit a single decay, At lower T a second, slower, decay arises (open symbols). The black line shows the expected T dependence of the diffusive τ for independent nano-stars. (b) $ln(\tau_s/\tau_f)$ plotted as function of $1/T$ and fitted by an Arrhenius law.

different locations of the network, and the *fast* time τ_f with the fluctuations in DNA concentration that are due to their free diffusion.

Upon lowering T, the amplitude A_s increases up to ≈ 0.9, so that A_f is reduced to ≈ 0.1 (see Fig. 6.4a). The ratio between decays amplitudes reflects the relative importance of the decorrelating processes that they represent. In this DNA nano-star system the prevailing process is that associate with the *slow* decay.

In parallel, as T is lowered, the exponent of the fast component decreases from ≈ 1 to a value close to 0.75 at the critical point (see Fig. 6.4b). At the same time, α_S grows from 0.5 - the value obtained at the highest T where it can be distinguished from the fast decay - to values around 0.8. We consider the behavior of the stretching exponent of the *fast* decay as a sign of growing polydispersity in the isotropic phase, caused by growing clusters of DNA nano-stars.

It is also interesting to investigate the behavior of the scattering intensities associated to the two decays, obtained multiplying the total scattering intensity by the amplitudes of the two decays. In Fig. 6.5 we plot data relative to the scattering intensity measured at $\theta = 30°$, which is the closest angle to critical divergence. We find that the two components of diffused intensity have opposite trends: the intensity associated to the fast decay decreases as T_c is approached, while the contrary is true for the slow component. This is an interesting finding since it indicates that in the whole interval where the critical divergence of the scattered intensity is found, the intensity is basically all associated to the slow component. This is also confirmed by comparing the amplitude of the slow component with the line in Fig. 6.5, which represents the total scattering intensity (it is the same line fitting the $\theta = 30°$ data in Fig. 6.1).

In Fig. 6.6 we report the q behavior of τ_f and τ_s for the $f = 4$ system. Both the fast and slow decay times are found, within experimental uncertainty, to be proportional to q^{-2}, as expected for diffusive kinetics and for critical fluctuations.

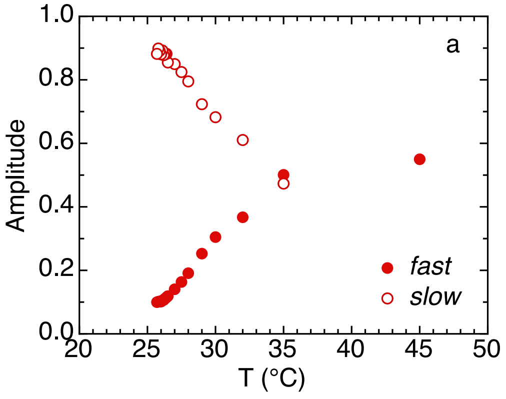

Figure 6.4: T dependence of the (a) amplitude and (b) stretching exponent for the *fast* and for the *slow* components.

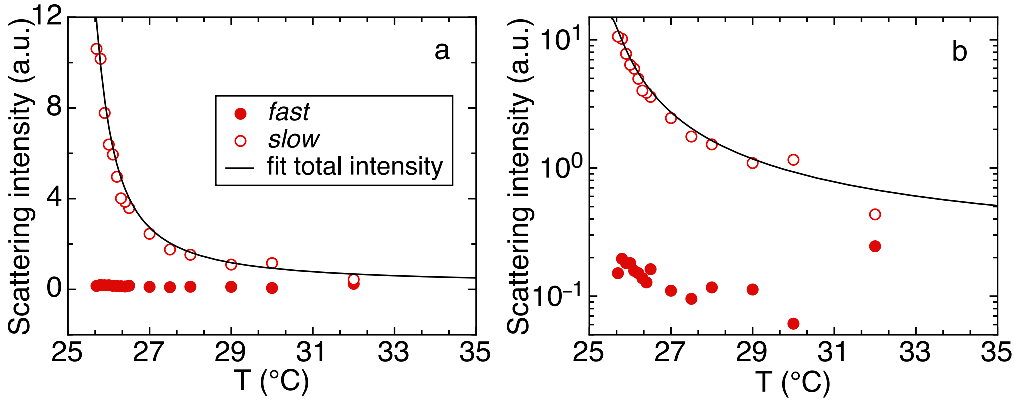

Figure 6.5: Scattering intensity associated to the *fast* and *slow* contributions of $g_1(\tau)$. (a) lin-lin; (b) lin-log representation of the same data. The line is the fit to the total scattering intensity already reported in Fig. 6.1 for $\theta = 30°$. The log scale in (b) enables visualization of the scattering intensity associated to the fast component.

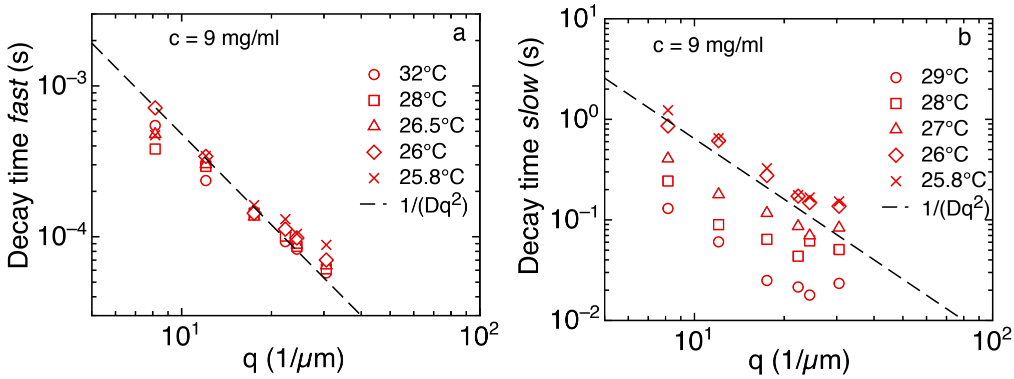

Figure 6.6: q dependence of the characteristic times for the (a) *fast* and (b) *slow* relaxation processes.

6.1.3 Critical slowing down and activated dynamics

The analysis of the dynamic light scattering data presented in the previous section indicates that the critical fluctuations giving rise to the scattering divergence decay through the slow process. Since the interactions of DNA structures involve short-ranged on/off bonds, it is possible to describe the formation and dissipation of concentration fluctuations by distinguishing two families of contributing processes: those that involve the breaking of inter-structures bonds and those that do not. The latter include the diffusion of unbound structures (or small aggregates of structures), accounting for the relaxation of the intensity correlation function at high T. They also include bond-preserving oscillations of the network, expected to contribute to the dynamics as the network grows [70]. We could however not detect convincing clues of their presence yet. Indeed, as T is decreased, network oscillations should increase in amplitude together with the scattering from the network, but they should not show an Arrhenius growth as the slow component do. For these reasons, network oscillations should give rise to kinetic contributions having a behaviour different from either the observed fast and slow components. Data thus suggest that bond-maintaining network oscillations might be of small relevance and buried under the other phenomena more easily detectable.

Overall, bond-preserving mechanisms provide a partial decorrelation, limited by the constraints imposed by the topology of the network, since only by breaking bonds the system can become fully ergodic. The local disruption of network bonds enables its readjustment into different patterns. This can take place either through nano-stars "evaporating" away from the network and reconnecting elsewhere or through the rearrangements of network portions made flexible by the opening of bonds. The kinetics of this process is intrinsically limited by the rate of unbinding events and thus necessarily slower than the free diffusion of the structures, being the lifetime of short paired oligomers easily spanning into the ms regime [71].

The characteristic time of the slow component of the dynamics grows as an Arrhenius-Eyring activated process $\tau = \tau_0 exp(-\Delta G/k_B T)$, where τ_0 is the high T characteristic time. By fitting the slope of $\ln(\tau)$ vs $1/T$ it is possible to evaluate the enthalpic part of ΔG. Specifically, we find $\Delta H = 82$ kcal/mol and $\Delta H = 120$ kcal/mol for the $f = 3$ to $f = 4$ nano-stars, respectively. These values correspond to about 1.8 and 2.7 times the enthalpic component expected for the binding of the sticky overhangs (see section 4.1.2 (characterization of the system)).

To extract from the Arrhenius-Eyring behaviour the entropic component of nano-star binding it is necessary to independently know the value of τ_0. We assume $\tau_0 = \tau_F$, in line with the notion that the diffusion processes following bond breaking are the same that produce the fast relaxation: free cluster diffusion and constrained diffusion of network fragments. Accordingly, $\tau = \tau_F exp(-\Delta G/k_B T)$. Under this assumption, from the data we obtain $\Delta S = 266$ cal/(mol K) and $\Delta S = 386$ cal/(mol K), for the $f = 3$ and $f = 4$ systems, respectively. These values correspond to respectively about two and three times the entropic component expected for the binding of the sticky overhangs (see section 4.1.2). Thus, the analysis of the activated slowing down consistently indicates that to achieve ergodicity the system undergoes readjustments that involve the breaking of a number of bonds lower than f. This notion makes good physical sense since breaking events take place more probably where the network is weakest, and less probably involve the disconnection of fully bonded supermolecules.

A striking result is that the slow decay does not show the power-law divergence expected for the critical slowing down. It is interesting to evaluate what would be the T dependence of the correlation time expected for an "ordinary" phase transition on the basis of the critical slowing down for the 3D Ising model with conserved order parameter. For $q \to 0$, $\tau_T = \tau_{T,0}\ \xi^z$, where $\tau_{T,0}$ is a coefficient and $z = 2$ is the critical exponent for the dynamics scaling of the 3D Ising system [72].

We display in Fig. 6.7 the predicted $\tau(T)$ with the $\tau_{T,0}$ coefficient chosen so to match the measured τ at high T, where the dynamics is purely diffusive. Quite evidently, the expected slowing down is, in the explored T range, much less significant than the one observed. Only very close to T_c the predicted τ_T would become slower than the measured τ. This simple estimate suggests that in the whole T range here explored, the critical slowing down is buried under the steep Arrhenius-Eyring dependence describing the growing stickiness of the DNA nano-stars. We can not exclude also the possibility that the finite q of our measurements can also contribute to mask the power-law divergence of the characteristic time, similarly to what has been observed for the scattered intensity.

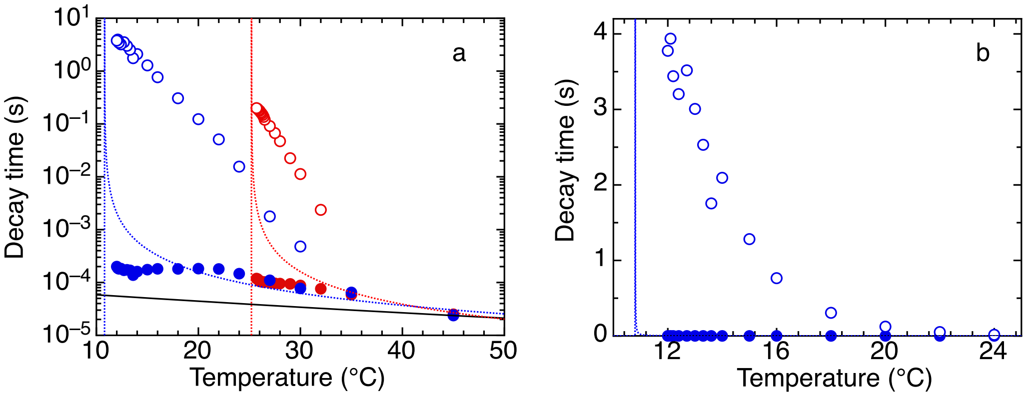

Figure 6.7: (a): Comparison between data and expected critical slowing down for both the $f = 3$ and $f = 4$ systems. (b): Linear plot of the same data, limited to the region of interest for the $f = 3$ structures.

On this basis we expect this same "anomalous" kinetics to be present even in much simpler systems every time the bond energy has such a strong T dependence. Even a simple random walker on a cubic lattice in which each site of the lattice has an escape barrier whose energy $\varepsilon(T)$ depends on T would have a diffusion coefficient $D = \ell^2/(6\tau_0)$ $exp(-\varepsilon(T)/k_B T)$, dominated by the activated component. Thus, a lattice gas built on this same lattice, would have a consolution curve with a critical point, whose kinetics, except for a very narrow range around T_c, would be dominated by the activated escapes from the lattice sites. Quite clearly, if the activated escape is transferred from the lattice sites to the interaction of nearest neighbors one would have a toy model of the situation we are here describing, maybe worth for a future in-depth analysis of the activated critical dynamics emerging from our experiments. This model would intrinsically combine critical slowing down and activated dynamics as the phase transition is approached. On the basis of such a model, we would expect the *slow* decorrelation process to be modulated on the critical slowing down, and thus the T dependence of τ_s to be described by the product of the two. This is not what we observe. As already pointed out, we observe no sign of critical slowing down in our data. One possible reason why such a multiplicative dynamics does not appear in our data is that the $q\xi$ value is not small enough to enable its detection. It is possible that in the q range we could explore, the critical slowing down is modified with respect to its power law behavior for $q \to 0$, in close analogy to what found for the T dependence of the susceptibility, and thus it does not affect the activated dynamics. It is thus possible that the behavior we observe is a complex combination of the activated evaporation of DNA nano-stars and a non-ideal critical slowing down.

6.2 Behavior of the $f = 4$ nano-stars at non-critical concentrations

To obtain a better characterization of the $f = 4$ system we investigated the behavior of $f = 4$ DNA nano-stars at various concentrations and temperatures. Samples having concentrations $c_{DNA} = 3.6, 5.4, 7.2$ and 18 mg/ml were investigated via static and dynamic light scattering within the wave vector range $15.7\mu m^{-1} < q < 28.5\mu m^{-1}$. We compare the results obtained for these non-critical samples with those obtained for the critical sample prepared at $c_{DNA} = 9$ mg/ml.

The sample at $c_{DNA} = 18$ mg/ml was obtained by preparing a $c_{DNA} = 6$ mg/ml sample and removing the diluted phase of the system after phase separation. It this way we should have produced a sample that is not subject to phase separation anymore, since its concentration is now that of the high concentration boundary of the phase diagram (at least up to the temperature at which the sample was prepared). Even if we don't have a detailed scan in temperature yet, it is interesting to compare its behavior with that of all the other samples. We will see in the following that the behavior of this system is in general different from that of the other non-critical samples. For this reason we will discuss it at the end of this section

Samples discussed in this section were all prepared diluting DNA in 30 mM NaCl electrolytic solution. The counterions concentration is thus different from sample to sample. As a consequence, this choice, adopted to ensure uniformity in the sample preparation, results in the fact that the melting temperature of the overhangs also varies from sample to sample depending on both the DNA concentration and the salt conditions. Despite this limitation we could determine a qualitative behavior of the $f = 4$ system that is coherent with the scenario proposed in section 6.1.

6.2.1 Static behavior

The quantity that can be used to compare the behavior of the samples at the various concentrations is the scattering intensity as a function of T. Fig. 6.8 shows the data collected at $\theta = 90°$. For any investigated sample, the scattering intensity increases as the temperature of the system approaches the coexistence region.

It is clear from the graph in Fig. 6.8 that the non-critical samples investigated here differ in the pseudo-critical temperature at which T diverges. We believe this is due to an interplay between differences in ionic strengths and differences in concentrations within the samples, since the melting temperature of the overhangs depends on both these quantities (see Eq. 2.6 and 2.8).

The maximum value that the scattering intensity reaches before the phase transition seems to depend on the concentration of the sample c_{DNA}, or on its distance from the critical concentration $c_c - c_{DNA}$. Measurements on DNA samples having concentration $c_c < c_{DNA} < 18$ mg/ml are still missing could provide new elements to clarify this point.

$I(q)$ for all the concentrations we explored exhibits a q dependence that becomes stronger as T approaches the coexistence region. At that temperatures, scattering intensity of all the investigated samples decreases of more than 40% in the explored range of q, with intensity decreasing as q increases. Such a q dependence indicates the growth of an

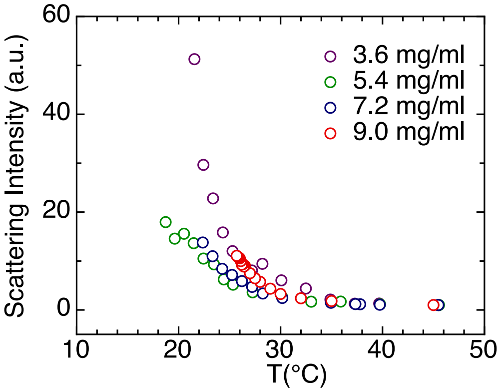

Figure 6.8: T dependence of the scattering intensity for the $f = 4$ system. Data acquired at $\theta = 90°$

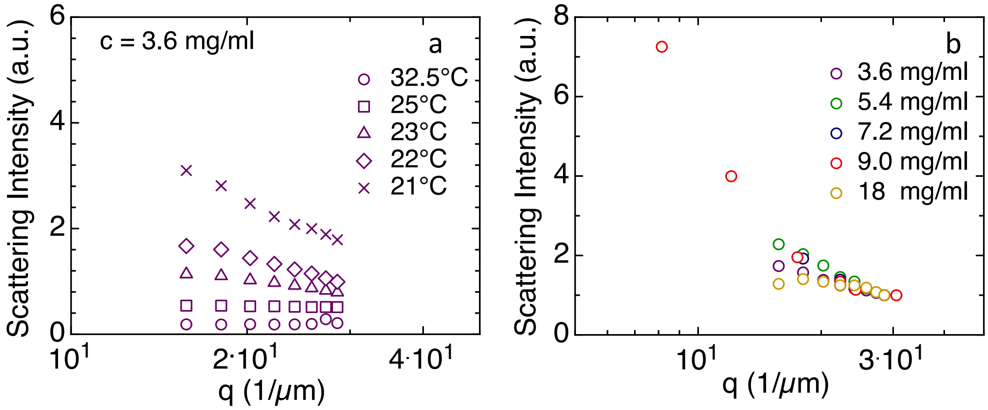

Figure 6.9: (a) Evolution of $I_s(q)$ as T is lowered. Data refers to the $f = 4$ sample at $c = 3.6$ mg/ml. (b) Comparison between $I_s(q)$ at the various concentrations for T close to the phase transition.

interconnected structure. As a representative behavior we plot in Fig. 6.9a the T dependence of the scattering intensity relative to the $c_{DNA} = 3.6$ mg/ml sample. $I_s(q)$ is flat at high temperatures, where DNA nano-stars are weakly interacting, and progressively develops a q-dependence as the temperature decreases.

To compare the behavior of the system at the various concentrations, we compare the $I_s(q)$ values relative to the closest temperature to the phase transition that was measured. For the $c_{DNA} = 18$ mg/ml sample we report data acquired at $T = 20°$C - a T value close to the transition temperature of the other samples - since a detailed scan in temperatures of the sample behavior is still missing. Data are reported in Fig. 6.9b, normalized so that the scattering intensities at $q = 28.5\ \mu^{-1}\mathrm{m}^{-1}$ are equal.

In the high q region $I(q)$ has a similar behavior for the various samples, growing as q decreases. Despite the q range explored is too narrow to enable any detailed analysis of the data, Fig. 6.9b shows that scattering intensities are shaped into a curve, diminishing their growth as q is reduced. This is in accord with the fact that pre-transitional fluctuations in non-critical samples have limited amplitude.

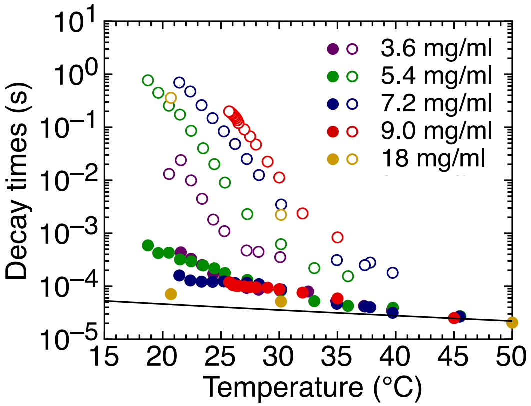

Figure 6.10: Decay times for $g_1(\tau)$ at the concentrations $c = 3.6, 5.4, 7.2, 9.0, 18$ mg/ml. *fast* times have the same weak T dependence, while *slow* times grow with temperature following the same exponential law. The black line represents the characteristic time expected for free diffusion of particles.

6.2.2 Dynamic behavior

T dependence of the characteristic times

We characterized the dynamic behavior of the samples via dynamic light scattering measurements. Field correlation functions for the non-critical set of samples show a single exponential decay at high temperatures, which evolves in a two step relaxation process as the temperature of the system is lowered.

As for the critical concentrations of both $f = 3$ and $f = 4$ systems, the two step relaxation of the non-critical samples is well fitted by a double stretched exponential. Fig. 6.10 shows the decay times obtained for all of the investigated concentrations (for the $f = 4$ structures) while approaching the phase transition.

Characteristic times of the *fast* relaxation process are the same for all of the DNA concentrations. τ_s of non-critical samples is characterized by the same weak dependence from temperature that we observed in the critical samples, decreasing by approximatively one decade before the phase transition happens. The only exception to such a behavior is represented by the $c_{DNA} = 18$ mg/ml sample, whose τ_f only decreases by a factor of ≈ 3 in the T range 50°C $-$20°C. Actually this is very close to the temperature dependence we would expect for the free diffusion process of unbound structures (black line in Fig. 6.10).

Even the *slow* relaxation processes of the non-critical samples show a temperature behavior similar to that observed for the critical concentration. When plotted in $lin - log$ scale, the τ_s for the various concentrations all grow with the same slope. This is an indication that the energy of bonding remains the same within the explored concentrations, involving approximatively three bonds (as previously discussed for the critical concentration sample). The characteristic times, though, strongly increases with the concentration of the samples, differing up to two decades for the $c = 3.6$ mg/ml and $c = 7.2$ mg/ml in the range of temperatures close to the phase transition. It is hard to tell if this effect is only due to differences in ionic strength among the samples (increasing the concentration of the sample the counterion concentration increases too, and the characteristic temperatures are moved upwards) or if is due to a more subtle contribution, e.g. a contribution due to the packing of the network. If the interpretation we propose of τ_s is correct, though, τ_s should be regulated by the lifetime of the duplexes that form between overhangs, a time that should be equal for any concentration condition.

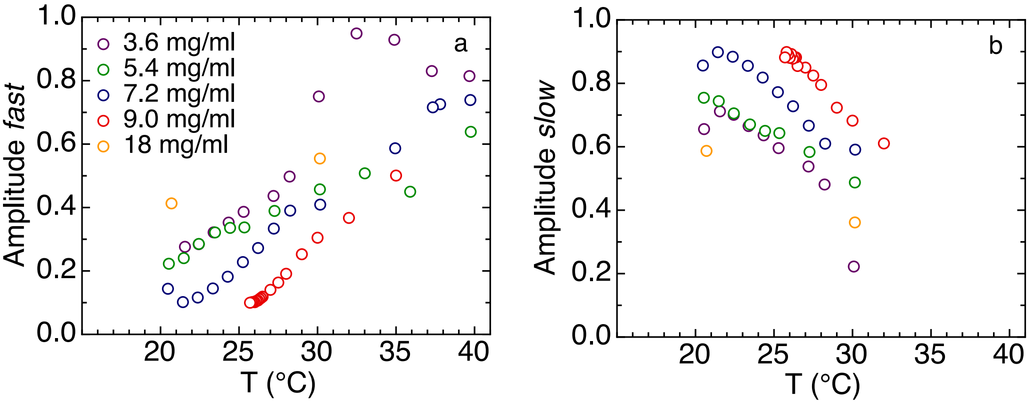

Figure 6.11: Amplitude of the stretching exponentials describing the (a) *fast* and (b) *slow* relaxation processes.

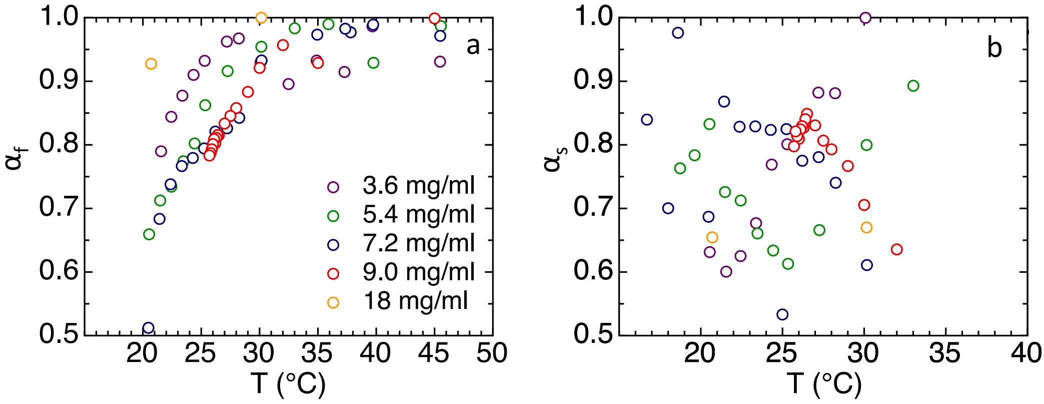

Figure 6.12: Stretching exponents relative to the (a) *fast* and (b) *slow* relaxation processes.

T dependence of the other fitting parameters

The temperature dependence of the other fitting parameters, A_f, A_s, α_f, α_s, is also similar to that discussed for the critical concentration sample. As the temperature lowers and interactions between DNA nano-stars become stronger, the amplitude of the *fast* decay reduces and that of the *slow* decay increases. The behavior of the two quantities is shown in Fig. 6.11. Ideally A_f should approach 1 at high temperatures, but since the correlation functions at those temperatures are affected from a spurious second decay (see section 4.3.3), the A_f reduces. A_s instead is not sensitive to this effect, so we use it to compare the behavior of the samples. Fig. 6.11b indicates that A_s for the critical sample (red dots) and for the $c = 7.2$ mg/ml sample (blue dots) depends from temperature in the the same way. Blue dots only seem to be shifted at lower temperatures with respect to the red dots, but in both set of data $A_s \approx 0.9$ as T approaches the coexistence region.

Upon lowering T, the behavior of A_s in the various samples appears to reflect the distance of each system from the critical concentration: samples closer to c_c develop larger fluctuations and have a dynamics that is more dominated by the slow component (larger A_s).

The temperature dependence of the stretching exponents is reported in Fig. 6.12. Stretching exponents for the $fast$ decay are $\alpha_f \approx 1$ at high temperatures, and decreases to a value comprised between 0.6 and 0.8 as T is lowered. α_s values instead show a less regular trend, oscillating between 0.5 and 0.9. We don't have any clear explanation for this irregular behavior, it may well be that it is due to the effects on the fitting process of irregularities in the correlation function.

q dependence of the characteristic times

We investigated the q dependence of the characteristic times τ_f and τ_s for the various concentrations and temperatures. Data are shown in Fig. 6.13. To compare the q dependence of the data, graphs include a guideline representing the q^{-2} behavior. The $fast$ decay times in Fig. 6.13a, c and e show a q^{-2} dependence for any concentration condition, thus supporting the hypothesis that it is expression of the diffusive process of single DNA nano-stars or clusters. The q dependence of the *slow* decay time varies instead with the concentration of the sample. Fig. 6.13b, d and f show τ_s for the explored concentrations. As the critical concentration is approached, $\tau_s(q)$ assumes the q^{-2} dependence that is expected for critical phenomena.

Analysis of the $c_{DNA} = 18$ mg/ml sample

Data reported in this section showed that the sample prepared at $c_{DNA} = 18$ mg/ml has, in general, a behavior that differs from that of the other non-critical samples investigated. This is reasonable since it does not, in principle, undergo the phase separation process. To sum up the differences with respect to the other sample, we observed (i) in Fig. 6.9 we could see that the sample $c_{DNA} = 18$ mg/ml, measured at $T = 20°$C, shows a weak q dependence of the scattering intensity (ii) the T dependence of τ_f is very close to the temperature dependence we would expect for the free diffusion process of unbound structures (see Fig. 6.10) (iii) Assuming that the *slow* decay times that we could plot in Fig. 6.10 are representative of the real temperature dependence of the sample, τ_s for this concentration exhibit a slope in the $lin - log$ plane that differs form that of the other samples.

By fitting $ln(\tau_s/\tau_f)$ we find that the energy associated to the relaxation process is $\Delta H = 39$ kcal/mol, corresponding to the rupture of approximatively 1 bond. This result cannot be trusted too heavily since it is built only on 2 data points. However, if one would take this result as significant, it would suggest that many DNA nano-stars are bind to the network for one bond only, or that only those nano-stars bound with just one bond are able to disconnect from the network. This may be due to the many structural defects that characterize the dense network, since the density of the system makes restructuring processes more difficult. τ_f suggest a similar scenario, i.e. it suggests that the only process taking part in the *fast* dynamics is the diffusion of single nano-stars. Neither diffusing clusters of nano-stars nor opening-closing processes of the network - which take part in the *fast* dynamics of the lower concentration samples - seem to have a role in determining τ_f for the $c = 18$ mg/ml sample.

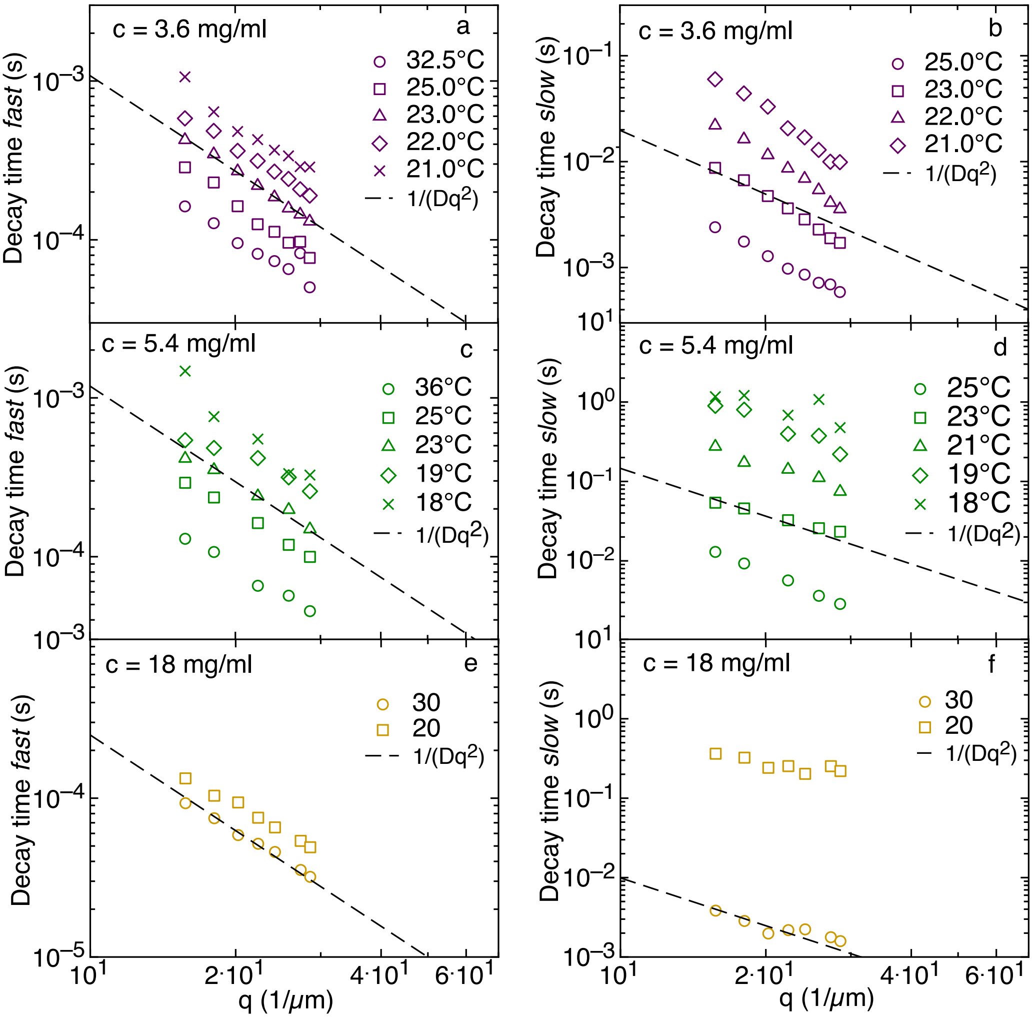

Figure 6.13: q dependence of the characteristic times τ_f and τ_s

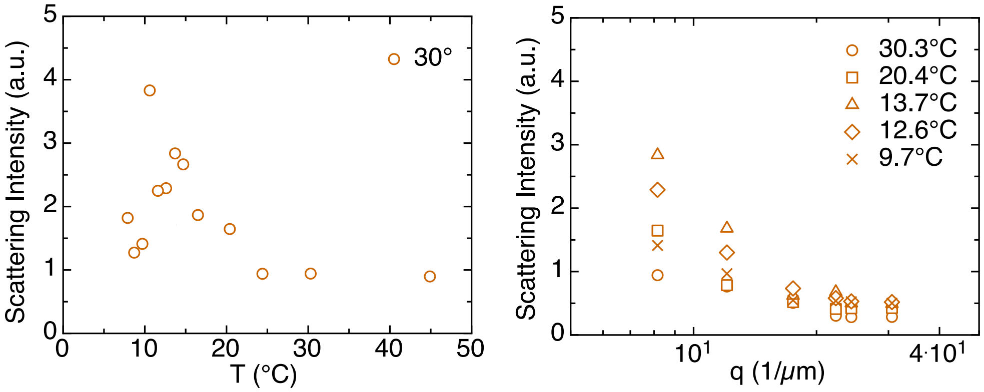

Figure 6.14: Scattering intensity measured at $\theta = 30°$

6.3 $f = 3$ DNA nano-stars at high concentration

On the bases of the interesting results obtained for the $f = 4$ system for the $c = 18$ mg/ml sample, we investigate the behavior of the $f = 3$ nano-stars at high concentration. The purpose is to determine the features of the $f = 3$ system out of the range of concentrations that include the coexistence region. Referring to the data furnished by the phase diagram reported in section 5.2 we prepared a $f = 3$ sample at concentration $c_{DNA} = 9$ mg/ml, which is just out of the phase boundary.

6.3.1 Static and dynamic behavior

Despite the sample is supposed not to cross the phase boundary, the scattering intensity significantly increases as the temperature is reduced (see Fig. 6.14).

A family of correlation functions measured at $\theta = 90°$ is shown in Fig. 6.15a. It is interesting to observe that even at high temperatures ($\approx 30°$C) correlation functions have three decays, which become four at $T \approx 11 - 12°$C. We fitted the correlation functions to the sum of three stretched exponential in order to have an estimation of their characteristic times. We fitted the first three decays. When a fourth decay appears in the correlation function, we still fit the first three decays only. Obviously, since the fit involves eight free parameters, several combinations on amplitudes, times and stretching exponent can in principle offer a good fitting of the data. The general behavior of the characteristic times is shown in Fig. 6.15b.

We notice that the first, fast decay in this sample is basically flat. Its only temperature dependence is due to the variation of viscosity with temperature. In the range of temperature between 30°C and 11°C we observe two decays which clearly grow with an Arrhenius fashion and that, at the same temperature, always differ more than one decade in time.

When $T < 11°$C a fourth decay grows between A and B. While decay B still decreases in an Arrhenius fashion as the temperature is lowered, decay D is constant, with a characteristic time $\tau \approx 0.1$ s. This is a clear indication of some more subtle mechanism regulating the decorrelation process.

Another intriguing element offered by this high concentration sample is represented by the parameters determining the Arrhenius growth that characterize the slow decay B. In fig. Fig. 6.16a we compare the A and B decays of the $c = 9$ mg/ml sample with the

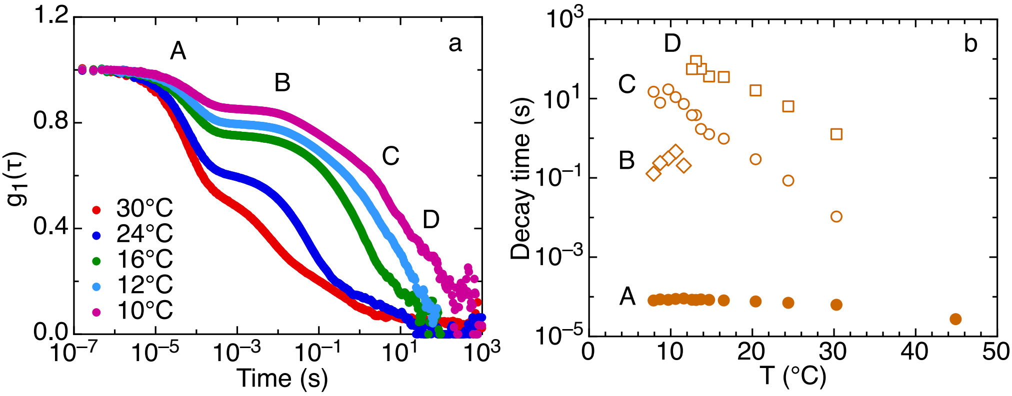

Figure 6.15: Family of correlation functions for the $f = 3$ system, measured at $\theta = 90°$.

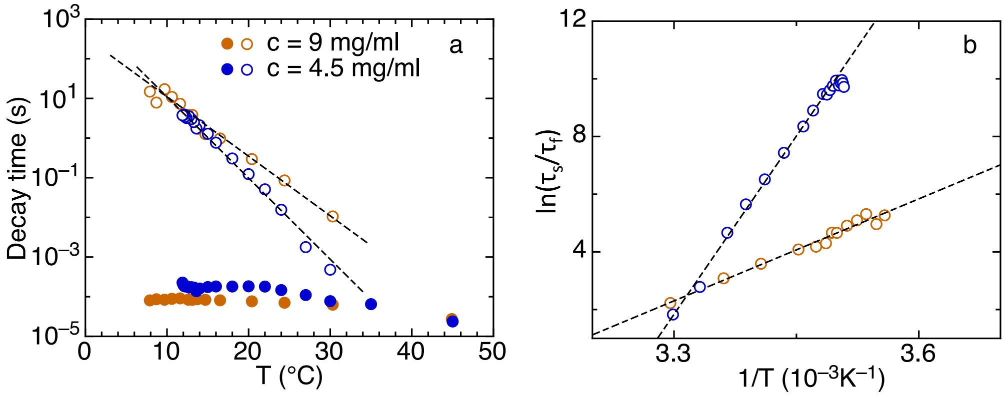

Figure 6.16: Comparison between critical sample ($c_{DNA} = 4.5$ mg/ml, blue dots) and high concentration sample ($c_{DNA} = 9$ mg/ml, orange dots). (a) Decay times as a function of T (b) $ln(\tau_s/\tau_f)$ plotted as function of $1/T$ and fitted by an Arrhenius law.

τ_f and τ_s associated to the critical $f = 3$ sample with $c = 4.5$ mg/ml. It is evident from the graph that the two *slow* times grows with the same Arrhenius law, but with different slope. As discussed in section 6.1 the slope of the τ_s is related to the activation energy that the overhangs need in order to break a bond. In principle this energy is the same for any concentration, thus the slope of the times should be the same for the two sample. Fitting the $ln(\tau_s/\tau_f)$ for the $c = 9$ mg/ml sample we find that an energy $\Delta H \approx 23$ kcal/mol, which is equal to ≈ 0.5 bonds.

The argument to explain this value of the energy of bond is the same discussed for the $f = 4$ sample prepared at $c = 18$ mg/ml, involving difficulties in the restructuring process and free diffusion associated to free nano-stars only. Despite the huge amount of lacking of data for the $f = 4$ sample, the behavior of $f = 3$ and $f = 4$ systems at high concentrations is similar.

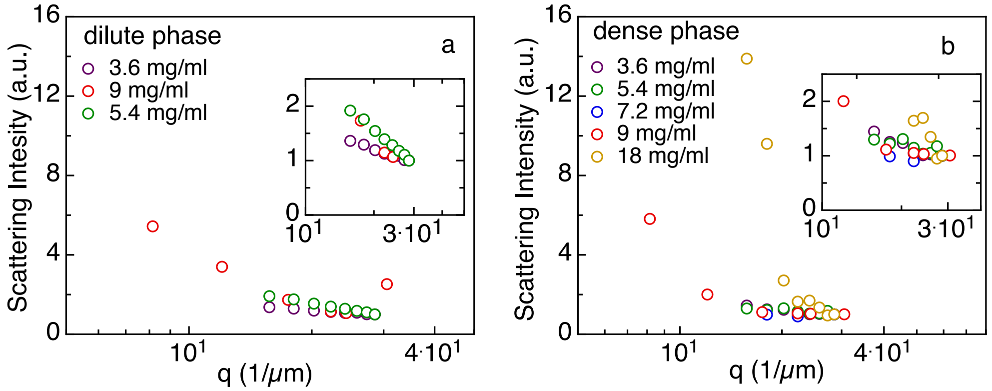

Figure 6.17: q dependence of the scattering intensity in (a) dilute and (b) dense phase for the $f = 4$ system. Insets show the same data, in a restricted region.

6.4 Characterization of coexisting phases

We used static and dynamic light scattering to characterize the two coexisting phases that compose the sample after phase separation. On the bases of the gel electrophoresis measurements and of the phase diagram (see section 5.2) we know that the diluted phase is mainly composed of a collection of well-formed and ill-formed nano-stars at a concentration $c_{-} \approx 0.5$ mg/ml. The behavior of this phase should be that of a gas-like phase and we expect that the only phenomena characterizing the sample is diffusion. Thus, we expect the correlation function to decay as a simple exponent.

The dense phase instead contains the network, that reconfigures via the processes described in section 6.1 (evaporation of single particles and clusters, network oscillation). As for the isotropic sample, correlation function of the dense phase should thus be composed again of two decays, a *fast* one that account for the free diffusion of particles and clusters, and a *slow* one that accounts for the reconfiguration of the network.

6.4.1 Static and dynamic behavior

In both dilute and dense phase the scattering intensity is relatively flat with respect to the strong q dependence that the systems showed while approaching the phase boundary from above.

This is not surprising for the diluted phase since it contains small, independent objects and thus the Rayleigh scattering condition holds.

We compare the correlation functions measured in the coexisting phases. We report as representative examples data acquired for the $c = 5.4$ mg/ml and $c = 9$ mg/ml samples. Fig. 6.18 show the correlation functions measured for $\theta = 90°$ and for a temperature close to the phase transition, together (homogeneous phase, red dots) with the two correlation functions measured in the diluted and dense phase (blue and green dots respectively). The non-critical sample at $c = 5.4$ mg/ml shows, in the dilute phase, a single relaxation that is well fitted by a single stretched exponential with stretching exponent $\alpha \approx 0.8$. Since the dilute phase collects most of the ill-formed structures we consider this stretched exponential to be due to polydispersity of the sample, in agreement with expectations. Again in agreement with the expected behavior, the dense phase shows a two step relaxation. Characteristic times of the *fast* component of the correlation functions measured

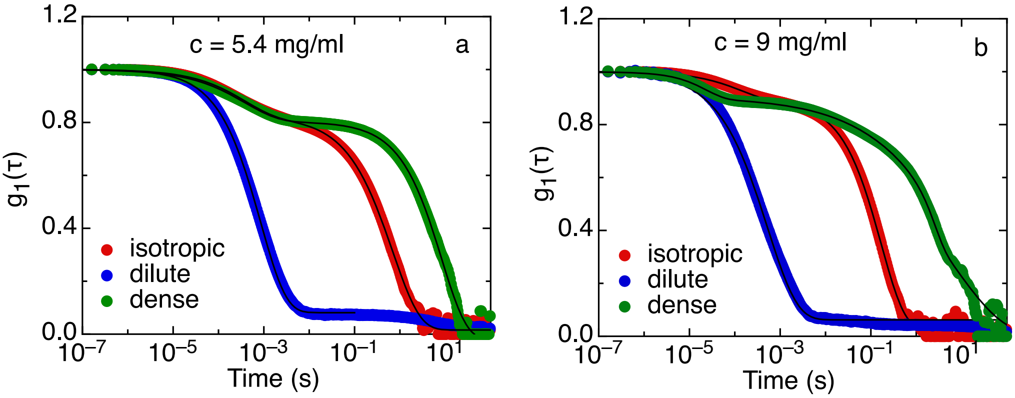

Figure 6.18: Field correlation functions in coexisting phases for $f = 4$ nano-stars

in the isotropic phase and in the dense phase are equal to the characteristic time of the dilute phase correlation function, indicating that they refer to the same process of free diffusion. The characteristic time of the slow decay, instead, slows down even more after the phase transition has occurred, growing from ≈ 0.5 s to ≈ 8 s, meaning that the network is now more stable. The amplitude of the *slow* decay remains instead the same before and after the phase transition, meaning that the network has ceased to grow.

The critical sample presents some variation to this behavior. Again the dilute and dense phase show a single and a double stretched exponential decay respectively, but the τ_f value differs in the three cases. Its value grows from 1.2×10^{-4} s in the isotropic phase to 7×10^{-4} s in the dilute phase, a variation of a factor 6. The diffusive process relative to the dense phase instead is faster, being $\approx 2 \times 10^{-5}$ s. Again, the amplitude of the *slow* decay remains constant after phase separation has occurred, but in this case the slow relaxation process of the dense phase shows multiple components. Four decays are distinguishable in the green correlation function in Fig. 6.18b. This peculiar shape of the correlation function suggests that the decorrelation process involving DNA hybridization and denaturing processes is actually even richer than what discussed up to now.

The meaning of all of these decays is still unclear. It is also unknown up to know why these multiple decays do not appear in the correlation function measured in the dense phases of samples which have different native concentrations, as the case of $c = 5.4$ mg/ml in Fig. 6.18a.

Future directions

In the present Thesis we addressed the fundamental question about the nature of the phase diagram of limited-valence particles. We experimentally investigated the equilibrium phase behavior of solutions of DNA nano-stars having valence number either $f = 3$ and $f = 4$, providing the first experimental study on the collective behavior of particles having bond limitations in number and directionality. We found that solutions of $f = 3$ and $f = 4$ nano-stars exhibit phase separation and that the coexistence region significantly shrinks as the valence is reduced. The coexistence region is in the shape of a liquid-gas consolution curve, necessarily terminating, at the top end, in a critical point. To the best of our knowledge, this is the first observation of critical behavior in DNA solutions.

As the critical point is approached from above the dynamic behavior of the system slows down and becomes characterized by a two-step relaxation process. As T decreases, the two characteristic times behave differently: the faster one (τ_f) changes only very mildly while the slower one (τ_s) slows down by more than three orders of magnitude in an Arrhenius fashion, without any noticeable divergence as T_c is approached.

The activated dynamics is a feature strictly related with the nature of the bonds between the particles: since bonds are provided by hybridization of DNA overhangs, their rupture is subject to an activation energy. What is surprising is that τ_s does not show the power-law divergence expected for critical slowing down.

Given these results, as a future direction it would be interesting to study the behavior of the $f = 3$ and $f = 4$ at low scattering angles ($\theta < 5°$) to determine if under this limit it is possible to access a region where the decorrelation process of the system is determined by the critical slowing down, or by a combination of critical slowing down and activated dynamics.

Since the concentration of the dense phase is rather low, according with numerical predictions discussed in section 1.3, a very promising field of research is related to the experimental study of the network region where an equilibrium gel is expected to form. In this work we presented a first result obtained in such region for the $f = 3$ system, and partial data for the $f = 4$ system, but a systematic experimental investigation of the properties of equilibrium gels is still missing.

Another open issue concerns the behavior of solutions of $f = 3$ and $f = 4$ particles in different salt conditions - here we only only worked in ≈ 50 mM NaCl - to investigate how the phase diagram, and especially the dynamics, are affected by ionic strength. It would indeed be very interesting to become able to control the lifetime of the DNA bonds through ionic strength, pH or through the addition of denaturant, and investigate how such modifications reflect in the kinetics of the system far and close to the phase transition.

Bibliography

[1] S. Glotzer and M. Solomon, Nature Materials **6**, 557 (2007).

[2] A. Jackson, J. Myerson, and F. Stellacci, Nature Materials **3**, 330 (2004).

[3] G. Yi, V. Manoharan, E. Michel, M. Elsesser, S. Yang, and D. J. Pine, Adv. Mater. **16**, 1204 (2004).

[4] D. Kraft, J. Groenewold, and W. Kegel, Soft Matter. **5**, 3823 (2009).

[5] E. Bianchi, J. Largo, P. Tartaglia, E. Zaccarelli, and F. Sciortino, Phys. Rev. Lett. **97**, 168301 (2006).

[6] S. Sacanna, W. Irvine, P. Chaikin, and D. Pine, Nature **464**, 575 (2010).

[7] Y. Wang, Y. Wang, D. Breed, V. Manoharan, L. Feng, A. Hollingsworth, M. Weck, and D. Pine, Nature **491**, 51 (2012).

[8] K. Binder and W. Kob, *Glassy Materials And Disordered Solids: An Introduction to Their Statistical Mechanics* (World Scientific Publishing Company, 2005).

[9] R. Jones, *Soft Condensed Matter* (Oxford University Press, 2002).

[10] D. Frenkel, Physica A **313**, 1 (2002).

[11] E. Zaccarelli, J.Phys.: Condens. Matter **19**, 323101 (2007).

[12] L. Cippelletti and L. Ramos, J.Phys.: Condens. Matter **17**, R253 (2005).

[13] P. Pusey and W. van Megen, Nature **320**, 340 (1986).

[14] M. Dijkstra, J. Brader, and R. Evans, J.Phys.: Condens. Matter **11**, 10079 (1999).

[15] F. Sciortino, Nature Materials **1**, 145 (2002).

[16] P. Lu, E. Zaccarelli, F. Ciulla, A. Schofield, F. S. F, and D. Weitz, Nature **453**, 499 (2008).

[17] T. Bellini, R. Cerbino, and G. Zanchetta, Topics in Current Chemistry **318**, 225 (2012).

[18] M. Wertheim, J. Stat. Phys. **35**, 19 (1984).

[19] L. Rovigatti and F. Sciortino, Molecular Physics , 1 (2011).

[20] B. Ruzicka, E. Zaccarelli, L. Zulian, R. Angelini, M. Sztucki, A. Moussaid, T. Narayanan, and F. Sciortino, Nature Materials **10**, 56 (2011).

[21] C. Calladine, H. Drew, B. Luisi, and A. Travers, *Understanding DNA - The molecule and how it works, 3rd edition* (Elsevier Academic Press, 2004).

[22] J. Watson and F. Crick, Nature **171**, 737 (1953).

[23] J. SantaLucia, Proc. Natl. Acad. Sci. **95**, 1460 (1998).

[24] J. SantaLucia and D. Hicks, Annual Review of Bioph. Biomol. Struct. **33**, 415 (2004).

[25] F. Manyanga, M. Horne, G. Brewood, D. Fish, R. Dickman, and A. Benight, The Journal Of Physical Chemistry B **113**, 2556 (2009).

[26] R. Owczarzy, Biophysical Chemistry **117**, 207 (2005).

[27] R. Owczarzy, *PhD Thesis* (University of Illinois at Chicago, 1999).

[28] H. Lodish, A. Berk, and S. Zipursky, *Molecular Cell Biology* (W. H. Freeman, 2000).

[29] Y. Roh, R. Ruiz, S. Peng, J. Leea, and D. Luo, Chem. Soc. Rev. **40**, 5730 (2011).

[30] F. Simmel and W. Dittmer, Small **1**, 284 (2005).

[31] N. Seeman, Annual Review of Biochemistry **79**, 65 (2010).

[32] N. Kallenbach, R. Ma, and N. Seeman, Nature **305**, 829 (1983).

[33] J. Chen and N. Seeman, Nature **350**, 631 (1991).

[34] R. Goodman, M. Heilemann, S. Doose, C. Erben, A. Kapanidis, and A. Turberfield, Nature Nanotechnology **3**, 93 (2008).

[35] Y. He, T. Ye, M. Su, C. Zhang, A. Ribbe, W. Jiang, and C. Mao, Nature **452**, 198 (2008).

[36] C. Zhang, M. Su, Y. He, X. Zhao, P. Fang, A. Ribbe, W. Jiang, and C. Mao, Proc. Natl. Acad. Sci. **105**, 10665 (2008).

[37] P. Rothemund, Nature **440**, 297 (2006).

[38] N. Seeman, Nature **421**, 427 (2003).

[39] N. Chelyapov, Y. Brun, M. Gopalkrishnan, D. Reishus, B. Shaw, and L. Adleman, J. Am. Chem. Soc. **126**, 13924 (2004).

[40] D. Liu, M. Wang, Z. Deng, R. Walulu, and C. Mao, J. Am. Chem. Soc. **126**, 2324 (2004).

[41] E. Winfree, F. Liu, L. Wenzler, and N. Seeman, Nature **394**, 539 (1998).

[42] H. Yan, S. Park, G. Finkelstein, J. Reif, and T. LaBean, Science **301**, 1882 (2003).

[43] Y. He, Y. Chen, H. Liu, A. Ribbe, and C. Mao, J. Am. Chem. Soc. **127**, 12202 (2005).

[44] W. Liu, H. Zhong, R. Wang, and N. Seeman, Angew. Chem. Int. Ed. **50**, 264 (2011).

[45] J. Zheng, J. Birktoft, Y. Chen, T. Wang, R. Sha, P. Constantinou, S. Ginell, C. Mao, and N. Seeman, Nature **461**, 74 (2009).

[46] S. Um, J. Lee, N. Park, S. Kwon, C. Umbach, and D. Luo, Nature Materials **5**, 797 (2006).

[47] B. J. Berne and R. Pecora, *Dynamic light scattering* (Krieger, 1990).

[48] H. C. van de Hulst, *Light scattering by small particles* (Dover Publications Inc., 1981).

[49] W. Brown, *Light scattering - Priciples and development* (Clarendon Press., 1996).

[50] T. Bellini, *Statica e dinamica della birifrangenza elettrica di liquidi complessi* (PhD. thesis, 1990).

[51] C. P. Lindsey and G. R. Patterson, J. Chem. Phys **73**, 3348 (1980).

[52] J. Ricka, Applied Optics **32**, 2860 (1993).

[53] T. A. J. Duke, J. Chern. Phys. **93**, 9049 (1990).

[54] H. Lau and L. Archer, Phys. Rev. E **84**, 061916 (2011).

[55] C. Cantor and P. Schimmel, *Biophysical chemistry part II: techniques for the study of biological structure and function* (Freeman, 2001).

[56] A. Tataurov, Y. You, and R. Owczarzy, Biophysical Chemistry **133**, 66 (2008).

[57] G. Felsenfeld and S. Hirschman, J. Mol. Biol. **13**, 407 (1965).

[58] J. Glasel, Biotechniques **18**, 62 (1995).

[59] G. Zanchetta, *Liquid crystalline phases in oligonucleotides solutions* (PhD. thesis, 2007).

[60] F. Livolant and A. Leforestier, Prog. Polym. Sci. **21**, 1115 (1996).

[61] M. Nakata, G. Zanchetta, B. Chapman, C. Jones, J. Cross, R. Pindak, T. Bellini, and N. Clark, Science **318**, 1276 (2007).

[62] G. Zanchetta, F. Giavazzi, M. Nakata, M. Buscaglia, R. Cerbino, N. Clark, and T. Bellini, J. Chem. Phys. **107**, 17497 (2010).

[63] Y. Li, Y. D. Tseng, S. Y. Kwon, L. d'Espaux, J. S. Bunch, P. L. McEuen, and D. Luo, Nature Materials **3**, 38 (2004).

[64] R. Owczarzy, M. Vallone, J. Gallo, M. Paner, J. Lane, and S. Benight, Biopolymers **44**, 217 (1998).

[65] K. Stewart and L. McLaughlin, J. Am. Chem. Soc. **126**, 2050 (2004).

[66] E. Bianchi, P. Tartaglia, E. Zaccarelli, and F. Sciortino, Journal of Chemical Physics. **128**, 144504 (2008).

[67] G. Foffi and F. Sciortino, J. Phys. Chem. B **111**, 9702 (2007).

[68] A. Pelissetto and E. Vicari, Physics Reports **368**, 549 (2002).

[69] H. Stanley, *Introduction to Phase Transitions and Critical Phenomena* (Oxford University Press, 1987).

[70] A. H. Krall and D. A. Weitz, Phys. Rev. Lett. **80**, 778 (1998).

[71] S. Howorka, L. Movileanu, O. Braha, and H. Bayley, Proc. Natl. Acad. Sci. U.S.A. **98**, 12996 (2001).

[72] A. Coniglio and W. Klein, J. Phys. A **13**, 2775 (1980).

List of Publications

Publications in preparation

S. Biffi, R. Cerbino, F. Bomboi, E.M. Paraboschi, R. Asselta, F. Sciortino, and Tommaso Bellini PHASE BEHAVIOUR AND CRITICAL ACTIVATED DYNAMICS OF LIMITED-VALENCE DNA NANO-STARS